Titre: Title:	Towards Space Grade Lasers for Sr Atomic Clock Applications: Fabrication and Characterization of a DFB Tm PM Fiber Laser with a Novel Single Polarization Single Frequency Design
Auteur: Author:	Yannick Cuerno
Date:	2022
Type:	Mémoire ou thèse / Dissertation or Thesis
Référence: Citation:	Cuerno, Y. (2022). Towards Space Grade Lasers for Sr Atomic Clock Applications: Fabrication and Characterization of a DFB Tm PM Fiber Laser with a Novel Single Polarization Single Frequency Design [Mémoire de maîtrise, Polytechnique Montréal]. PolyPublie. https://publications.polymtl.ca/10746/

POLYTECHNIQUE MONTRÉAL

affiliée à l'Université de Montréal

Towards Space Grade Lasers for Sr Atomic Clock Applications: Fabrication and Characterization of a DFB Tm PM Fiber Laser with a Novel Single Polarization Single Frequency Design

YANNICK CUERNO

Département de génie physique

Mémoire présenté en vue de l'obtention du diplôme de *Maîtrise ès sciences appliquées*

Génie Physique

Décembre 2022

POLYTECHNIQUE MONTRÉAL

affiliée à l'Université de Montréal

Ce mémoire intitulé :

Towards Space Grade Lasers for Sr Atomic Clock Applications: Fabrication and Characterization of a DFB Tm PM Fiber Laser with a Novel Single Polarization Single Frequency Design

présenté par **Yannick CUERNO**

en vue de l'obtention du diplôme de *Maîtrise ès sciences appliquées*

a été dûment accepté par le jury d'examen constitué de :

Frédéric LEBLOND, président
Raman KASHYAP, membre et directeur de recherche
Frédéric MAES, membre externe

DEDICATION

To my parents, family and grandparents who have given all for us to have dreams

A mis padres, familia y abuelos quienes han luchado para que tengamos sueños

ACKNOWLEDGEMENTS

This work was a collaborative effort made possible with the help of many people from Polytechnique Montréal and MPB Communications (MPBC).

From MPBC, I would like to acknowledge technical support from Yan Boulay. His expertise on fiber loading was used throughout the project. I am also grateful to Nathalie Toupin and Julie Grondin M.Sc. A, whose initial support led to the realization of this partnership. Lastly, a warm thank you to Vladimir Karpov Ph.D. for his more than helpful insight and implication during all this master's work.

From Polytechnique Montréal, first I would first like to express my gratitude to the Electric Engineering and Physics Engineering departments staff for their help throughout the project. In no specific order: Lyne Dénommé, Mikaël Leduc, Jean-Paul Levesque, Emile Jetzer, Louis-Philippe Carignan Ph.D., and Pascal Burasa Ph.D.

Followed by co-workers and friends also in no specific order. Thank you, Frederic Monet, for the valuable discussions throughout the experiments, and for his big contribution in writing all the successful and… unsuccessful gratings! Thank you, Prof. Sébastien Loranger, for his contribution to this work via our discussions and with his more than relevant experimental insight. Likewise, thank you to Jean-Sébastien Boisvert, for the discussions, sometimes during the weekends, and his ideas on how to approach a problem; his passion for photonics is undeniable. Thank you, Anthony Roberge, for passing down a small portion of your simulation knowledge.

A great amount of appreciation for Prof. Raman Kashyap. For the opportunity to pursue my passion in his research group, for our multiple exchanges and discussions throughout the project. His comments and questions could feel challenging at times, but they were always big tool learners.

Additionally, a word of gratitude to my defense committee, Prof. Frédéric Leblond and Frédéric Maes Ph. D. for their time in reviewing my work with their respective expertise.

Merci à mes proches, parents et amis, avec une mention particulière à ma copine Elissa Haddad pour son amour et sa rigueur scientifique qui me pousse à me surpasser.

RÉSUMÉ

Les lasers monofréquences jouent un rôle fondamental dans diverses applications en passant par la métrologie, les senseurs et les télécommunications. Depuis quelques années, ils jouent un rôle crucial dans la nouvelle génération d'horloges atomiques, les horloges optiques. Celles-ci promettent de belles avancées scientifiques tant fondamentales, e.g., quantique, unité de base SI, qu'appliquées, e.g., satellites, métrologie, en particulier celles basées sur l'atome de strontium (Sr^{87}). Les horloges optiques actuelles nécessitent des systèmes encombrants basés sur de l'optique en espace libre. Une réduction de la taille et une augmentation de la fiabilité sont souhaitables pour accroître leur accessibilité et leur utilisation dans de nouvelles installations telles que dans l'espace. Les lasers fibrés monofréquences offrent les avantages souhaités, mais les spécifications du laser pour l'horloge de Sr^{87} posent plusieurs défis de conception dans la fibre optique. Les principaux défis proviennent de la haute puissance requise à la longueur d'onde du réseau optique à 813 nm, ainsi que du besoin d'utiliser une fibre à maintien de polarisation pour tout le système, particulièrement dans la fibre de gain.

Dans cette étude, nous proposons un nouveau montage pour un laser monofréquence à polarisation linéaire unique basé sur un réseau de Bragg à rétroaction répartie dans de la fibre dopée au Thulium (Tm) à maintien de polarisation avec un réseau de Bragg externe. Ce dernier est discriminatif en polarisation et permet ainsi une opération à polarisation unique du laser lorsqu'en phase. Contrairement aux lasers à cavités courtes, notre laser permet une plus grande longueur de fibre active et ne requiert pas d'épisseuses de pointes. Le laser développé qui émet à 1742 nm s'insèrera avec un laser 1530 nm dans un système combinant *MOPA (*Master optical power amplifier*)* et effets non-linéaires pour générer la longueur d'onde du réseau optique requise à 813.420 nm.

L'étude démontre tout d'abord la faisabilité du laser à rétroaction répartie dans la fibre dopée au Tm. Des simulations du plan de conception montrent les paramètres clés à contrôler pour le bon fonctionnement du laser soit la longueur de la cavité externe, la phase, la température puis l'accord en longueur d'onde. Enfin, l'étude démontre la robustesse de son opération monofréquence à polarisation unique face aux perturbations de phase et de température testé sur une plage de 11 GHz. Une puissance de sortie au-dessus de la puissance minimum requise de 1 mW est observée.

ABSTRACT

Single frequency lasers are essential in diverse applications such as metrology, sensors, and telecommunications. In recent years, they have played a key role in the development of new atomic clocks, optical clocks. These systems show great promise for fundamental scientific breakthroughs, e.g., quantum, SI units' definition as well as for applications, e.g., satellites, metrology, in particular optical clocks based on Sr^{87}. Current optical clocks require bulky systems based on free space optics. Improvements in compactness and reliability are desired to increase their accessibility and broaden their environment usage such as in space. Single frequency fiber lasers offer such advantages. However, the laser specification requirements for Sr^{87} atomic clock lead to multiple design challenges. They mainly arise from the high power required at the optical lattice wavelength of 813 nm and from the use of polarization maintaining fiber, including the gain fiber.

In this work, we propose a new design for a single frequency (SF) single linear polarization (SP) laser based on a distributed feedback (DFB) laser in thulium (Tm) fiber with an external fiber Bragg grating (FBG). This external FBG discriminates in wavelength thus allowing single polarization laser operation when in phase. Unlike short-cavity lasers, our developed laser enables usage of a longer active fiber and does not require cutting-edge splicing equipment. The laser emits at λ = 1742 nm and will be integrated in a MOPA system with a 1530 nm laser. Their combined usage with non-linear optics will achieve the required optical lattice wavelength of 813.420 nm.

This work demonstrates the feasibility of a DFB laser in polarization maintaining Tm fiber. Simulations based on the proposed design then highlight key parameters for robust single polarization single frequency laser operation. These parameters are the external cavity length, the phase, the temperature uniformity, and the wavelength tuning. Finally, we demonstrate robust SPSF operation under strain and temperature tuning and a desired output power of >1 mW output power.

TABLE OF CONTENTS

LIST OF TABLES

LIST OF FIGURES

LIST OF SYMBOLS AND ABBREVIATIONS

ASE	Amplified spontaneous emission
CW	Continuous wave
DBR	Distributed Bragg reflector
DFB	Distributed feedback
EDF	Erbium doped fiber
EM	Electromagnetic
ESA	Electronic spectrum analyzer
FBG	Fiber Bragg grating
FP	Fabry-Pérot
FPI	Fabry-Pérot interferometer
fs	Femtosecond
FSR	Free spectral range
FWHM	Full width at half maximum
ISO	Optical isolator
LD	Laser diode
LHS	Left-hand side
LIDAR	Light Detection and Ranging
MFD	Mode field diameter
MOPA	Master oscillator power amplifier
MWL	Magic wavelength
NASA	National Aeronautics and Space Administration
O.P.	Optical path
OSA	Optical spectrum analyzer

PC	Power coupler
PM	Polarization maintaining
Pp	Pump power
PS	Phase-shift
Q-factor	Quality factor
RHS	Right-hand side
SC	Semiconductor
SF	Single frequency
SI	International System of Units
SP	Single polarization
Sr	Strontium
TDF	Thulium doped fiber
Tm	Thulium
UV	Ultraviolet
WDM	Wavelength division multiplexer
Yb	Ytterbium

CHAPTER 1 INTRODUCTION

1.1 Context – Single Frequency Fiber Lasers

The discovery of lasers in 1960 by Theodore H. Maiman [1] was a great scientific breakthrough of the 20th century. Lasers provide light with highly sought-after properties such as spatial and temporal coherence. This new technology was then combined with fiber optics achieving the first demonstration of a fiber laser by Koester and Snitzer in 1964 [2]. The combination of the laser properties and the fiber optics benefits such as heat dissipation, electromagnetic radiation shielding, beam quality, and the lack of alignment requirement [3] have enabled fiber lasers to achieve a wide range of emission wavelengths. This range covers wavelengths as low as ultraviolet (UV) [4] up to the mid-infrared spectral region [5]. The single frequency (SF) fiber laser is a well-established category of various lasers which offer an increased temporal coherence. Such lasers are also known as narrow-linewidth fiber lasers and usually operate with linewidths in the MHz to kHz range [3]; ultranarrow fiber lasers with linewidths in the Hz range have also been demonstrated [6]. This property is desired for multiple applications including spectroscopy, metrology, light detection and ranging (LIDAR), and nonlinear frequency conversion [3, 7]. Over the past decade, optical clocks have emerged as a cornerstone tool for metrology applications of time measurement, which has led to an increase in demand for single frequency lasers [8-10]. Optical clocks setups are complex and include the usage of multiple SF lasers for atomic excitation and noise reduction. One of the subsystems used for noise reduction is the optical lattice [10, 11]. In their current state, optical lattice setups remain bulky, just like others optical clocks systems, which hinders their application and accessibility. SF laser sources based on fiber optics technology present a high potential to bring optical lattice systems towards a more compact design while preserving their required specifications. However, the selection of an SF laser from their multiple existing designs needs to take into consideration the optical lattice specifications. A state-of-the-art on SF fiber lasers is presented in section 2.4. Once a design is selected, the laser characterization is a critical step before integration for the understanding of its benefits and limitations. The focus of this work is placed on the selection, fabrication, understanding and characterization of a novel distributed feedback (DFB) SF fiber laser. In the following section we present an overview on optical clocks and its subsystem, the optical lattice. Their introduction will lead to the specification's requirement crucial to the SF fiber laser design and the associated challenges.

1.2 Unveiling the Mysteries of Time

Time is at the core of the scientific world as one of the fundamental quantities. For centuries, the fundamental unit of time has been regarded as invariant, a fixed measurement completely independent of other phenomena. However, scientific breakthroughs beginning with the general theory of relativity in the early 20th century challenged and changed how we perceive time. At the centre of this breakthrough are atomic clocks – utilizing the natural electronic transitions states in atoms to measure frequency, and hence time. These devices have revolutionized the way we measure time [9]. This impacts other fundamental quantities that rely on time for their own definition as published by the Bureau International des Poids et Mesures (BIPM) [12], schematized in Figure 1-1 and thus also impacts our understanding of core physics phenomena such as gravity, force, temperature, quantum mechanics, electric and magnetic fields to name but a few. Their usage is also found in the booming space industry - providing satellites the accuracy needed to fulfil their increasing specification requirements [8].

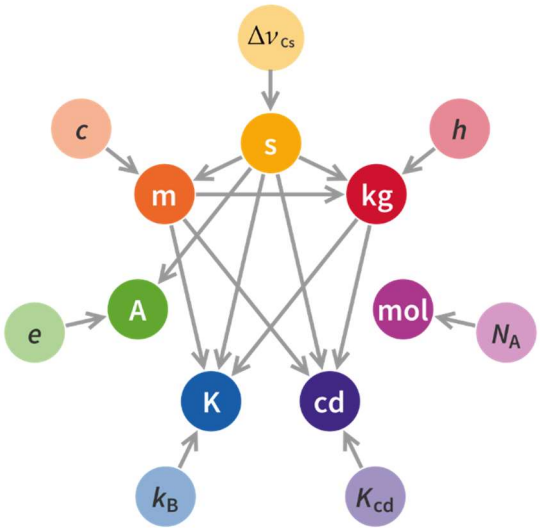

Figure 1-1 SI units interdependence with their respective symbol from BIPM SI units 9th edition report. © 2016 E. Pisanty [12], reproduced with permission.

Researches from the European Space Agency [8] to NASA [13] show increase interest in developing the technology for space applications and space research. Finally, they could play an

important role in the current climate change crisis - providing unprecedented precision for environmental monitoring, for example of melting ice sheets and increasing ocean levels [14].

The new generation of atomic clocks known as optical clocks, rely on optical frequencies of electron band transitions rather than the radio frequencies currently used by standard atomic clocks to measure time. The new generation has an uncertainty reduced by 4-5 orders of magnitude compared to their radio waves counterpart [9]. Such precise and accurate measurements are easily susceptible to noise effects known as light shift which broadens their transition frequency. The light shift comes from: the AC Stark shift effect where oscillating electromagnetic waves split the transition states, from the Doppler shift, and from the recoil shift [15]. Optical lattices are one of many systems required for noise reduction. Like a lattice structure found in solid state matter, the atoms are trapped in place using standing waves generated by laser interference, reducing atomic noise [16]. Another critical system combined with optical lattices for noise reduction is laser cooling [11]. Once combined, these systems create the conditions for atoms to reach the Lamb-Dicke regime where the temperature of atoms reach micro-kelvins (μK) [17, 18] – mitigating light shift effects (noise). Figure 1-2 shows a simplified representation of an optical lattice.

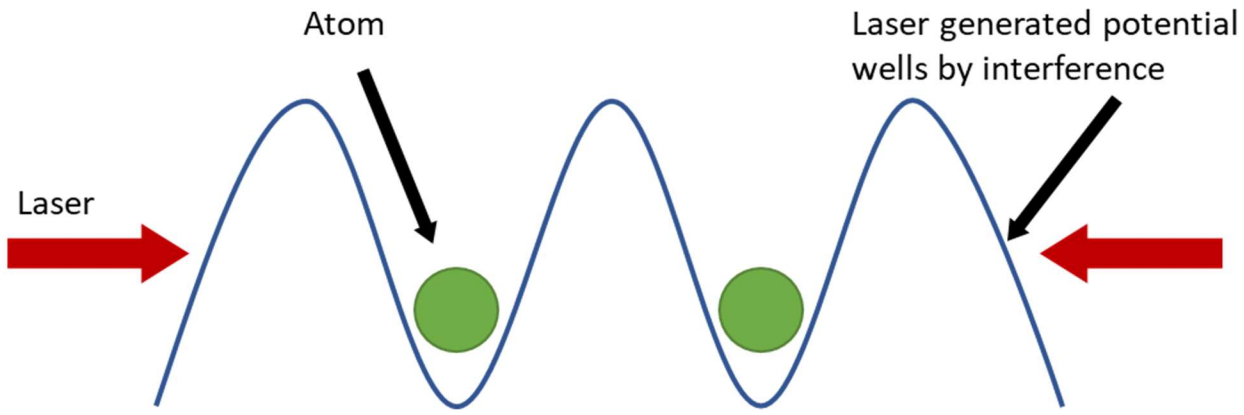

Figure 1-2 Optical lattice diminishes electronic gap transition noise by confining the atoms in periodically generated potential wells. This method enables more precise atomic clocks based on neutral atoms with optical transitions.

1.3 Long Term Motivation – Strontium Optical Clock & Lattice Magic Wavelength

Current and past research have looked at multiple atom candidates to use in atomic clocks - from ions to neutral atoms and their stable isotopes such as Al^{+}, Yb^{+}, Mg, Ca , Sr [87,88] to name but a few [10]. Optical clock systems using ions have the advantage that their oscillation frequency and optical transition frequency do not overlap, thus the clock signal has less potential noise [10, 11]. The advances in optical lattices confinement have opened the door for neutral atoms such as strontium (Sr^{87}) to be utilized in optical clock systems. The interest for neutral atoms in optical clock systems comparatively to their ion based counterparts lies in their much lower reactivity enabling the use of large number of atoms which increases the signal-to-noise ratio [15]. Alkaline-earth atoms have been selected as promising candidates due to their simple atomic structure [15]. Systems based on the alkaline-earth strontium show great promise due to its availability and the accessibility on the market of laser sources with the corresponding wavelengths to trap, cool and pump the Sr^{87} atoms [11, 15].

So far, we have discussed the benefits of optical clocks versus standard atomic clocks, the importance of optical lattice, the benefits from neutral atoms in a clock system and the promising usage of Sr^{87} as the neutral atom. These lay the required basis for the development motivation of our fiber laser. One of the remaining optical clock concepts before laying the specifications requirement of our laser is the choice of the optical lattice wavelength known as the magic wavelength (MWL) [16]. The magic wavelength is selected as to confine the atoms in a ground state where their fundamental oscillations match the clock state oscillations – the excited state natural oscillation [19]. Thus, reducing the broadening from noise. The optimal wavelength was demonstrated for Sr^{87} atoms by Takamoto M. and al. with a wavelength of 813.420(7) nm [16] with a wavelength stability under 1 pm. Optical lattices are virtual potential wells generated by combining light beams to produce static electromagnetic wave structures in a 2-D or 3-D pattern. These structures have a specific wavelength known as the magic wavelength that reduces the radiation noise from and to the ground state oscillations by matching it to the excited state.

1.4 The Ideal Optical Lattice Light Source: Fibered, Coherent, Single-frequency, High Power, and Single Polarization

Now equipped with a basic understanding of optical lattice we can discuss the required properties the light source generating the lattice must possess. First, this generation process requires coherent light interference which is obtained via the interaction of two or more coherent light sources with the same polarization [20] - giving us the first two specifications of the light source. Second, the structure formed from interference needs to be periodic, meaning that the resulting field must maintain a uniform wavelength – each trapped atom must experience the same potential confinement. The interference of two monochromatic beams of frequency ω_0, e.g., in a Mach-Zehnder interferometer, results in a static interference pattern with the same frequency ω_0 [21]. This leads to the third specification, monochromaticity. Single-frequency lasers can reach kHz-MHz linewidths and possess a long coherence length making them ideal candidates for generating optical lattices. Section 1.3 introduced the critical role of the MWL in atom confinement noise reduction. Although the wavelength is the predominant parameter, the broadening of each state is a function of the atomic polarizability $\alpha_k(\omega, \boldsymbol{e})$. The polarizability α of the atomic state $|k\rangle$ depends on the frequency ω (MWL) and the polarization vector $\boldsymbol{e}$. This polarization dependence comes from the dipole nature of atoms. Although neutral in charge, atoms can carry a dipole due to the uneven distribution of electrons around the nuclei – thus their confinement response varies with the polarization vector. Minimizing the light shift noise between the ground and clock state consequently comes from minimizing the polarizability difference $\Delta\alpha(\omega, \boldsymbol{e})$ between both states [16, 19] further increasing the polarization requirement. The fourth requirements for the laser can be extracted from the polarization dependence. The laser needs to be polarized and given the atomic polarizability of strontium at precisely 813.420(7) nm, for large atomic numbers it requires an output power of a few watts [22].

Multiple designs for lasers with an output wavelength of 813.420(7) nm are plausible such as semiconductor lasers, crystal lasers and fiber lasers. A state-of-the-art review on 813 nm sources for Sr^{87} MWL generation is presented in section 2.5. Optical clocks and optical lattices are a vast subject with important details outside the scope of this thesis – for a more in-depth explanation we refer the reader to [10].

1.5 Research Objectives

1.5.1 Research Partner – MPB Communications Inc.

This research was funded and done in partnership with MPB Communications Inc. MPB Communications (MPBC) is an international leading supplier and innovator for fiber lasers, fiber amplifiers and amplifier sub-systems located on the island of Montreal, Quebec. Committed to continuous R&D, MPB aims to maintain a leadership role in the ever-changing photonics and high technology market.

1.5.2 Objectives

The research objective presented in this thesis is the development of a narrow linewidth single mode linearly polarized DFB laser operating at 1742 nm in a thulium doped polarization maintaining (PM) fiber. This thulium doped fiber (TDF) laser is critical in the development of a fully fibered high power 813 nm SF laser. The MWL laser is an integration system combination with the TDF laser, and an erbium doped fiber (EDF) laser using non-linear wave mixing. This system is to be integrated by MPB. The high-power specification for the optical lattice application is achieved by the integration system, in a MOPA configuration; the MOPA design requires a minimal output power specification of 1 mW from the DFB laser. The main objective can be divided into smaller secondary objectives. **(1)** Conceive an operational PS DFB laser in PM TDF. **(2)** Simulate the single polarization (SP) design spectral responses from the external cavity length, phase relation and temperature; dual polarization lasing is expected in PM fiber but undesired for MWL applications, with more details in section 2.2.1. **(3)** Develop and conceive the fiber design to achieve SP laser operation **(4)** Demonstrate the selected SP design robustness. **(5)** Demonstrate stable SP single frequency (SF) laser operation, i.e., <1 pm fluctuation with a minimum output power of 1 mW.

1.5.3 Achievement

To the best of our knowledge this research has achieved a previously undemonstrated single-polarization single-frequency design based on a phase-shift DFB laser in PM fiber with an external non-PM FBG reflector. With robust SP operation, an 8 MHz linewidth or 81 fm and a stability

under 0.3 pm at 1742 nm, this source makes a great additional tool in SPSF fiber laser designs and enables fully fibered polarization selectivity. The laser is pumped at 1575 nm using a CW Er:Yb laser. It achieves 1.5 mW output power for 460 mW pump power and maintains SPSF operation while temperature or strain tuned over 11 GHz.

1.6 Thesis Outline

This thesis is divided into 6 chapters. Chapter 2 provides scientific background relevant to the thesis with 5 main themes: fiber Bragg gratings, thulium doped fiber, DFB lasers, a state-of-the-art review on SPSF operation in fiber lasers and lastly an overview on other 813 nm generation sources. Chapter 3 presents the experimental methodology tied to the realization of the research objectives. The experimental approach is explained with the appropriate measurement methods and presents the characterization equipment used. Chapter 4 presents the experimental results starting with the ones tied to the PS DFB grating conception, followed by simulations of the SPSF design and then an in-depth characterization of our laser operating in a SPSF regime. In Chapter 5 the laser characterization results, and the challenges overcome are discussed and put in perspective to the state-of-the-art presented in Chapter 2. The objectives are also revisited with future improvements. Finally, Chapter 6 concludes the thesis with a global portrait on the work and objectives.

CHAPTER 2 LITERATURE REVIEW

2.1 Fiber Bragg Gratings (FBGs)

Discovered inadvertently in 1978 by Hill et al. [23], FBGs are now an indispensable part of optical fiber technologies. Their applications range from communication systems, sensing applications and, more importantly to this thesis, to fully fibered lasers [24]. They enable the creation of a resonant cavity, critical to lasers – acting as wavelength selective reflective mirrors within the fiber waveguide. Their properties have been carefully studied over the years and their spectral response can be simulated using the transfer matrix method [25], employed by simulation tools in this section.

2.1.1 Principle of operation

FBGs are periodic diffractive structures over a fix length within the fiber core. These diffractive structures known as gratings are induced by a modulated variation of the refractive index (RI) in the waveguide. Using the principle of momentum conservation from an incident light arriving perpendicularly to the grating structure in optical fiber and reflected into the core [26, 27], one can obtain equation **(2.1)**:

$$-\beta_r = \beta_i - \beta_g \tag{2.1}$$

Where β_r, β_i and β_g are the propagation constant of the reflected light, incident light and periodic grating respectively, in a lossless medium. The reflected light has a negative sign due to its backward propagation relative to its incident counterpart. The negative sign of the FBG propagation constant can be understood as the loss of momentum encountered by the incident light and transferred back to the reflected light when interacting with the inscribed grating. The propagation constants are defined such as:

$$\beta_{i,r} = \frac{2\pi n_{eff}}{\lambda} \; and \; \beta_g = \frac{2\pi}{\Lambda} \tag{2.2}$$

Where n_{eff} is the effective refractive index, λ is the vacuum wavelength of incident and reflected light and Λ is the grating period. Inserting equation **(2.2)** in equation **(2.1)** one obtains the Bragg condition equation:

$$m\lambda_B = 2n_{eff}\Lambda \qquad \textbf{(2.3)}$$

Where λ_B is the central phase matching wavelength known as the Bragg wavelength and m is the Bragg order of diffraction, typically $m = 1$ [24]. A schematic of the FBG operating principle is presented in Figure 2-1.

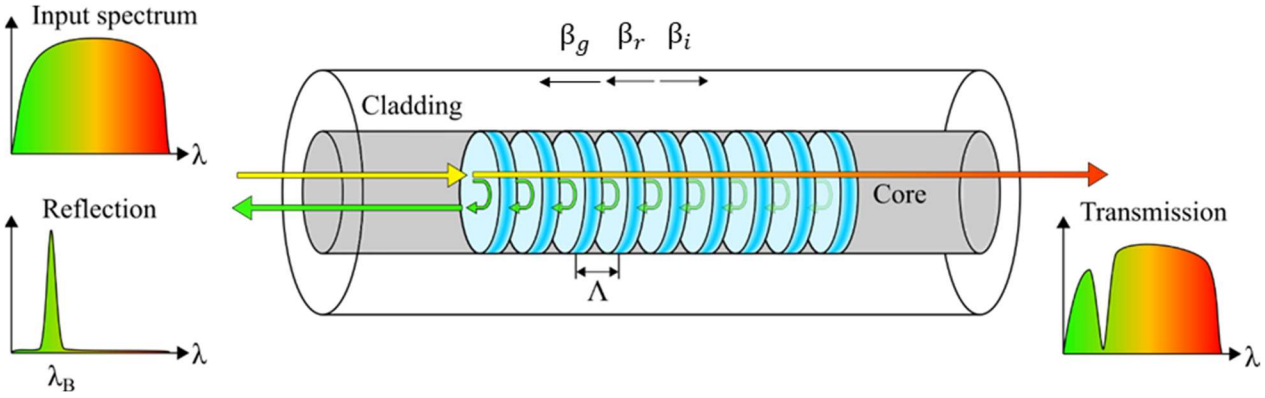

Figure 2-1 Fiber Bragg grating schematic. An input spectrum propagates in the fiber core. As the input encounters the RI variations at Λ intervals the Bragg mode, centered at λ_B, respecting the phase matching condition is reflected over the length of the grating while non-resonant modes are guided through without perturbation. © 2022 A. Roberge [28], reproduced with permission

2.1.2 Photosensitivity

In specific controlled conditions, irradiated fiber can have its refractive index changed permanently. This process known as photosensitivity is responsible for the creation of fiber Bragg gratings. A simplified model to explain this process can be obtained using the Kramers-Kronig relation shown in equation **(2.4)**. This equation links the real part of a complex number, the RI index in this case, to its imaginary part [26, 29]:

$$\Delta n(\lambda) = \frac{1}{(2\pi)^2} \int_{\lambda_2}^{\lambda_1} \frac{\Delta\alpha(\lambda')\lambda^2}{(\lambda^2 - \lambda'^2)} d\lambda' \quad \textbf{(2.4)}$$

Where Δn is the refractive index change, λ is the wavelength at which the refractive index change occurs, $\Delta\alpha$ is the absorption coefficient variation - linked to the RI imaginary part, λ' is the source wavelength used for RI modulation. Finally, $\lambda_2 < \lambda' < \lambda_1$ is the spectrum relative to the absorption change. A typical wavelength λ' used in FBG inscription is UV light. In this electromagnetic region, the induced change in the absorption, or imaginary part of the refractive index affects its real part in the IR spectrum [26, 29].

Photosensitivity mechanism is complex and depends on both the irradiation conditions and fiber composition this includes wavelength, intensity, total dosage, impurities, mechanical structure, and dopants for the fiber composition to name but a few [23, 27].

A key element in the inscription of FBGs abundantly used is fiber dopants to enhance UV photosensitivity – one preeminent dopant being Germanium [24]. Introduced by modified chemical vapor deposition during the preform fabrication process, these dopants create defects in the lattice structure of glass. Once exposed to specific UV light absorption bands, 213 nm or 280 nm for example, for standard SiO_2 Ge co-doped fiber, it leads to the creation of new defects by a single photon process which increases the absorption and thus the refractive index modulation. These defects are known as color centers. The RI change induced by this UV-light process leads to Type I gratings. A higher energy process from a multi-photon absorption is also possible, it has the Type II denomination and usually requires pulsed lasers [24, 29].

In addition to Ge doping, another method to enhance Type I fiber photosensitivity consists of having hydrogen present in the fiber core before writing. This is done by loading the fiber with deuterium or hydrogen atoms in pressured chambers via diffusion. Once loaded, fibers must be kept at low temperature to reduce outer diffusion at ambient pressure. This process increases the probability of new color center defects at the cost of increased absorption near ~1.4 μm for hydrogen and ~1.9 μm for deuterium due to newly formed bonds with hydrogen. [27]

2.1.3 Annealing

Just like for a metal, annealing glass consists of heating the material and letting it cool down in a controlled environment. The annealing process of fiber following the inscription of Type I grating plays two essential roles. First, it unloads the deuterium or hydrogen left in the fiber core. When splicing fiber, the heat generated through fusing causes the gas to expand and greatly disables the ability to properly splice fibers and can damage the splicing machine over time. When done at room temperature and atmospheric pressure unloading the fiber gas can take weeks before being able to properly splice the fiber. This unloading also needs to be considered for the Bragg wavelength as it reduces the glass density and thus reduces n_{eff}. This translates into a shift of the Bragg wavelength to lower wavelength values. Second, Type I gratings are more susceptible to have a decay in time of their refractive index. This is especially true at higher temperatures where the decay is amplified. Annealing the grating makes the induced refractive index more robust to further decays [24].

2.1.4 Fabrication methods

Fiber Bragg grating fabrication can be categorized into two main categories related to the photosensitivity process involved. The first category uses the one photon absorption process - creating additional defects in the glass - color centers. The second fabrication method uses the multi-photon absorption process. The following section presents both fabrication methods related to each photosensitivity process.

2.1.4.1 Single photon – UV writing

The one photon process method requires a high enough energy photon which can interact with the fiber core to create color centers. This is typically performed using emission bands in the UV regime and relies on an interference pattern projection on the fiber core to obtain the desired grating period [26]. This method requires the fiber to be stripped of its protective coating due to its high absorption in the UV regime.

Figure 2-2 presents a schematic of the writing setup used for DFB gratings inscription – a modified Talbot interferometer. A phase mask is placed with normal incidence to the UV light. The ± 1 orders of diffraction are aligned with phase modulators [29]. The sawtooth wave from the

modulators is synchronized with the moving fiber on air-bearing stage for continuous writing. Mirrors redirect the modulated light on the fiber core to form an interference fringe pattern.

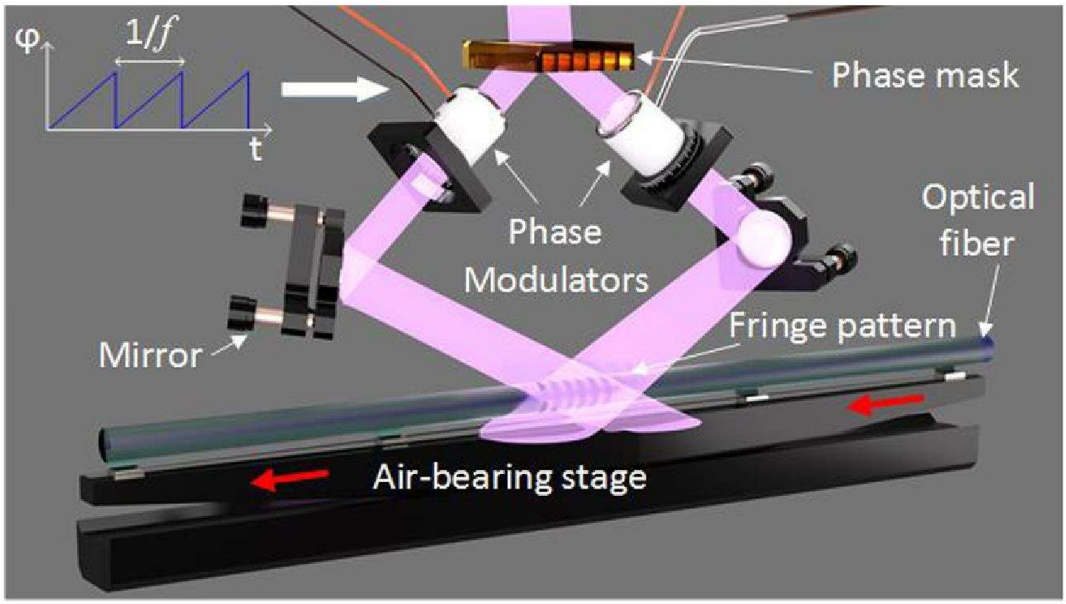

Figure 2-2 Fiber Bragg writing station – modified Talbot interferometer schematic. © 2018 S. Loranger [27], reproduced with permission.

Phase masks are made from silica wafers via micro-fabrication process and are a common robust tool in FBG writing to obtain diffraction orders. Their diffracted light can be used directly to write gratings or recombined using mirrors, the configuration used in the current thesis to write FBGs. This setup offers high versatility enabling the Bragg wavelength to be independent of the phase mask period [24]. The corresponding Bragg wavelength is given by [27]:

$$\lambda_B = \frac{2n_{eff}v}{f} \tag{2.5}$$

Where v is the fiber translation speed and f the sawtooth wave function frequency. In more basic FBG writing stations utilizing phase masks, the Bragg wavelength λ_B is proportional to the phase mask slit period Λ_{PM} which limits the versatility of the desired reflected central wavelength and could require multiple phase mask interchanged to achieve a broad selection of wavelengths [30]. Whereas equation **(2.5)** displays the versatility of the setup effectively removing the phase mask periodicity dependence.

Typical FBG writing phase mask setups are physically limited to ~10 cm FBG in length [31]. One of the main challenges of such long FBGs is to maintain good modulation uniformity throughout the length of their writing process. Multiple setups can achieve longer writing but are often unpractical [29]. The current writing setup used for this thesis work was initially reported by M. Gagné et al. [31] reaching FBGs up to 1 m long in SMF-28 fiber. Work by S. Loranger et al. [32] improved the setup achieving the same writing length in specialty fiber with a mapping and correction of the RI leading to more robust complex structures such as DFB gratings.

2.1.4.2 Multi-photon – Femtosecond writing

The other process for FBG inscription involves a multi-photon absorption. Due to the multi-photon absorption process where the band gap energy is achieved from the sum of multiple photons energy, a pulsed laser is typically used in FBG inscription - more specifically IR femtosecond lasers. This offers the possibility for inscription through the polymer protective coating contrary to single photon UV writing [33].The RI modulation from this process is not solely due to the creation of color center, as such the need to load the fiber with deuterium or hydrogen is irrelevant. The multi-photon process high energy burst densifies the fiber core from new atomic bonds and also leads to the creation of color centers in material [24]. There exist multiple schemes for femtosecond laser inscriptions such as point-by-point, plane-by-plane and line-by-line writing. Their respective advantages and disadvantages go beyond the scope of this thesis; however, a common characteristic for all femtosecond writing is the high alignment precision requirement with the fiber core comparatively to the interference projection for UV writing. This makes the inscription of longer FBGs more challenging [33].

2.1.5 Refractive index modulation

The effective refractive index over the propagation axis z from the induced RI modulation can be modeled as [27]:

$$\mathrm{n(z)} = \mathrm{n_0} + \overline{\Delta n}(z)\left(1 + v(z)\cos\left(\frac{2\pi z}{\Lambda} + \phi(z)\right)\right) \tag{2.6}$$

Where n_0 is the effective RI of the mode pre-inscription, $\overline{\Delta n}(z)$ is the average component of the modulated RI, the product $\overline{\Delta n}(z)v = \Delta n(z)$ is the modulated RI amplitude, Λ is the grating period and $\phi(z)$ any other phase variation over the grating length, such as a phase shift. Lastly, $v(z)$ is the modulation visibility $(0 \leq v \leq 1)$ and is associated with the FBG writing process known as apodization. Figure 2-3 presents a schematic of the different parameters [27].

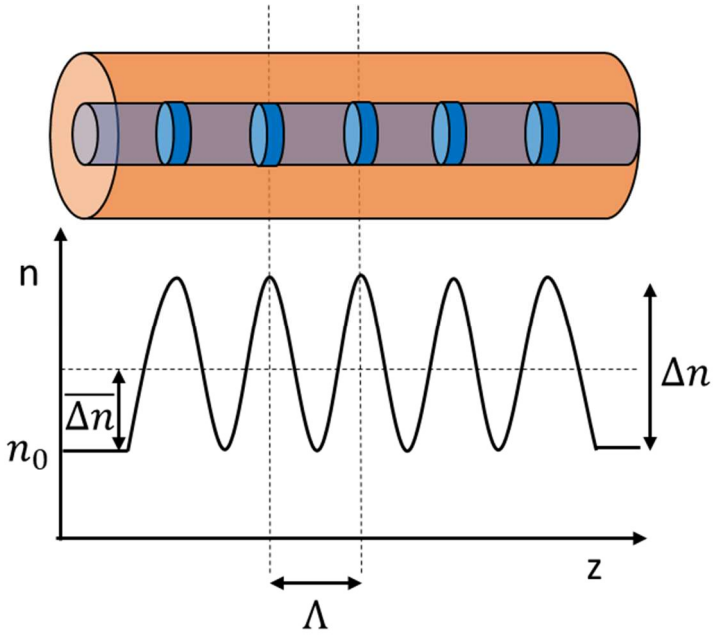

Figure 2-3 Refractive index modulation schematic for a uniform FBG.

2.1.6 Apodization

The visibility $v(z)$ in equation **(2.6)** is utilized during the inscription for apodizing the grating. An explanation for apodization is to consider the following: the Fourier transform of a rectangular shape such as the RI modulation profile in Figure 2-3, is a sinus cardinal profile in the spectral domain. This leads to side lobes in the reflection spectrum of the grating, undesired for SF laser applications as seen in Figure 2-4 a). They can be reduced or eliminated with a proper choice of the visibility function for the RI modulation to impact its spectral domain, this process is called apodization. We observe its effect in Figure 2-4 b) where the simulated apodized grating side lobes have over ~30 dB attenuation comparatively to the non-apodized grating. Typical apodization functions include Gaussian, cosine and tanh [34].

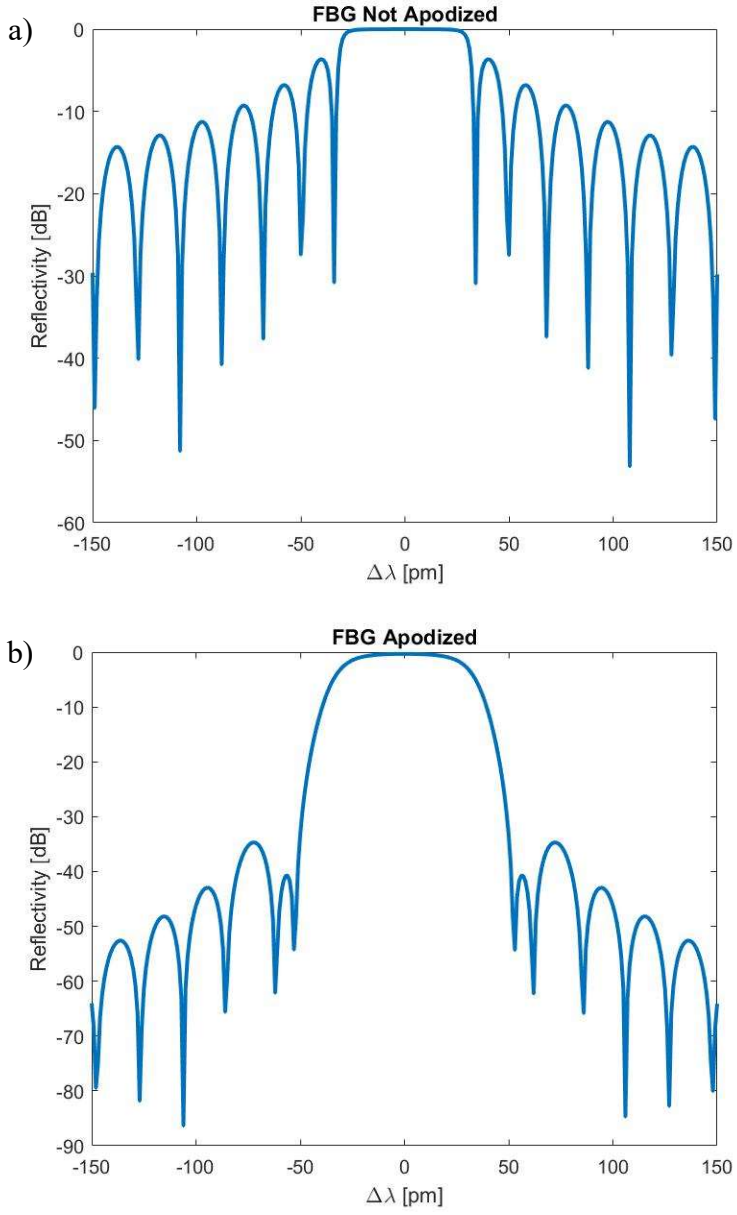

Figure 2-4 Simulated FBGs reflection spectra a) 0% apodization b) 100% apodization. Gratings parameters: length 5 cm, κ_{ac} = 80 m^{-1}, cosine apodization and central wavelength 1746 nm.

2.1.7 Grating reflectivity and strength

The number of photons coupled in the counterpropagating direction of the incident light is known as the grating strength – its reflectivity. The reflectivity is a function of two parameters: the grating RI modulation and the grating length [24], and is given by the following equation:

$$R = \tanh^2(\kappa_{ac} L) \quad \textbf{(2.7)}$$

Where R is the reflectivity at the grating central wavelength, κ_{ac} is the ac coupling constant, proportional to the RI modulation Δn, and L is the grating length. The product κL is known as the grating strength. From equation **(2.7)**, we can see how a higher refractive index modulation will increase the grating reflectivity due to $\kappa_{ac} \propto \Delta n$; more photons are coupled in the counter-propagating mode. Similarly, a longer grating will enable more photons to couple in the counter-propagating mode leading in both cases in an increased reflectivity.

2.2 Thulium Doper Fiber

Like other rare earth elements such as erbium, ytterbium or neodymium, thulium ions are commonly used to dope glass fiber cores for fiber lasers and fiber amplifiers applications. The ions enable stimulated emission where absorbed pump light is re-emitted at a lower energy. The main gain bandwidth from thulium ions in silica (Tm^{3+}) ranges from 1.7 μm to 2.1 μm peaking near 1.85 μm; a continuation of the highly used erbium ions with a bandwidth ranging from 1.52 μm to 1.61 μm [35]. Thulium doped fiber (TDF) gain bandwidth has opened multiple fiber-based applications from the medical field due to high water absorption near the 2 μm region [36], to near-infrared spectroscopy [37] and many others as this new bandwidth enables new wavelengths through frequency mixing previously unattainable.

The new frequency reach is highlighted in this research via its optical clock application for a high power fully fibered single frequency linearly polarized source for a Sr^{87} optical lattice generation. The required SF laser wavelength of 813 nm can be achieved with a sum frequency generation process of 1535 nm and 1730 nm laser, both achievable with erbium doped fiber and and TDF respectively. Figure 2-5 presents TDF main ground state absorption and emission energy levels with their respective central wavelengths [35, 38]. Figure 2-5 shows TDF has three potential

wavelengths for pumping. The 1210 nm absorption band encompasses 1064 nm, this is highly relevant as ytterbium fiber lasers are well known and available at 1064 nm capable of reaching high power outputs [35]. However, this absorption band is prone to undesired excited state pump absorption due to upconversion resonance. This upconversion is a three photons absorption process starting from the ground state (Figure 2-5 in orange). This leads to a blue light emission from radiative transition between the $^1G_4$ state to the $^3H_6$ ground state.

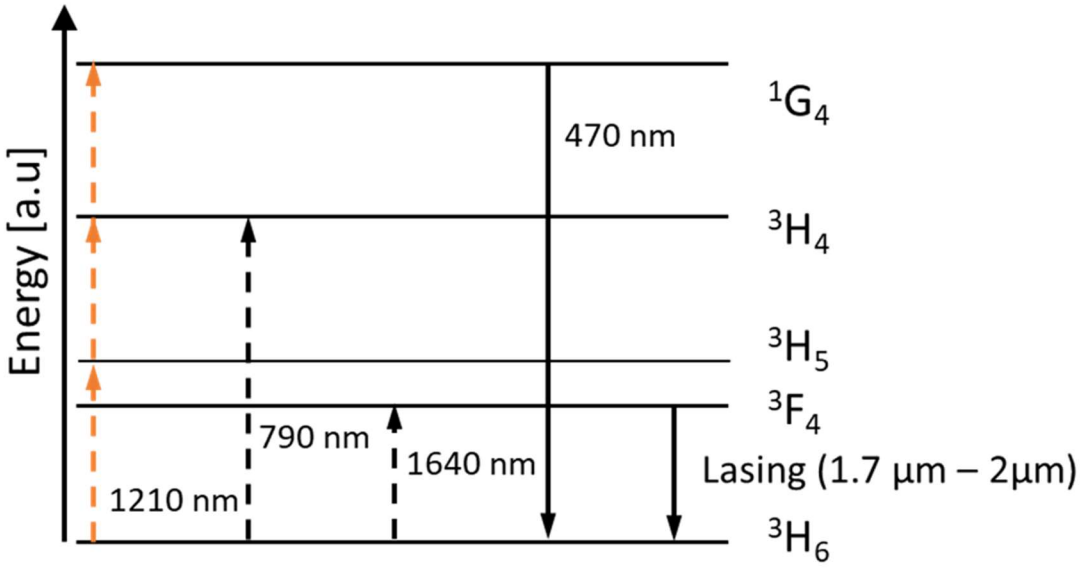

Figure 2-5 Thulium energy level in fiber glass. Absorption levels in dashed lines and emission levels in straight lines with their respective central wavelength, and orange line: 3 photons absorption process. Inspired from [35].

Another option is pumping in the 790 nm band. This band can be achieved by Ti:Sapph lasers and semiconductor laser diodes such as InGaAs. Semiconductor laser diodes (LDs) are usually preferred over their Ti:Sapph lasers counterparts in this band as they provide a fully fibered pump and are less complex system. This absorption band cannot achieve direct resonance with the $^1G_4$ state. However, combined with other energy transfer mechanisms present in rare-earth doped fiber such as energy transfer from ion clusters, the undesired upconversion to the $^1G_4$ state can occur. The last absorption band is the 1640 nm centered band, which encompasses the L-band (~ 1565 nm – 1625 nm) generated with erbium doped fiber (EDF) lasers where high power is achievable in a double cladding or MOPA configuration. Figure 2-6 presents the a broad absorption spectrum in

a thulium aluminum co-doped fiber [35]. The 790 nm band has the highest absorption, while 1200 nm and 1640 nm bands have similar peak absorption, but the latter has a much broader band.

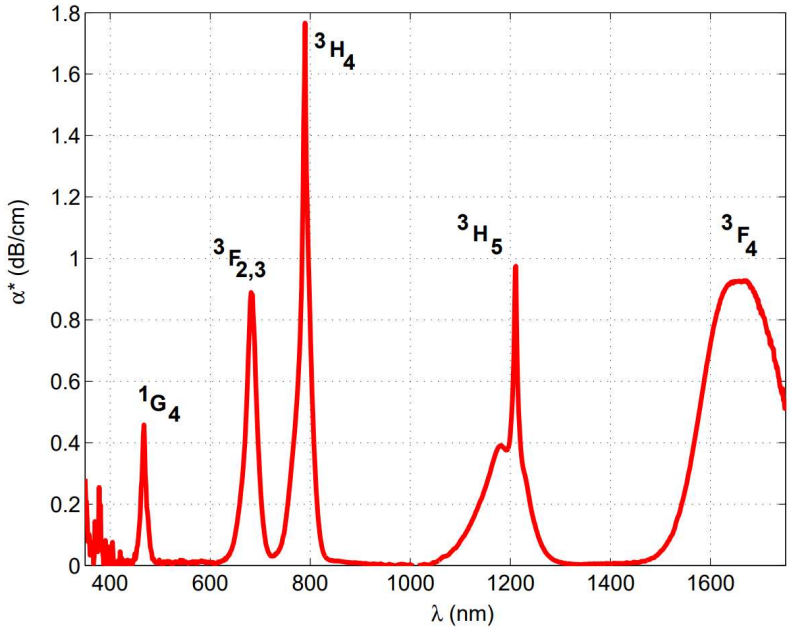

Figure 2-6 Absorption spectrum of thulium and aluminium co-doped fiber. © 2006 S. Agger [35], reproduced with permission.

The lower energy end tail of the L-band reduces excited state absorption, as such it is desirable to increase the pumping wavelength in the L-band. Furthermore, as seen in Figure 2-7, TDF absorption is also increased deeper in the L-band. However, a trade off is required as EDF imposes gain limitations at longer wavelengths of the L-band [39]. Finally, TDF absorption band overlaps with the $^3F_4$ - $^3H_6$ signal emission band, where the ground state absorption at 1735 nm was measured to be 0.4 dB/cm [38]. This favors lasing at longer wavelengths near 1.9 μm over 1.7 μm emission.

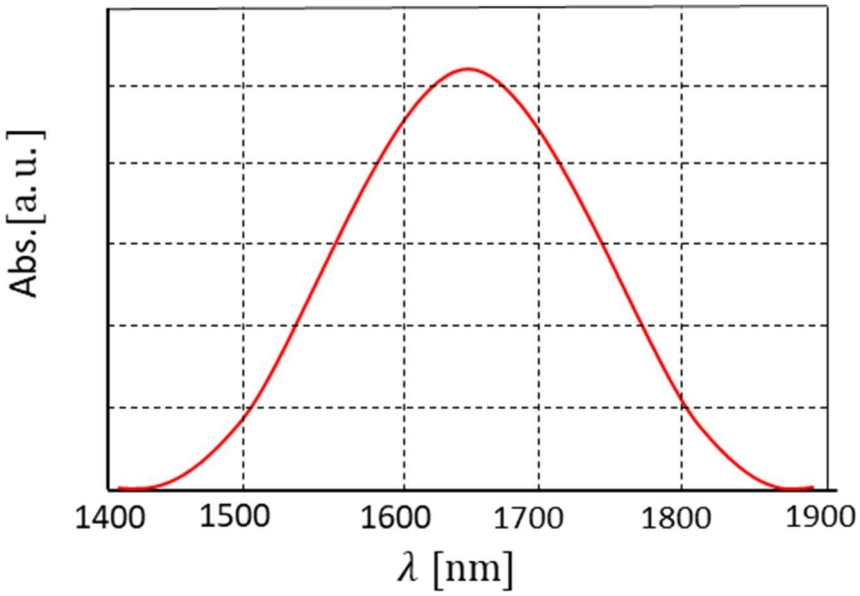

Figure 2-7 Thulium doped fiber absorption spectrum near 1.65 µm. Inspired from [39].

However, unlike EDF and YDF whose main emission band's quantum efficiency is close to 100%, TDF quantum efficiency for the $^3F_4$ state is closer to 10% and even lower for other transition emissions [40]. The quantum efficiency η of fluorescence for an atomic state is defined by:

$$\eta = \frac{Nb.\ photons\ emitted\ via\ fluorescence}{Nb.of\ photons\ absorbed} \quad \textbf{(2.8)}$$

Ideally the decay from the excited state is purely from spontaneous emission, however quenching effects such as clustering and non-radiative decay can reduce its lifetime and thus the number of photons emitted via fluorescence from the $^3F_4$ state the population. To achieve the population inversion threshold the laser requires more pump power. With the quantum efficiency of fluorescence proportional to the excited state lifetime this negatively affects Tm sources by significantly increasing their lasing threshold.

Increasing Tm ion concentration can increase gain and quantum efficiency but also the tendency for ions to form cluster which reduces the quantum efficiency. Co-doping TDF with aluminum has shown to increase the quantum efficiency by reducing the formation of ion clusters, enabling a higher quantum efficiency in TDF capable of reaching 40% [41]. Co-dopants in rare-earth doped fiber can reduce cluster formations and it has been shown that Tm fiber co-dopants concentration

can shift its emission peaks to favorize shorter wavelengths, with germanium, and longer wavelength, with aluminium [38]. These co-dopants can also lead to more efficient sources outside of the 1.7 μm - 2 μm band in TDF (see section 2.5).

2.2.1 Polarization maintaining fiber

Maintaining light polarized as it propagates through the fiber is a required specification of the fiber laser design from the polarization dependence of the optical lattice. In fiber this can be achieved by inducing a strong birefringence using a bow-tie or panda fiber design. These fibers are known as polarization maintaining (PM) fiber and are an attractive tool to maintain a linearly polarized propagating light. Panda fiber has two cylindrical rods parallel to the fiber core axis which induce a strong birefringence forcing the guided modes to propagate as two orthogonal polarization modes [42], see Figure 2-8. Bow-tie fiber functions similarly, but the rods' structure shape is a trapezoidal prism instead. One main challenge arises when designing a SF laser with PM fiber. The modes in each axes experience a different effective refractive index. Recalling equation **(2.3)** which dictates the resonant wavelength, we have $\lambda_B = 2n_{eff}\Lambda$. The induced birefringence is characterized by a refractive index difference Δn. The PM TDF selected in this research has a birefringence specification $\Delta n > 2\times10^{-4}$. Hence, FBG inscription for a constant step Λ in PM fiber leads to two resonant wavelength peaks separated by $\Delta\lambda_B > 0.24$ nm for a central wavelength of 1742 nm. The shorter wavelength peak is the fast axis while the longer wavelength peak is the slow axis – these denominations are from the electromagnetic (EM) wave speed propagation in the waveguide relate to their respective effective refractive index as EM wave velocity v = c/n. This birefringence is undesirable for SF operation, as the laser then operates in a dual polarization regime or multimode

regime. Section 2.4 presents a state-of-the-art on fiber designs for single polarization single frequency laser operation (SPSF).

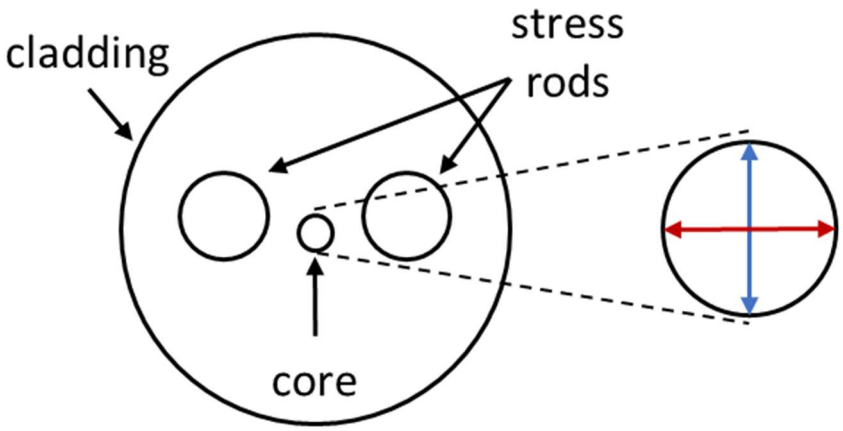

Figure 2-8 Panda fiber transverse view schematic. The stress rods induce a strong birefringence resulting in two propagating linear polarizations, blue: fast axis and red: slow axis.

2.3 Distributed-Feedback Lasers

Distributed feedback lasers play key roles in single frequency laser applications. First developed in semiconductor lasers and subsequently in optical fiber, both technologies rely on the same fundamental principle: wavelength discrimination for the longitudinal modes is distributed over the cavity length added to the laser feedback, hence the name distributed-feedback laser [43]. This discrimination is the fundamental tool leading to single frequency operation with linewidths typically in MHz range for semiconductor DFBs and in MHz down to kHz range for their fibered counterpart [7]. Although limited in output power, there have been multiple reports of DFB lasers amplified in a MOPA configuration with PM thulium fiber [44, 45]. One instance reaching hundreds of watts in power while preserving the SF operation and MHz linewidth properties with a 2 μm DFB LD seed [45]. The following section presents concepts on PS-DFB fiber laser fundamental to the thesis understanding. Other SF laser mechanisms are also briefly presented such as DFB semiconductor laser and short cavity lasers (DBR lasers).

2.3.1 Fibered DFB Lasers

Inherently, fiber lasers provide great advantages thus inherited by fibered DFB lasers. They offer robust operation, compact designs, great beam quality and a low system maintenance without alignment requirement [7]. They also present several advantages over their semiconductor (SC) counterparts, see section 2.3.5, such as better stability, narrower linewidth, and better reliability [46]. DFB fiber lasers can be categorized into two main branches distinguished by their gain mechanism. For the first branch, the gain is provided by rare-earth dopants such as erbium, ytterbium, and thulium to name but a few. For the second branch, the gain is provided by non-linear processes such as stimulated Raman scattering. SRS is a non-linear process where vibrational energies from polar molecules are re-emitted at fixed frequency shifts of lower energy. Although interesting with their wide lasing wavelength selection theoretically not limited by rare-earth emission spectra, SRS silica-based fiber lasers offer poor gain comparatively to their rare-earths counterpart and are more susceptible to undesired non-linear effects [47]. For high power, rare-earth based fiber lasers have a reduced design complexity since the same rare-earth doped fiber can be used for its amplification. The main parameter affecting lasing threshold in DFB fiber laser has been demonstrated to be the grating strength [48] – the laser cavity threshold increases exponentially with a reduction in its strength. Better phase control allows lengths up to tens of cm [48] to be possible. Thus, DFB lasers can operate at a lower lasing threshold with a constant RI modulation. A reduced threshold is desired as it lowers the pump power required and hence also reduces the heat impact in the cavity from the quantum defect as well as reducing power consumption.

The first successful lasing wavelength near ~1.7 μm in TDF using a phase-shifted DFB laser design was achieved in 2004 by Søren Agger with a laser operating at 1735 nm [38]. The grating length was 4.7 cm with a $\kappa \approx 220\ m^{-1}$ giving a grating strength (κL) ≈ 11 . Operating in a single-polarization single-frequency regime, the DFB cavity with 600 mW pump power at a wavelength of 790 nm from a Ti:Sapph laser reported a maximum output lasing power of 1 mW.

2.3.2 Structure

A typical fiber lasers structure is comprised of a fiber gain media with resonant reflectors, i.e., FBGs, at both of its end. In its simplest form a distributed-feedback mechanism can be achieved in

fiber by inscribing a single uniform FBG in the gain media. In this configuration the feedback mechanism leads to two main resonant modes. The highest Q-factors modes are located at the edges of the stop band [25, 27] as seen in Figure 2-9 a), negating SF operation. This multimode operation is overcome by introducing a π-phase shift during the inscription process [27, 49]. We also observe lower side lobes due to the square shape This new configuration introduces a transmission peak within the bandgap of a few GHz – the high Q-factor modes change from lateral to a single central mode enabling single frequency operation as seen in Figure 2-9 b).

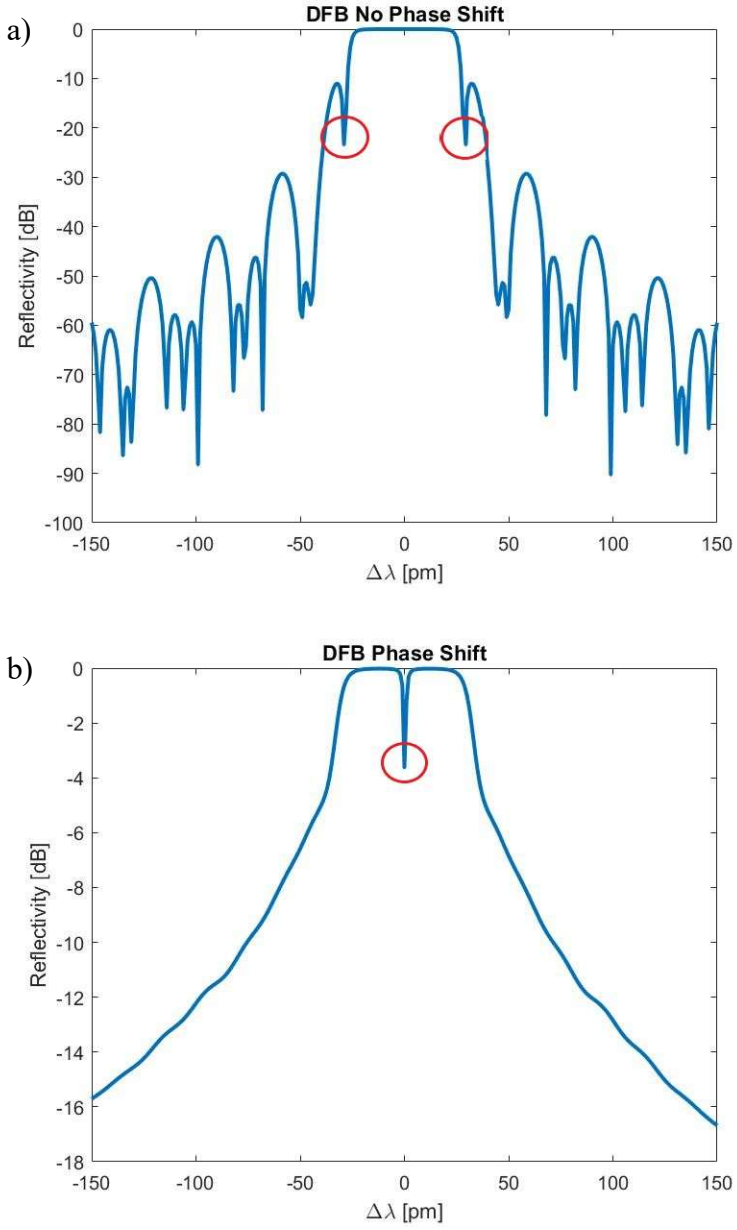

Figure 2-9 Reflection spectra for simulated fiber DFB gratings a) without a phase shift and b) with a π-phase shift at 55% grating length. Red circles highlight the favorize lasing mode(s). Grating parameters: length 10 cm, κ_{ac} = 64 m^{-1}, 70% cosine apodization and central wavelength 1746 nm.

2.3.3 Q-factor

The quality factor is commonly used to characterize the quality of an optical resonator. It is defined by the ratio [21]:

$$Q = 2\pi \frac{stored\ energy}{energy\ loss\ per\ cycle} = \frac{\boldsymbol{E}}{\boldsymbol{E}c\alpha_r} \tag{2.9}$$

Where **E** is the cavity stored energy, cα_r**E** is the energy lost rate per unit time with c the speed of light and α_r is the total loss defined as:

$$\alpha_r = \alpha_s + \frac{1}{2nL} ln\left(\frac{1}{R_1 R_2}\right) \tag{2.10}$$

Where $\alpha_s$is the coefficient associated to absorption and background losses from the medium, n is the refractive index, L the cavity length and $R_{1,2}$ the reflectivity of mirror 1 and 2 respectively.

Equation **(2.9)** can be rewritten for a cycle of the optical field ($c\boldsymbol{E}\alpha_r/\nu_0$) [21] and it then becomes:

$$Q = \frac{2\pi\nu_0}{c\alpha_r} = \frac{\nu_0}{\delta\nu} \tag{2.11}$$

Where ν_0 is a resonant mode frequency of the cavity and $\delta\nu$ its full width at half maximum (FWHM). From equation **(2.11)** we can observe how the Q factor is dependent on the total resonator losses – smaller losses will result in a higher Q factor whether the smaller losses be from the medium via α_s, or via the cavity mirrors $R_{1,2}$, see equation **(2.10)**. The Q-factor can also be defined as a function of the cavity photon lifetime τ_p [21, 50] with:

$$Q = 2\pi\nu_0\tau_p \tag{2.12}$$

From equation **(2.12)** we see how the Q-factor is proportional to the photon lifetime in the cavity, this is in agreement with equation **(2.11)**; loss reduction increases the cavity lifetime of photons increasing the quality factor just like an increase in the resonator length L. Thus, the Q-factor dictates which modes are favored within the cavity as well as the laser linewidth.

2.3.4 Phase shift grating

Fiber Bragg gratings with phase shift(s) have been studied since the mid 90's for their transmission peak within the FBG stop band in applications ranging from demultiplexers [51], sensors [52] and SF lasers [38, 48, 53]. The phase-shift can be permanently inscribed in the grating structure during the writing process [54] or temporarily induced with a mechanical stress [55] or a temperature variation [56]. The application for a robust, compact, and fully fibered DFB laser in this research project led to the selection of a permanent phase shift inscription method. The permanent phase shift in the TDF grating can be modeled for a localized phase shift as:

$$\phi(z) = \begin{matrix} 0 & z < z_{shift} \\ \phi_{shift} & z \geq z_{shif} \end{matrix}$$

Where $\phi(z)$ is the phase variation along the grating length from equation **(2.6)**, ϕ_{shift} is the phase shift value and z_{shift} is the phase shift position in the grating.

The phase ϕ of a propagating E.M wave is given by:

$$\phi = \frac{2\pi nL}{\lambda} \qquad \textbf{(2.13)}$$

Where nL product is the optical path (O.P.) comprised of the refractive index n and L is the length traveled, and λ is the wavelength.

To better understand the effect of the phase shift in the grating let us consider its effect on the RI modulation. The refractive index modulation completing a full phase cycle of 2π is equivalent to a period length equal to Λ, the RI period length from equation **(2.3)** selected from the Bragg condition. Adding a phase shift with a value of π, or phase of half a period, is thus equivalent to a period increase of $\Lambda/2$. The same methodology can be applied for different phase shift values. The modified period length creates a discontinuity in the uniform grating resulting in a resonant transmission peak within the FBG stop band as observed in Figure 2-9.

Once a phase-shift is inserted in the DFB grating, the structure can be modeled as two uniform FBGs separated by the half-period discontinuity. With a PS at the center of a grating of length L, such as $z_{shift} = 0.5L$, then the left-hand side and right-hand side gratings, relative to the phase-shift, have the same reflectivity but have a phase difference of π. This configuration maximizes the

Q-factor of the cavity leading to the smallest lasing threshold [57-59]. Thus, when $z_{shift} < 0.5L$ it reduces the reflectivity of the left-hand side FBG creating an output coupler at the expense of a higher threshold from the Q-factor reduction - and when $z_{shift} > 0.5L$ the same occurs for the right-hand side FBG. [57-59]. The effect of the phase-shift value on the FBG spectra is observed in Figure 2-10 for two FBGs spectra simulated with two distinct phase-shift values. The transmission resonance shifts within the stop band from smaller wavelengths to longer wavelengths as the magnitude of the PS increases.

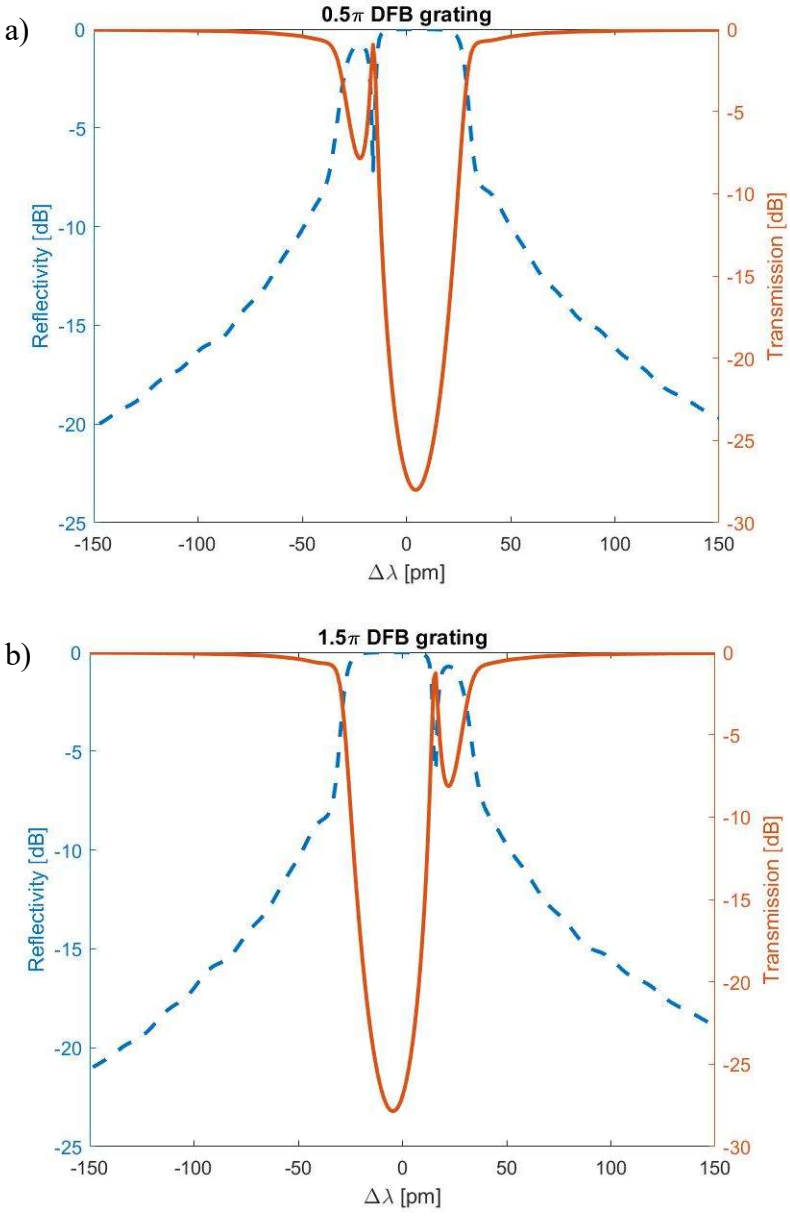

Figure 2-10 Effect of the phase-shift value on a DFB grating transmission and reflection spectrum for a) a PS of 0.5π and b) a PS of 1.5π both centered at 1746 nm. The transmission wavelength resonance shifts towards higher wavelengths as the magnitude of the PS increases.

The phase shift where the transmission peak is centered within the DFB stop band maximizes the Q-factor and minimizes the lasing threshold. This is achieved with a phase shift value of π. Whereas, as seen from Figure 2-10, higher or lower PS values shift the transmission resonance to longer or shorter wavelengths respectively leading to a lower Q-factor.

Once pumped, high intensity in the phase shift region leads to important heating phenomena. The quantum defect induces non-uniform heat from absorption maxed in the phase shift region which negatively impacts the typical PS DFB laser performances [59].The increased temperature in the phase shift region expands the optical cavity which alters the $\Lambda/2$ phase shift required for a single resonant mode potentially enabling other resonant modes to appear. Furthermore, the temperature gradient lowers the Q-factor as the FBG becomes off-tuned with the resonant wavelength over its full length. Lastly, high pump powers can potentially lead to a phase detuning from possible non-linear effects, if the power is large enough. This detuning from the optical Kerr effect could push the lasing mode closer to the stop band edge, which in turn makes it more likely for other under-threshold modes to lase at higher pump powers. However, it has been shown by S. Loranger [59] to be insignificant when compared to the effects of heating from quantum defect and absorption. This further re-enforces selection of the pump wavelength near the 1.6 μm band versus the 0.8 μm band to reduce the impact of the quantum defect in the PS region.

2.3.5 Semiconductor DFB lasers

Semiconductors DFB lasers are small devices with large wavelength emission range from near UV $\sim 400\ nm$ to short-wave infrared $\sim 2\ um$. The most common SC laser structure is known as double hetero-junction which is comprised of two doped semiconductors at the device extremities, one p-type and one n-type. Each doped layer is typically in the tens of μm and in between the p-n junction is an even smaller intrinsic (undoped) semiconductor layer typically $< 1\mu m$ in size which acts as the gain media, see Figure 2-11. Selecting a semiconductor with lower refractive index and higher

band gap for the extremity layers reduces the lasing threshold comparatively to a p-n homojunction semiconductors. The lower RI enables a tighter confinement of the longitudinal mode in the active region while the higher band gap confines the p and n dopants in the active region when pumped [43]. When a certain forward bias voltage is applied typically expressed in its current form, the threshold current, the holes and electrons from each external layer can recombine in the active layer leading to emission. Polishing the edges enables the selection of the direction of the output signal.

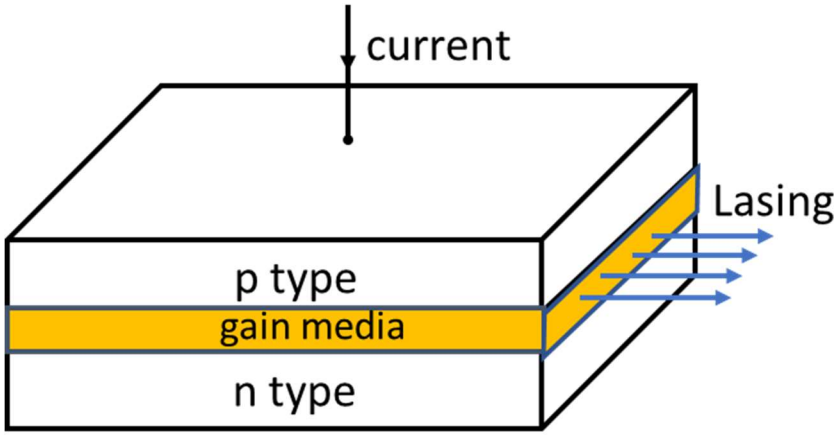

Figure 2-11 Hetero-junction semiconductor laser structure schematic. The p and n-type layers have a lower refractive index than the active region. This enhances the modal confinement in the gain region and lowers the threshold current operation.

Common semiconductors in a hetero-junction structure include InGaAs, InAsP, GaAsP to name but a few. The semiconductor composition and atomic ratios enable a wide selection of wavelength emissions. A PS DFB structure can also be introduced in their built for SF operation by an etching process. However, SC lasers are highly susceptible to temperature, making them inherently more susceptible to noise and thus they have a higher linewidth limitation over their fully fibered counterpart with linewidths in the MHz. These devices are also prone to undesirable leakage current which is electron-hole recombination outside the gain media, hence not participating in the lasing process. This leakage is made more important as the device operation lifetime progresses. [43]

2.3.6 Short-cavity fiber lasers (DBR)

We previously discussed how the DFB fiber resonator lasing modes can be narrowed from 2 modes to 1 mode with the introduction of a π-PS. Another design for longitudinal mode discrimination in fiber are the small cavity fiber lasers, also known as DBR fiber lasers, basically a Fabry-Perot (FP) cavity with a rare-earth doped fiber as the gain medium in-between resonators. Focusing on the cavity section of the laser, one simple design consists of one FBG spliced at each end of the active fiber effectively creating the resonant cavity. As shown in Figure 2-12 where one FBG acts a pure reflector, denoted high reflector (HR), while a lower reflection FBG acts as an output coupler (OC) allowing preferential signal output

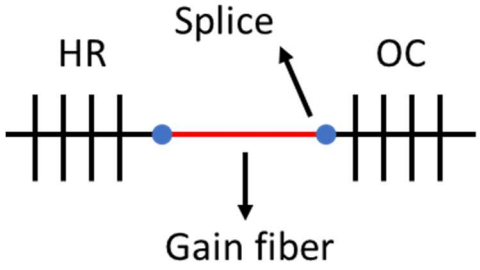

Figure 2-12 Basic short cavity laser design schematic. The gain fiber typically doped with rare-earth is a few cm in length. A small enough cavity with high longitudinal mode discrimination leads to SF operation. The OC FBG enables preferential output.

There are multiple variations possible for this design such as writing one of the gratings in the gain fiber, reducing loss by eliminating one splice point. Their common design remains the same and is based on the discrimination of longitudinal modes within the gain media – relying on high free spectral range (FSR) to ensure SF operation. The free spectral range of a resonator is given by the following equation:

$$FSR = \frac{c}{2n_g L} \tag{2.14}$$

Where c is the speed of light, $n_{g\ is}$ the group index and L is the cavity length. From equation **(2.14)** we observe how a better longitudinal discrimination (high FSR) can occur when L is reduced. Hence, the need for a short cavity length in this design, up to a few centimeters at most. While a

PS-DFB laser length is limited by the RI modulation uniformity over its length, up to tens of cm, DBR fiber laser length is limited by their FSR, up to a few cm. The requirement for a short cavity reduces the available gain [3] and the potential modes in the active region make them susceptible to instability from mode hopping. Jihong Geng et al. demonstrate a non-PM Tm based SF short cavity fiber laser with a 1.95 μm emission wavelength resulting in a kHz linewidth [60]. Their DBR laser was tested with two fiber lengths of 6 cm and 2 cm. The 6 cm cavity yields at minimum 4X the output power compared to its 2 cm counterpart for the same pump power. However, they observed mode hopping at the longer cavity length while none was observed in the 2 cm cavity length.

2.4 Single Frequency Single Polarization Designs

Section 2.2.1 introduced the intrinsic cause of undesired dual polarization operation in PM fiber lasers for single frequency operation. This section presents designs to eliminate the dual polarization for single polarization single frequency (SPSF) operation in a PM fiber laser with a focus on fully fibers design as to preserve the inherent qualities from a fiber system previously presented. Regardless of the design, the common principle behind single polarization operation is the same; manipulation of the polarization dependence of critical factors for laser operation behavior such as reflectivity, loss, gain and birefringence to name but a few [61].

2.4.1 Stress induced single polarization

One method consists of applying stress on the fiber, often the phase shift region. Controlled stress SP operation have been attributed to polarization discrimination or enhancement of multiple parameters in PM or non-PM fiber. The mechanisms for discrimination of a polarization can include, creating leaky modes by modifying the waveguide shape, or increasing modal loss by bending [62] ; another demonstrated mechanism consists of writing PS DFB gratings in PM fiber with a non-π phase shift value. Then by applying a perpendicular pressure, this increased the birefringence by 1 order of magnitude leading to a new PS value closer to π for one of the polarizations enabling SP operation [61]. This mechanism utilizes the Q-factor dependence of the phase-shift value, as previously discussed in section 2.3.4, to favorize one polarization lasing. Although functional, generally low cost, simple and relatively quick to implement; stress induced

methods compromise the fiber mechanical structure and are difficult to reproduce especially in a manufacturing environment.

2.4.2 Thermally induced single polarization

First demonstrated by Babin et al. in 2006, this method was achieved with a 4.5 cm non-PM Yb fiber in a PS DFB configuration. SPSF operation achieves 1.5 mW output power and 10 MHz linewidth [63]. At low pump power the DFB operates in a dual polarization regime, and the modes are separated by 260 MHz, or ~0.9 pm at the signal wavelength of 1 μm (low birefringence). The method consists of polarization loss discrimination due to the non-uniform heat generated from absorption as the pump power increases until SP is achieved. Although simple in its approach, this method as several limitations. The pump power required to break the dual polarization condition is not arbitrary and can vary greatly depending on the fiber non-uniformity, pump power absorption and birefringence. Most of the absorption and thus heat is generated near the phase shift region, hence a cavity chirp is induced with increasing pump powers reducing the cavity efficiency. Lastly, this method cannot reliably select the slow axis or fast axis polarization for its SP operation regime.

2.4.3 Self-injection

The self-injection method relies on favorizing the gain for a specific polarization by reinjecting the desired polarization signal in the PS DFB grating. This process breaks the gain equilibrium and collapses the discriminated polarization when sufficient favorized signal is reinjected. The design relies on rare-earth fiber laser properties of emitting signal in both co-pumped and counter-pumped directions simultaneously. A fully fibered PM design is presented in Figure 2-13. The wavelength division multiplexer (WDM) splits the pump and signal wavelength, an optical isolator (ISO) and circulator prevent undesired back reflection in the cavity. The in-fiber polarizer selects the polarization to be favored in the PS DFB cavity and the circulator enables counter-pump signal output.

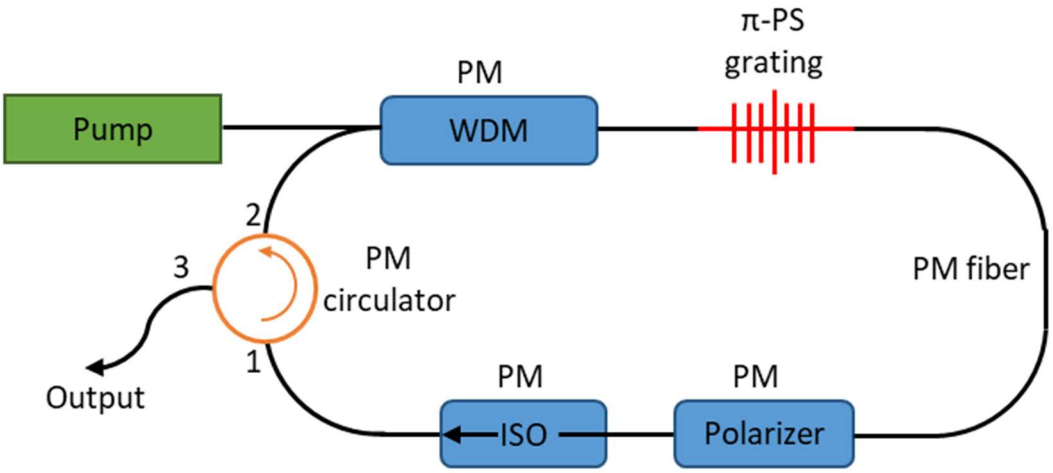

Figure 2-13 SPSF self-injection fully PM fibered design schematic. The polarizer selects the favored polarization to be reinjected, the WDM splits pump and signal wavelength, the ISO and circulator provides protection from back reflections, and the circulator enables SP output branch. Inspired from [64].

Yin et al. achieved single polarization single frequency operation (SPSF) in a 14 cm phase-shifted DFB erbium doped fiber laser using a self-injection design operating near 1.5 μm [64]. Their laser linewidth was 10 kHz with a reported wavelength stability under 10 pm. The laser maximum output power was 55 mW with 450 mW pump power. The self-injection design enables a fully PM fibered laser and robust SP operation it has also been demonstrated to reduce laser linewidth [64];1000 times smaller linewidth was achieved with a DFB laser using an external fiber-ring cavity [65]. However, the components required can be expensive outside of the typical Yb and Eb wavelengths, and the amount of component reduces the laser compactness. More importantly, the self-injection design inherently leads to a couple cavity behavior between the reinjected and DFB generated signals where the phase relation leads to wavelength instability. This circular cavity design leads to a cavity length at least in the tens of centimeters order of magnitude due to the many fiber components it requires. If we consider a small distance of 5 cm between each component (25 cm total); then the FSR generated by such cavity can be approximated using equation **(2.14)** to 416 MHz, or 4.21 pm at 1.74 μm signal wavelength. This small FSR distance can lead to mode hopping and thus unstable SPSF operation for the required Sr^{87} magic wavelength of <1 pm variation.

2.4.4 FBG writing using linearly polarized light

So far, the designs presented to achieve single polarization have been based on post-grating writing discrimination. The linearly polarized writing method relies on discrimination implemented during the writing process to achieve SP operation. Figure 2-14 presents the schematic of the SP process. The usage of a birefringent material (waveplate) on the writing light optical path can linearly polarized the writing light which is then aligned with the fiber core. In Figure 2-14, the refractive index modulation is more important for the plane parallel (y-axis) to the writing light than the perpendicular plane (x-axis) leading to loss discrimination. This method has been applied using both UV [38, 66] and femtosecond (fs) sources [67, 68]; with fs sources yielding the highest birefringence. However, the challenges for fs alignment are more important than UV alignment and poor phase control for length > 10 cm using this method poses serious grating quality issues especially when writing DFB structures.

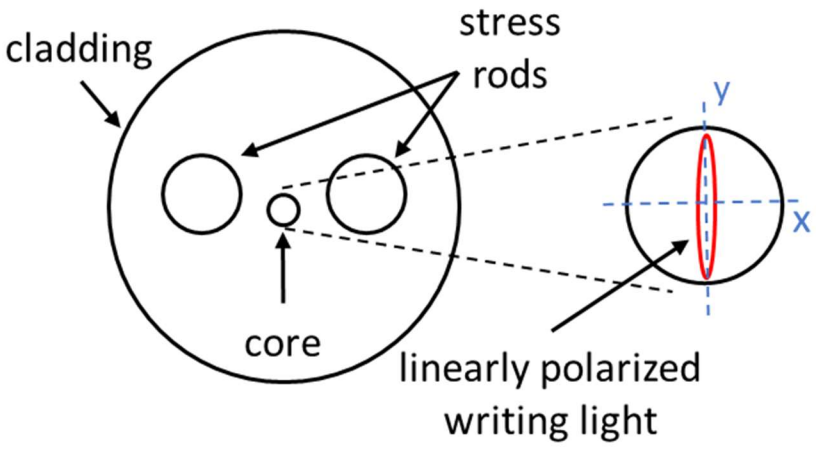

Figure 2-14 Single polarization design using a linearly polarized inscription beam. The RI modulation is higher for the y-axis, parallel to the beam, than the perpendicular x-axis resulting in a reflectivity difference between the modes.

The emergence of novel more robust fs phase control methods can potentially overcome this challenge [33], but core alignment constrains remain, and its complexity is increased in PM fiber due to the rods.

Soren Agger et al. utilized the FBG writing method using linearly UV polarized light to achieve SP operation in the phase-shift region for their phase-shifted DFB cavity, section 2.3.1 [38]. Using

a fs source, this method was demonstrated in a non-PM Er: Yb co-doped fiber in a rare-earth short-cavity (1.5 cm) configuration [68]. The inscription was directly written in the active fiber with a Ti:Sapph fs laser; the gratings were 8 mm long. Beam shaping led to polarization dependant loss discrimination. The SP operation was induced with birefringence measured led to a difference between orthogonal modes of 1.1 dB in reflectivity. The linearly polarized writing method shows great potential for SPSF operation directly embedded within the cavity, but is limited by the alignment requirements, the writing phase control and requires highly photosensitive fiber or a slow writing process to induce strong birefringence.

2.4.5 Fast and slow axis wavelength alignment

Inherent to their designs, DBR fiber lasers have at least one splice point in the cavity. This introduces loss in the system; however, this splice points also enables a polarization selectivity within the cavity. Polarization maintaining fiber splicing requires high precision alignment splicers. Typically, this imagery alignment is done with a 0° angle difference between each fiber polarization axis, i.e., a continuation of the fiber structure [42]. Introducing a 90° difference leads to only one wavelength respecting the Bragg resonance condition for both FBGs forming the cavity, thus a single polarization operation. As seen in Figure 2-15, the left-hand side (LHS) fiber comprised of the high reflector grating is in a 90° angle with the right-hand side (RHS) comprised of the output coupler and active fiber is in a 0° angle. Thus, by matching the LHS grating fast axis wavelength to the RHS grating slow axis wavelength during the inscription process, only the selected wavelength is resonant with both FBGs Bragg condition [69].

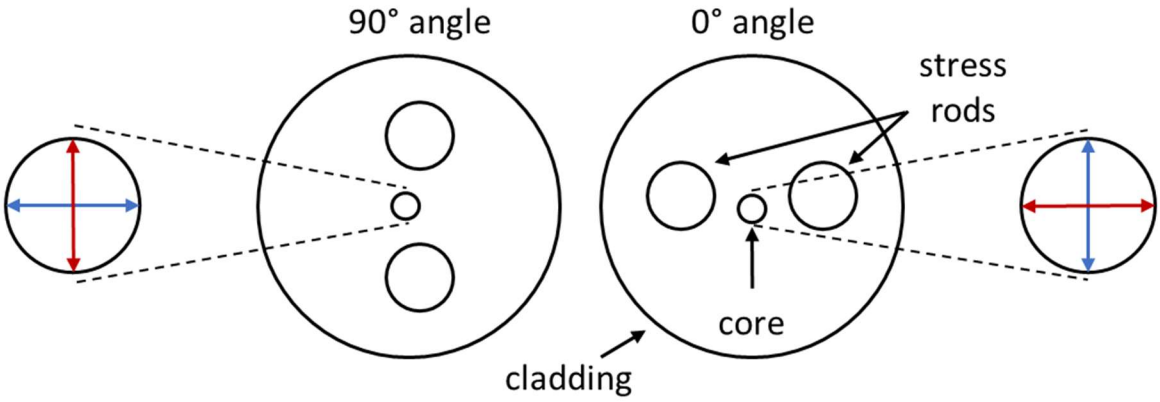

Figure 2-15 Single polarization scheme in DBR lasers with PM fiber. It requires alignment of the fast axis wavelength in the LHS with the slow axis wavelength in the RHS and a 90° splice. Red line slow axis, blue line fast axis.

This method is only applicable to short cavity laser designs and requires expensive specialized fiber splicers with end view mirrors for robust repeatability of the PM fiber rods angled alignment. Other applicable challenges when working with designs based of short-cavity Tm fiber near 1.7 μm are presented in section 2.4.6.

2.4.6 Non-PM reflector – DBR cavity

Similarly to the design presented in section 2.4.5, the non-polarization maintaining (PM) reflector method allows only 1 of the two polarization wavelengths in the short-cavity structure, presented in Figure 2-16. The use of a non-PM fiber reflector bypasses the stress rods high precision alignment. In a low birefringence fiber, the inscription yields a single resonant Bragg wavelength; selection of its wavelength with the slow or fast axis from the PM grating with a small bandwidth enables it to resonate in the cavity while the unmatched wavelength is dumped with the residual pump power using an angle cleaved bare fiber.

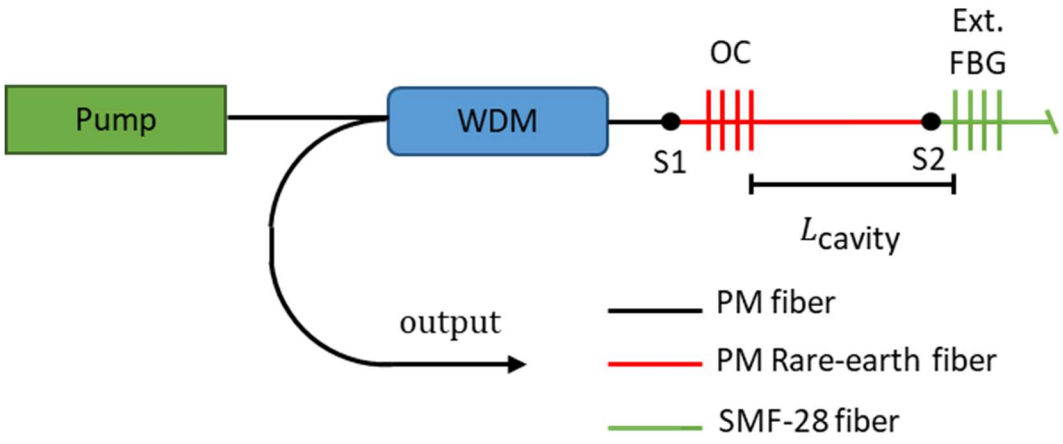

Figure 2-16 Single polarization short-cavity laser design. The external FBG (Ext. FBG) is written in low birefringent fiber, e.g., SMF-28 and wavelength matched to a polarization axis. Writing one of the gratings directly in the active fiber reduces cavity losses from splicing.

Most Tm lasers using a similar configuration operate near the 1.9 μm emission band [70-72]. Achieving the short-cavity design for a 1.7 μm TDF laser has a few notable challenges. Indeed, at this wavelength, TDF has a lower gain; the emission cross section is halved compared to 1.9 μm [73]. While the active fiber length can be increased for more gain, this SP design based on a short cavity is limited in length by its FSR for SF stability. Furthermore, the TDF 1.7 μm signal reabsorption is higher than its 1.9 μm counterpart, see Figure 2-7, increasing the population inversion requirement and thus the required pump power.

The first SPSF Tm laser using a non-PM reflector design was recently accomplished by [74] with an operating wavelength of 1.73 μm. The design used a non-PM HR grating, reflectivity > 99.9%, spliced to a 10.6 μm core diameter TDF, and an OC PM grating, reflectivity 80%. The laser cavity was inserted into a temperature-controlled copper tube. The initial cavity length of 2 cm led to multimode operation throughout the 10°C to 45°C temperature operation. The cavity was reduced to 1.8 cm and stable SPSF operation was achieved from 16°C to 22.5°C. The maximum output power was 12 mW for 600 mW of absorbed pump power, while a lower 1.5 mW output at 1730 nm was achieved with 350 mW of absorbed pump power at 1610 nm. The measured laser linewidth is 172 kHz at 20 dB limited by the self-heterodyne system resolution of 100 kHz.

Increasing the pump wavelength allows for a higher population inversion from the increased TDF absorption at longer wavelengths, see Figure 2-7, hence they were able to compensate for the low gain from a 1.8 cm cavity. However, their simulations showed that the minimal pump wavelength to obtain < 5 mW laser output power is ~ 1595 nm - when operating at a fixed pump power of 1 W with a 1.8 cm cavity. Additionally, under a pump wavelength of 1590 nm, the cavity does not lase - showcasing the high dependence on longer wavelength pumps. The low gain in Er for emissions >1600 nm and the increased excited state of absorption [75] complicates the generation of such sources versus shorter L-band wavelengths. Nonetheless, lasers operating over 1.6 μm, in a Er:Yb MOPA configuration [75] or with Ge:Bismuth (Ge:Bi) co-doped silica fibers [76] have seen an increased interest and their development opens the potential for more efficient Tm non-PM reflector-based DBR lasers.

2.4.7 Non-PM reflector – DFB cavity

Our proposed design is a phase-shifted DFB polarization maintaining (PM) fiber grating combined with an external FBG in non-PM fiber for polarization feedback discrimination, schematized in Figure 2-17. This external grating is wavelength matched with one of the polarizations; a small bandwidth ensures only one of the polarization modes is reflected. Hence, when sufficient signal from the matched polarization is returned, minimal FBG reflectivity, the cavity gain equilibrium is collapsed and the reinjected signal leads to single polarization (SP) operation. To the best of our knowledge the design presented in Figure 2-17 has not yet been demonstrated for SPSF operation. The active fiber length when using a DFB laser is much less restrictive than a DBR laser and major drawbacks occur closer to > 50 cm in length [48]. Development of longer wavelength pumps (>1600 nm) are expected to also increase our design performance for Tm fiber near 1700 nm emission. Nonetheless, the design enables better pump versatility, by allowing the more accessible lower L-band lasers to be used as pump sources. However, the introduction of the external cavity leads to a coupled cavity with phenomena that need investigation before claiming robust SPSF operation related to research objectives **(3), (4)** and **(5)**.

The mode field diameter (MFD) mismatch is known to be the major factor in splice losses [77]. MFD is related to the EM wave intensity profile propagating in the waveguide. The proposed design requires 3 different types of fiber displayed in Figure 2-17 making it prone to MFD

mismatches and losses at splice point 1 and 2, (S1) and (S2) respectively. S1 reduces the laser efficiency and increases threshold by decreasing the effective pump power available in the active fiber. While in-cavity losses from S2 increase lasing threshold, equation **(2.10)**. This is also applicable to the design in section 2.4.6.

The external FBG generates a FP cavity of L_{cavity} length, Figure 2-17, with resonant modes separated by an FSR inversely proportional to its length, equation **(2.14)**. The external FBG will be referred as FPFBG.

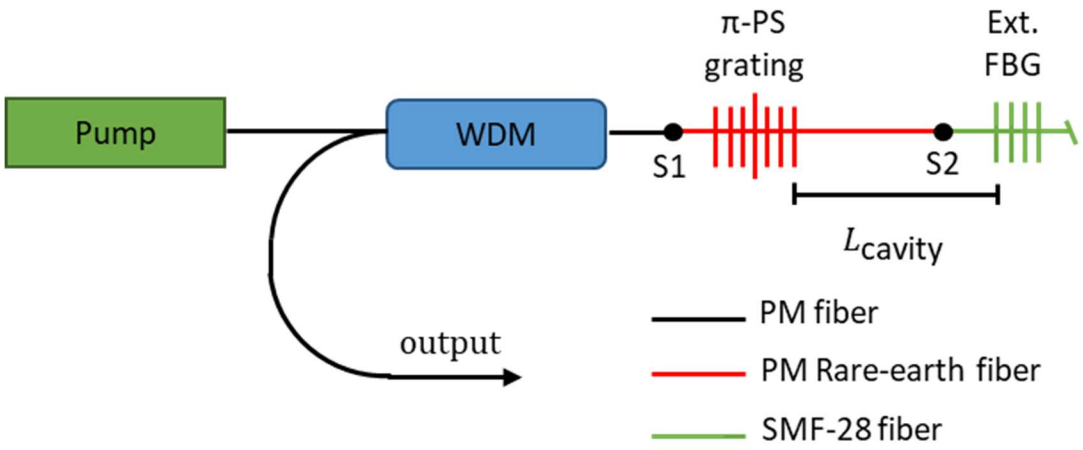

Figure 2-17 Proposed design using a PS-DFB laser cavity for single polarization operation. The external grating is written in low birefringent fiber, e.g., SMF-28 and wavelength matched to a polarization.

The FPFBG modes are modulated by the FBG spectral response as observed in [78, 79] and by extension the DFB grating. These modes within one polarization are detrimental to the SF operation. Like in short cavity lasers, they can lead to instability via mode hopping and multimode operation if they achieve threshold in the DFB cavity. Shortening the cavity length re-enforces SF operation - an increased free spectral range (FSR) reduces the number of modes in the active DFB grating.

External cavity FBGs can potentially reduce lasing threshold with an increase in reflectivity due to higher signal feedback. This effectively enhances the generation of stimulated emission and reduces amplified spontaneous emissions (ASE) [79]. This is however not mode selective, which

can lead to multimode operation by reducing the lasing threshold for other side modes if the reflectivity is too high.

The exte reflectivity leads to the next important consideration for SP operation. The reflectivity from the FPFBG depends on the phase relation between the DFB lasing mode and FPFBG modes. Resonance is a periodic behavior where its maximum occurs when in-phase, i.e., multiple integers of 2π, whilst no resonance occurs in anti-phase, i.e., multiple integers of π [21]. Hence, we can expect maximum signal feedback when in-phase and inversely in anti-phase no signal is returned in the cavity effectively creating losses for the aligned polarization and potentially collapsing its lasing. The reflectivity for other phases, partial resonance, has a periodic behavior in between the minima and maxima. This highlights the importance for preventing anti-phase behavior to achieve robust SP operation.

Equation **(2.13)** dictates the phase relation to multiple variables that need to be considered for phase control. It shows the length traveled by light in a medium (O.P.) affects its resulting phase. This adds a requirement of controlled FPFBG length for reproducibility. To ensure constant FPFBG length, the gratings need to be written following the 3 fiber types splicing. The precise stages used for FBG writing can then control a specific minimal length, for multimode operation discrimination, with the required phase from the optical path. This re-enforces single polarization (SP) operation at room temperature and without strain, however, the refractive index and length have a temperature dependence from their respective thermal coefficient [24] which compromises SP operation; this enables FBG usage for strain and temperature sensing. A combination of phenomena such as: quantum defect, temperature non-uniformity in the phase shift region, laser temperature control and frequency tuning are expected to modify n and L during its operation. Discussed in section 2.3.4, DFB lasers are inherently prone to quantum defect which leads to phase detuning and non-uniformity heating. The quantum defect can also lead to chirp gratings and thus a lower cavity efficiency. Generally, the temperature control setup and/or method for fiber lasers should maximize the temperature uniformity, but this is far from trivial with DFB lasers due to the PS region.

Reducing the negative impact from temperature on the laser performances becomes now highly relevant. The phase dependence to temperature is found by the temperature derivative of equation

(2.13). It has been shown that the dominant thermal effect is from the RI change [24], we then arrive to equation **(2.15)**:

$$\frac{\Delta\phi}{\Delta T} = \frac{2\pi}{\lambda}\left[\frac{\partial n_g}{\partial T}\, L\right] \qquad \textbf{(2.15)}$$

Where $\Delta\phi$ is the phase change, ΔT is the temperature change, λ is the wavelength, L is the length and $\frac{\partial n_g}{\partial T}$ the thermo-optic coefficient with units (RI/°C). The resulting equation is a linear relation between temperature and phase where the coefficient $\frac{\partial n_g}{\partial T}$ varies for each waveguide due to the RI dependence, adding a phase control challenge. Hence, equation **(2.15)** further re-enforces the need for a small FPFBG length to reduce phase perturbations from temperature.

2.5 Laser for Sr^{87} Based Optical Clocks

In this section we present a brief overview of other 813 nm sources and their applicability to Sr^{87} magic wavelength (MWL) generation.

2.5.1 Ti:Sapphire lasers

Among the first source used for strontium magic wavelength generation were Ti:Sapph lasers [16, 80] [81]. Their availability, maximum gain, and laser efficiency near 800 combined with SPSF operation made them a good fit for a research setting. However, such systems are based on free space optic leading to poor reliability, and more importantly major challenges for a compact design and space friendly device. Other crystal-based lasers have been demonstrated for Sr^{87} atomic clock but suffer the same free space optic drawback [22].

2.5.2 Laser diodes

Semiconductor lasers designs enable SPSF operation while offering a wide range of wavelength selection including the 813 nm MWL, e.g., InGaAs, GAsP and AlGaAs. Fiber lasers advantages over their semiconductor counterpart, section 2.3.1, partially explain the limitations of LD in MWL generation. The biggest challenge for laser diodes is their small output power limited to mW order of magnitude and the lack of simple signal amplification designs at 813 nm.

2.5.3 Ge:Bi co-doped fiber

Ge:Bi co-doped fiber enables the generation of fiber lasers sources within the 1.6 μm – 1.8 μm region. This emission band could rely on frequency doubling to achieve 813 nm. Designs using this fiber have reached watts output powers near 1.7 μm. However, current applications are limited to lengthy fiber sources and amplifiers due to the high background losses making the fiber unsuitable for SF designs. [76]

2.5.4 TDF $^3H_4$ - $^3H_6$ transition

From an energy level perspective, silica TDF can have radiative emission in the 800 nm region. This emission occurs between the $^3H_4$ - $^3H_6$ energy levels, Figure 2-5. In practice, the $^3H_4$ energy level cannot be attained using 1 photon pumping schemes and is thus associated to its absorption band. The following methods are based on upconversion to achieve population inversion in TDF to the $^3H_4$ level for stimulated emission to the $^3H_6$ ground state.

2.5.4.1 Fluoride Tm doped fiber

The high-phonon energy in silica-based fiber leads to poor upconversion performances. With a reduced phonon energy, fibers made from ZBLAN glass enable a higher upconversion efficiency by increasing the excited state lifetime. The 810 nm high power emission was demonstrated in [82] with 1 W of output power, while more recently a 813 nm high power SPSF for optical lattice applications was demonstrated in [83] with 2 W output power. Beside other issues encountered by the development of the latter laser such as photodarkening [84]; ZBLAN fibers are expensive to manufacture, hard to splice and have a low durability, strength compared to silica based fibers.

2.5.4.2 Tm co-doped fiber

The low efficiency to operate a silica based TDF at 800 nm is not limited to the high phonon silica energy. Indeed, as presented in section 2.2, a 1060 nm pump laser in silica TDF offers the required excited state absorption for upconversion. This upconversion is not limited to the $^3H_4$ level as it is capable of exciting the ion to the upper $^1G_4$ level, further reducing the efficiency in silica based TDF. Co-doping the fiber with Yb was demonstrated with a 980 nm pump, which reduces the unwanted excited state absorption to the $^1G_4$ state. Like Ge:Bi co-doped fibers, the applications are

limited to long cavity lasers or amplifiers. While other co-dopants have also been studied such as Tm:Alumina [85] none possesses sufficient gain efficiency for the fiber length required in SF fiber designs.

CHAPTER 3 EXPERIMENTAL METHODOLOGY

The following chapter presents the methodology for the experimental manipulations performed during this research with their respective measurements, setup, and equipment. The chapter is divided into sections tied to the research objectives presented in section 1.5.2. The proposed design schematic for single polarization single frequency (SPSF)operation presented in Figure 2-17 is comprised of 3 fiber types: 1 non-PM fiber (green) for discriminating feedback, 1 PM Tm gain media fiber (red) and PM fiber (black) for controlled polarization propagation. For cost reduction and increased accessibility purposes the work in this thesis utilizes SMF-28 fiber components instead of PM fiber. This modification does not alter laser operation; the single polarization single SPSF laser challenges arise from the polarization maintaining thulium doped fiber (TDF) hence the methodology and results remain valid.

3.1 Laser Conception

The experimental methodology leading to objective **(1),** an operational TDF phase-shifted DFB laser is presented. This includes determining pump absorption, create a splice recipe to minimize splice losses, characterize TDF gain, characterize TDF absorption at pump and signal wavelength, and writing an operational PS DFB laser cavity.

3.1.1 Pump absorption and splice loss

Fiber splicing is inevitable when working with fiber systems. Common fiber splices recipes such as SMF-28 to SMF-28 are often included by default in splicing machines. The usage of multiple type of fibers requires a custom-made recipe for loss from mode field diameter (MFD) mismatch, and thus the need for splice loss minimization. Although critical in any fiber related research, the steps and science for creating a splice recipe go beyond the scope of this thesis. For more

information on the science of splicing procedures we refer the reader to [86]. The specifications of the PM TDF selected in the present work are presented in Table 3.1

Table 3.1 PM Thulium Fiber Specifications

Parameter	Specification	Units
Absorption @793 nm	>120	dB/m
Absorption @1180 nm	>30	dB/m
Numerical Aperture	0.25 ± 0.02	
Core Diameter	4.5 ±0.5	µm
Cladding Diameter	125 ±2	µm
Coating Diameter	245 ±15	µm
Proof test level	100	kpsi
Birefringence	$>2x10^{-4}$	

The absorption coefficient data is given for the 790 nm and 1200 nm bands, no data for the L-band absorption is available. The MFDs for TDF and SMF can be calculated at 1742 nm with Marcuse's equation [87] applicable to single-mode fibers. Resulting in TDF MFD = 5.6 µm and SMF-28 MFD = 10 µm, the MFD mismatch showcases the splice recipe optimization importance.

The splices were performed with a Fujikura FSM-100P splicer. The setup for splice loss and pump absorption measurements is presented in Figure 3-1. The source is a JDSU low power tunable laser model SWS15101 and the power meter is a Thorlabs S144C low signal integration sphere power meter with a spectral range of [0.8 µm - 1.7 µm]. The insertion loss method [86] was used to measure splice loss at pump wavelength, 1575 nm. Once modified the new recipe is tested with the same method. The angle cleave prevents lost of power from back-reflection and unwanted signal feedback in the laser. An integrating sphere power meter ensures the detected light amount is constant. Only one splice recipe optimization is required, i.e., between SMF-28 and TDF.

The same source is selected for fiber absorption. To prevent absorption saturation and amplified spontaneous emission (ASE) generation leading to a false absorption coefficient, the measurements are performed with a low pump power laser at pump wavelength. A 50 cm length TDF is spliced to SMF-28 at S1 followed by an angle cleave, again to mitigate back reflection. The cut-back method [86] is used with the Tm bare fiber. The laser operates at 1575 nm with a 3.59 dBm power at P1. The fiber is left unstressed to reduce inadvertent mechanical losses.

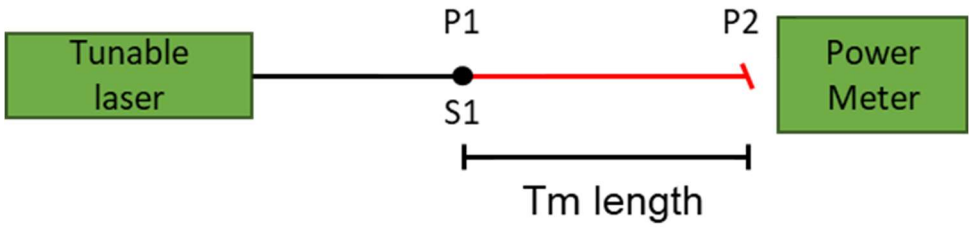

Figure 3-1 Tm fiber absorption and splice loss experimental setup. The tunable laser is operated at the pump wavelength of 1575 nm and at low power to prevent absorption saturation.

3.1.2 TDF gain and absorption

The gain fiber characterization setup is presented in Figure 3-2. The pump is an Er CW laser operating at 1575 nm from MPBC with an output power ranging from 90 mW to 1.3 W; output power characterized see Figure 3-3 .

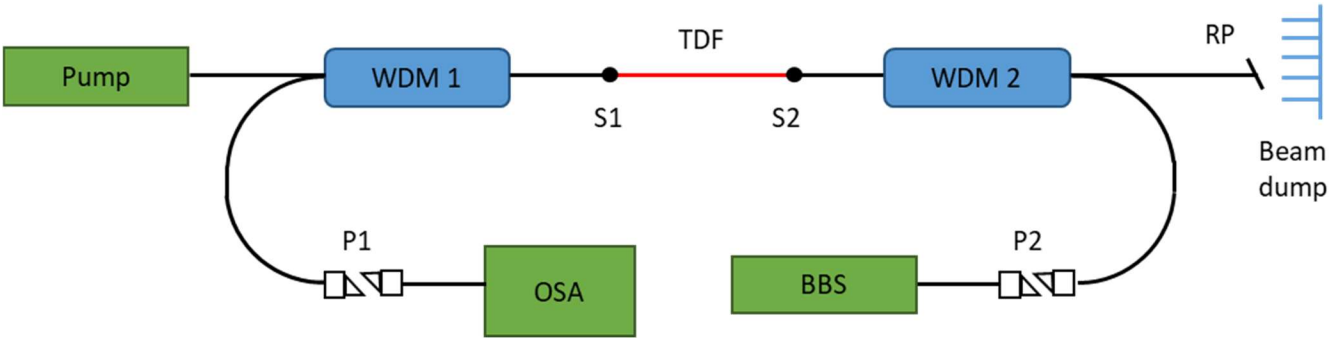

Figure 3-2 TDF characterization setup.

The wavelength division multiplexers (WDMs) are made of SMF-28 fiber and separate the pump and signal wavelength. WDM1 pump port delivers the pump power to the common port. Its signal port (P1) is connected to an Optical Spectrum Analyzer (OSA) model Yokogawa AQ6375B with a spectral range of [1.2 µm – 2.4 µm] and maximal resolution of 0.05 nm. P1 and the OSA are connected using FC/APC connectors and a mating sleeve. WDM2 pump branch serves as residual pump (RP) dumping with an angle cleave to negate pump back reflection. A custom-made broadband source (BBS) from MPBC is connected to the signal port of WDM2 (P2) with FC/PC connectors and a mating sleeve. The BBS emission bandwidth is from 1.6 µm to 2 µm and the TDF length is 12.3 cm

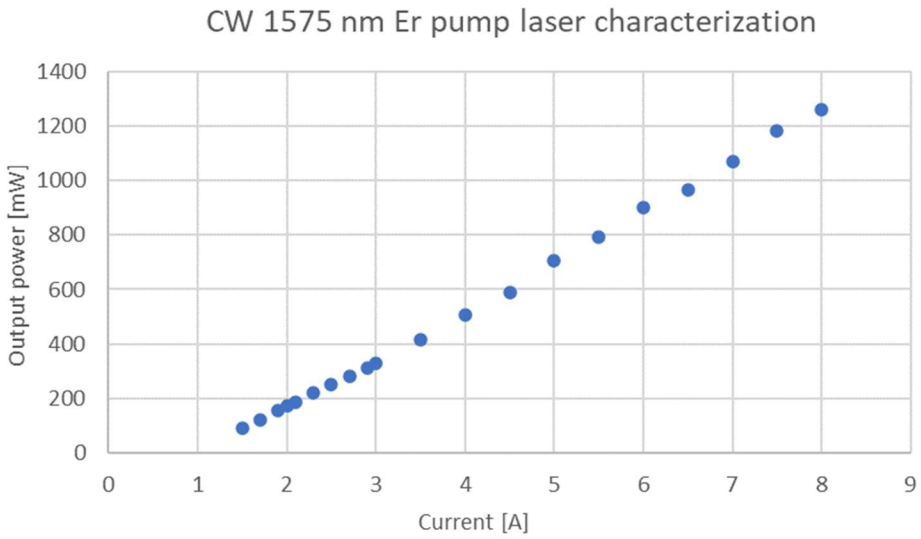

Figure 3-3 Pump laser output power characterization

The TDF gain spectrum can be experimentally obtained using the setup presented in Figure 3-2, where the broadband source signal is amplified by a TDF in a counter-pump configuration. TDF or SMF-28 is inserted between splice point 1 and 2 (S1, S2); SMF-28 is used to characterize reference value while preserving the setup insertion losses from the WDMs.

Thulium doped fiber net gain spectrum G [dB/cm] is obtained using equation **(3.1)**:

$$G = \frac{1}{L}(P_{out} - P_{in} - P_{ASE}) \quad \textbf{(3.1)}$$

Where L is the gain fiber length, P_{out} is the BBS amplified signal by the pumped TDF measured at P1. This measurement also includes the absorption losses from the TDF. P_{in} is the BBS reference signal, measured at P1 with SMF instead of TDF to preserve insertion losses. The BBS signal amplified has an added amplified spontaneous emission (ASE) component referred as P_{ASE} due to the pumped TDF. This component is subtracted from P_{out}. The ASE spectrum is obtained at P1 by only turning on the pump laser with the 12.3 cm of TDF.

The fiber absorption loss spectrum is obtained by subtracting P_{in} to the BBS signal unpumped measured at P1and divided by the 12.3 cm length of TDF used in the setup. The resulting spectrum is our TDF absorption from the $^3F_4 - {}^3H_6$ emission band.

3.1.3 Phase-shifted DFB grating

The phase-shifted (PS) DFB grating was inscribed using a 213 nm UV source with a Talbot interferometer and a phase mask presented in section 2.1.4.1- an in-depth setup and methodology can be found in [27]. The gratings inscription was done by my colleague Frederic Monet. The DFB grating specifications are listed in Table 3.2. The Bragg wavelengths are at room temperature, unstrained and at pump threshold with thermal compound measured with a 0.05 nm resolution OSA. The DFB was apodized at 40% of its length using a cosine function.

Table 3.2 Phase-shifted DFB Grating Specifications

Parameter	Specification	Units
λ_B fast axis	1741.9	nm
λ_B slow axis	1742.4	nm
κ	64	m^{-1}
L	100	mm
PS	π	rad
PS offset	5	mm

The resulting grating strength is $\kappa L \approx 6.4$. The PS offset is 5 mm off the grating center. The DFB grating is annealed for 16 hours at 190°F to increase its RI modulation robustness to thermal effects [24]. Then the grating is spliced at S1 and S2, Figure 3-2, using the developed recipe. OSA spectra are taken at the DFB grating HR output (P2) and OC output (P1) to confirm lasing. The laser rests on an aluminium metallic plate with thermal paste to reduce unwanted heating effects. However, the thermal compounds viscosity can lead to non-uniform uncontrolled cavity strains with effects comparable to non-uniform heating. What is more, the thermal compound can increase the difficulty in measurement reproducibility and increase the chance of fiber breaking during the multiple required manipulations. Glycerol as been previously used in [56], instead of a paste based thermal compound, however glycerol is suitable for space applications. This highlights the need for a lower viscosity thermal compound paste for an uniform strain.

3.2 Single Polarization Single Frequency (SPSF) Operation

The experimental methodology leading to an SPSF laser is presented in this section. They encompass the methodology leading to the realisation of objectives **(2), (3)** , **(4)** and **(5)**. This section methodology can be separated into 3 main parts: Simulation of the SPSF design, SP laser operation setup, and SPSF laser operation setup with a reduced external cavity length for robust SPSF operation under laser tuning and temperature control.

3.2.1 SPSF simulations

The design spectral response was simulated using an existing in-house program based on the transfer matrix method described in [25] developed by my colleague Anthony Roberge. The simulation highlights critical parameters to consider for the experimental setup: cavity length, phase shift value, and wavelength offset. The simulation is based on 3 main transfer matrixes. The first one is comprised of two uniform gratings with a phase-shift simulating the PS grating. The second one is comprised of a phase shift matrix simulating the external cavity. The last main transfer matrix is comprised of a uniform grating simulating the external FBG. The simulations are limited to spectral response results – a complete simulation would include DFB gain mechanisms [27, 35] and dynamic mode competition [88, 89] requiring much more complex simulations beyond the scope of this thesis.

3.2.2 Characterization equipment

3.2.2.1 Pump laser

The pump is the 1575 nm Er source with a maximum pump power of 1.3 W with a bare fiber output from MPBC. We have discussed how longer wavelengths >1600 nm are more desirable for Tm pumping, however this increases the pump laser conception difficulty and potentially cost.

3.2.2.2 Optical Spectrum Analyzer

The OSA model utilized is an ANDO AQ6317B with a spectral range of [0.6 μm – 1.75 μm] and maximal resolution of 0.01 nm. OSAs rely on spectral density and generally diffraction gratings for their measurement [90], although others based on interferometers also exist. They allow a broad

spectral range with input powers up to ~20 dBm. However, their resolution limits their usage for SF laser measurements.

3.2.2.3 Electrical Spectrum Analyzer

The Electrical Spectrum Analyzer (ESA) model is a Keysight PXA-N9030A with a maximum frequency of 50 GHz. The ESA enables frequency beat measurements. Hence a great tool to study SF operation. The ESA maximum frequency for $\lambda = 1742$ nm limits its reading to a maximum $\Delta\lambda = 0.5$ nm, over that range the OSA is fully capable of providing the wavelength resolution required to observe any multimode operation. However, the ESA observes frequency beat, one could have SF operation, thus no frequency beat but have unstable SF operation such as from jitter or mode hopping.

3.2.2.4 Fabry-Perot interferometer

The Fabry-Perot interferometer (FPI) setup is comprised of a dual channel oscilloscope, a sawtooth voltage generation model SA201 and a FP cavity with an integrated PD. The FP model from Thorlabs is SA200-12B with a spectral range of [1.3 μm – 2 μm], an FSR of 1.5 GHz and a maximal resolution of 5.8 MHz. The FPI is an additional SF measurement tool relying on interferometry for its measurements. A piezoelectric material allows a maximal cavity sweep equal to its FSR, while the FWHM cavity modes dictate its resolution [90]. The FPI allows the measurement of single mode operation, mode hopping and stability.

3.2.2.5 Power meter

The power meter from OPHIR is a 3A model; a thermopile sensor with a spectral range of [0.19 μm – 20 μm] and a power range of [10 μW – 3 W]. There exists a multitude of photodetector (PD) equipment, but two of the most common are semiconductors or thermopile based. The semiconductor PD are limited by InGaAs responsivity which greatly decreases after ~1.6 μm, this range can be extended but is not as accessible and affordable. Hence, the selected power meter is a thermopile-based PD, less sensitive to wavelength by design.

3.2.3 External FBGs

The proposed SPSF laser design requires the usage of an FPFBG, i.e., an external uniform grating at a distance L of the PS grating. The FPFBGs were written by my colleague Frederic Monet in SMF-28 fiber using the same setup from section 3.1.3. They are then annealed for 16 hours at 190 °F to increase their RI modulation robustness to thermal effect. The FPFBGs used in the SP and SPSF manipulations are presented in Table 3.3 with their respective specifications and related experiment. None of the FPFBGs were apodized, and their length is 1 cm.

Table 3.3 FPFBGs Specifications

FPFBG	λ_B (nm)	R (%)	L_{Cavity} (cm)	FSR (GHz)	Experiment
FPFBG1	1742.16	10	190	0.054	SP
FPFBG2	1742.16	52	190	0.054	SP
FPFBG3	1742.2	48	4.4	1.17	SPSF
FPFBG4	1742.26	48	3.2	3.21	SPSF

3.2.4 Thermoelectric coolers

Two TECs jig were used throughout the SPSF operation methodology, both are schematized in Figure 3-4. Each TEC thermistor position for temperature feedback is presented (red cross). TEC a) is comprised of two metallic plates with fiber grooves and two independent TECs with a total length of 10 cm. TEC a) thermistors for temperature feedback are inserted inside the metallic plate.

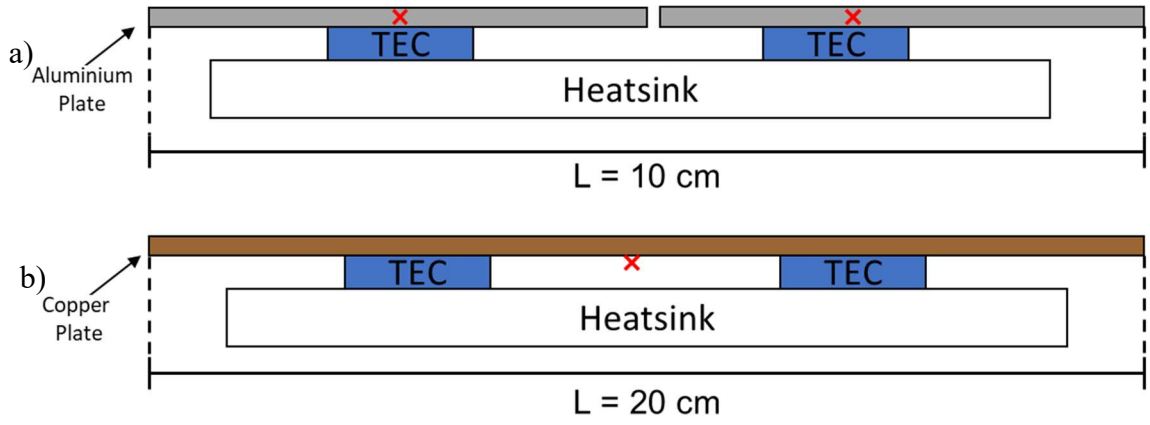

Figure 3-4 TEC setup used for a) SP operation methodology b) SPSF operation methodology, thermistor positions (red cross).

TEC b) is comprised of a single 20 cm metallic plate without fiber grooves and two dependent TECs. Thermal paste is applied on both upper and lower surface of the TECs for an increase in heat transfer. A thermistor is placed under the center of the metallic plate within the thermal paste for temperature feedback. The Peltier elements for TEC b) have a larger dimension than TEC a) for increased temperature uniformity over its longer length.

3.2.5 Single polarization (SP)

The fibered setup to achieve SP operation is shown in Figure 3-5. An FPFBG is spliced to the right-hand side (RHS) of the PS grating creating a cavity with a length L_{cavity}. At room temperature FPFBGs are not wavelength matched with one of the DFB grating polarization. Hence, the FPFBG rests in a metallic groove with integrated TECs for wavelength temperature tuning, in Figure 3-4 a). FPFBG 1 and 2 were tested on this setup. The discriminating reflection favorizes gain for the reinjected polarization leading to SP operation, section 2.4.7. The WDM splits the pump and signal wavelength. The selected signal output is the backward signal (relative to the injected pump power) for an increased signal-pump extinction ratio. The forward output is spliced to the FPFBG and dumped with the residual pump at Port 3 (P3) on a beam dump using an FC/APC connector. An isolator (ISO) in the backward signal output prevents unwanted Fresnel reflection from the FC/PC connectors at Port 1 (P1) and Port 2 (P2).

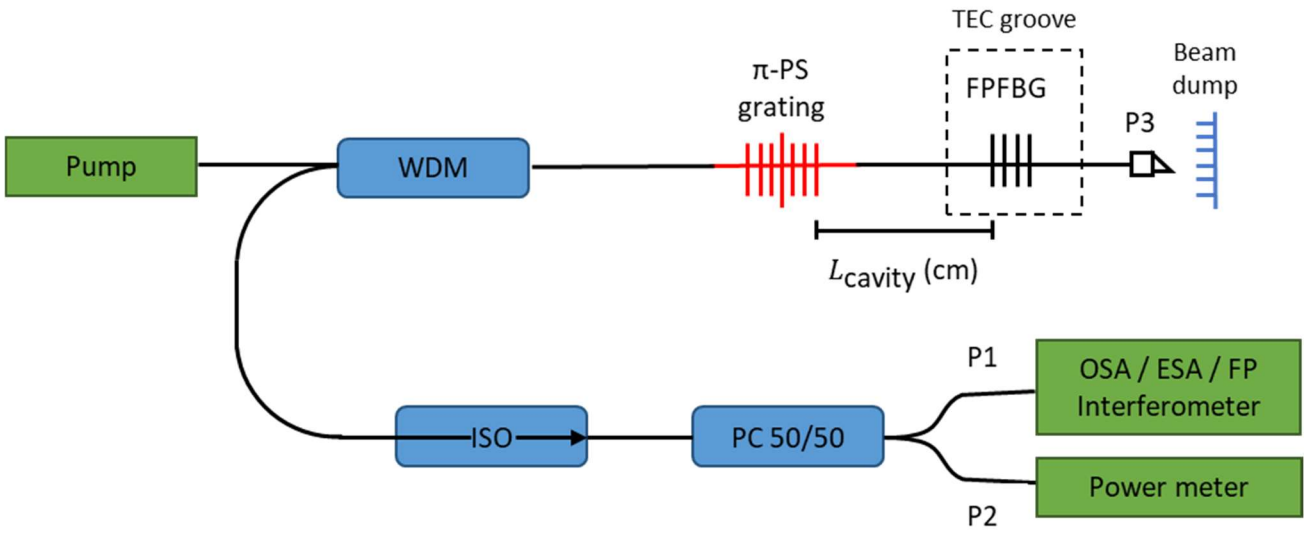

Figure 3-5 Laser single polarization operation setup

The backward signal is split by a – 3dB coupler (PC) where P1 and P2 are interchangeably connected to the characterization equipment. The PS grating rests on a metallic plate without thermal compound. Reflection spectra of the un-pumped laser can be obtained at P3 with a -3 dB coupler and supercontinuum source.

3.2.6 Single polarization single frequency (SPSF)

The fibered setup to achieve SPSF operation is shown in Figure 3-6. The setup utilizes the same setup as the SP operation with new elements. The FPFBGs used in this setup, i.e., FPFBG3 and 4 are wavelength matched. Hence, the laser rests on a single metallic plate with two TECs driven by the same controller, Figure 3-4 b). Fiber holders mounted on micrometric translation stages on each end of the laser cavity enable frequency tuning by controlled strain.

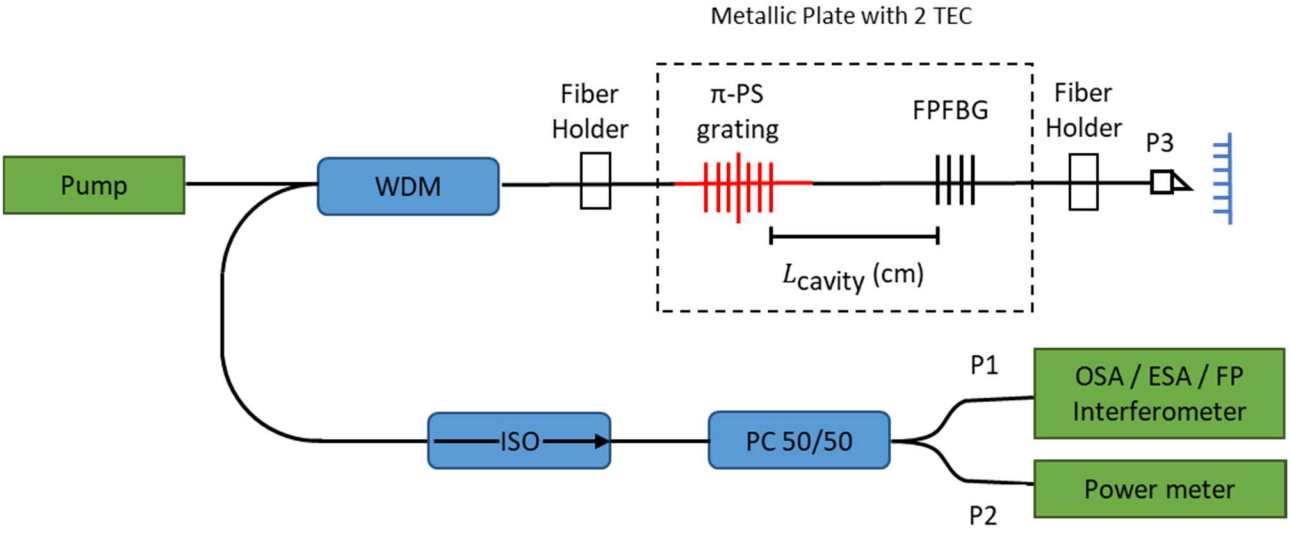

Figure 3-6 Laser single polarization single frequency setup

CHAPTER 4 RESULTS

4.1 Building the Laser Cavity

4.1.1 Pump absorption and splice loss

The data collected in section 3.1.1 is presented in Figure 4-1. With the data in its logarithmic form, the splice loss can be separated from the absorption loss. The splice loss measured is <0.1 dB or over 98% signal transmission and the absorption coefficient α measured is α = 0.6 dB/cm at 1575 nm. Using Table 3.1. we thus have α(0.8 μm) = 1.2 dB/cm, α(1.2 μm) = 0.3 dB/cm and α(1.58 μm) = 0.6 dB/cm. This is in accordance with thulium doped fiber absorption behavior from Figure 2-6. The highest absorption is in the 800 nm band while the 1200 nm band and 1650 nm band have a similar absorption, with the 1200 nm band absorption dropping rapidly for close to peak wavelengths.

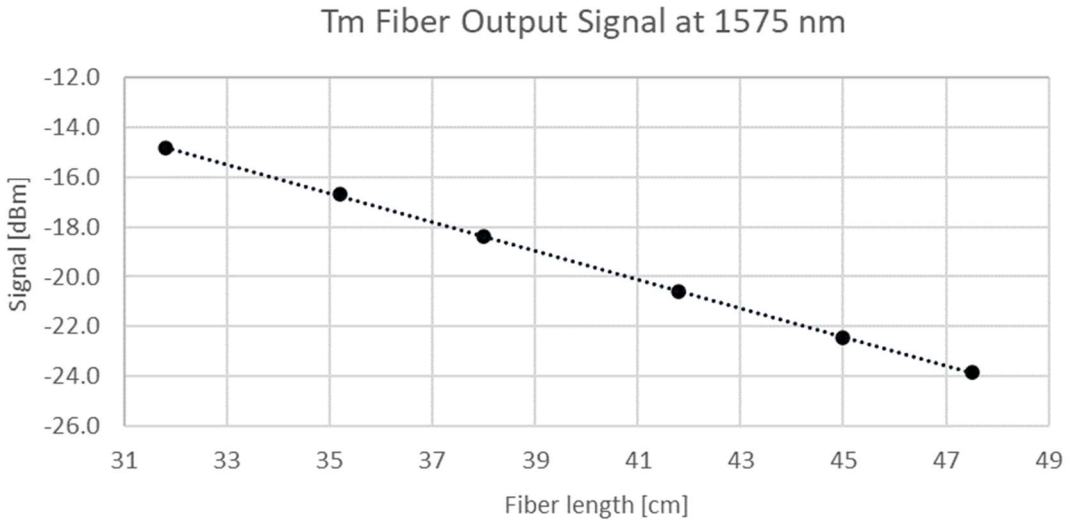

Figure 4-1 TDF output small signal for multiple fiber lengths at pump wavelength (1575 nm).

The splice recipe yields a transmission of 98% or 0.1dB loss, much higher than the 15% transmission yield using SMF-28 common recipe. We believe the transmission can be further improved with a non-PM fiber with a closer MFD to the Tm fiber than SMF-28, recalling the calculated MFD for TDF and SMF-28 of 5.6 μm and 10 μm respectively. Low splice losses measurement requires an improved loss measurement setup. This could be achieved by a proper

implementation of the loss estimation program available in the Fujikura FSM-100P splicer. The splice recipe was strained tested at 140 kpsi (0.14 Gpa) with 10 splices each tested 10 times to ensure robust mechanical integrity.

4.1.2 TDF gain and absorption characterization

The purpose of thulium doped fiber (TDF) gain and absorption characterization is to ensure positive net gain near 1740 nm especially due to the expected high signal reabsorption for shorter Tm doped fiber emission wavelengths as seen in the literature review. The high signal reabsorption can also be shifted with co-dopants, thus characterizing the absorption is also important. Figure 4-2 presents the measured TDF absorption spectrum for its emission band. The absorption at the signal wavelength of 1742 nm is ≈ 0.4 dB/cm. This is in agreement with [38] where the measured absorption is 0.4 dB/cm at 1735 nm. The signal absorption peaks near 1640 nm and decreases with increasing wavelengths. This is also consistent with the TDF literature absorption spectrum (see Figure 2-7).

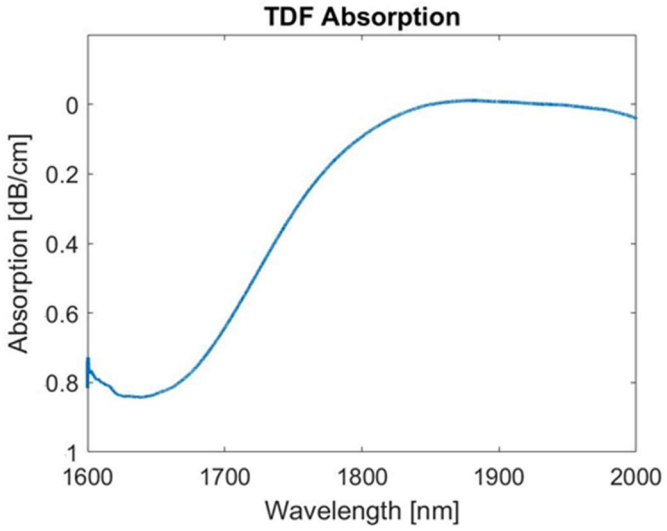

Figure 4-2 TDF emission band absorption spectrum.

Figure 4-3 a) presents the ASE at maximal pump power (1.3 W) for 12.3 cm of TDF. This highlights the emission peaking near 1800 nm and decreasing all for other wavelengths also consistent with the literature [35]. Hence, both these results confirm the challenges related for TDF generation near 1700 nm. Figure 4-3 b) shows the net gain spectrum of the TDF obtained via equation **(3.1)**. The net gain near 1740 nm is positive with a value of 0.5 dB/cm thus enabling lasing. As a comparison Tm:Bi doped fiber for 813 nm direct generation has a gain 2 orders of magnitude smaller, greatly limiting its length and therefore, laser applications usage [76].

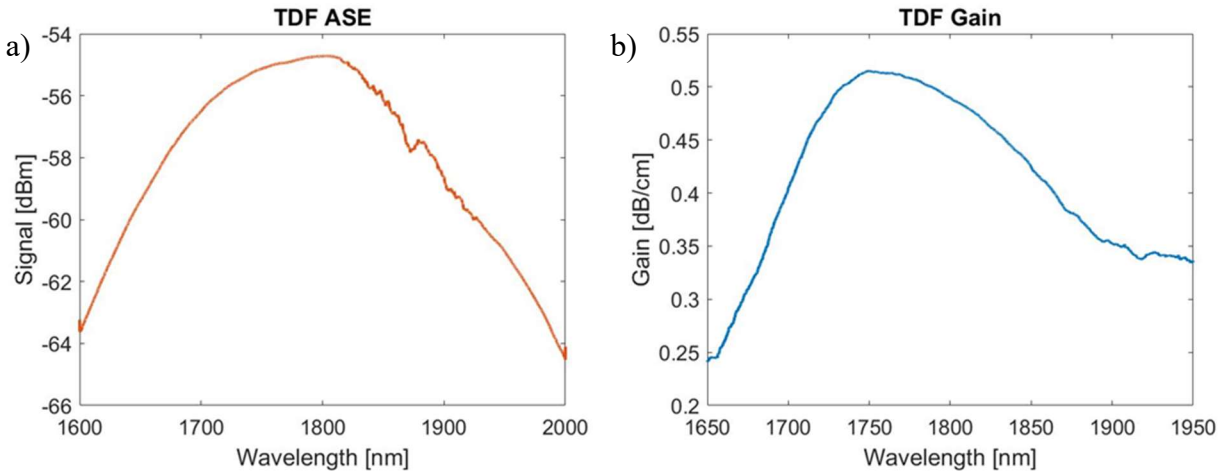

Figure 4-3 TDF a) ASE spectrum with a 1575 nm pump and b) small signal net gain.

4.2 Phase-Shifted DFB Grating

Once the grating was inscribed in the PM TDF and inserted in the initial test bench, (see Figure 3-2) it was pumped with the 1575 nm laser for multiple pump powers. The resulting spectra are presented in Figure 4-4 for a) high reflection (HR) output and b) output coupler (OC) output.

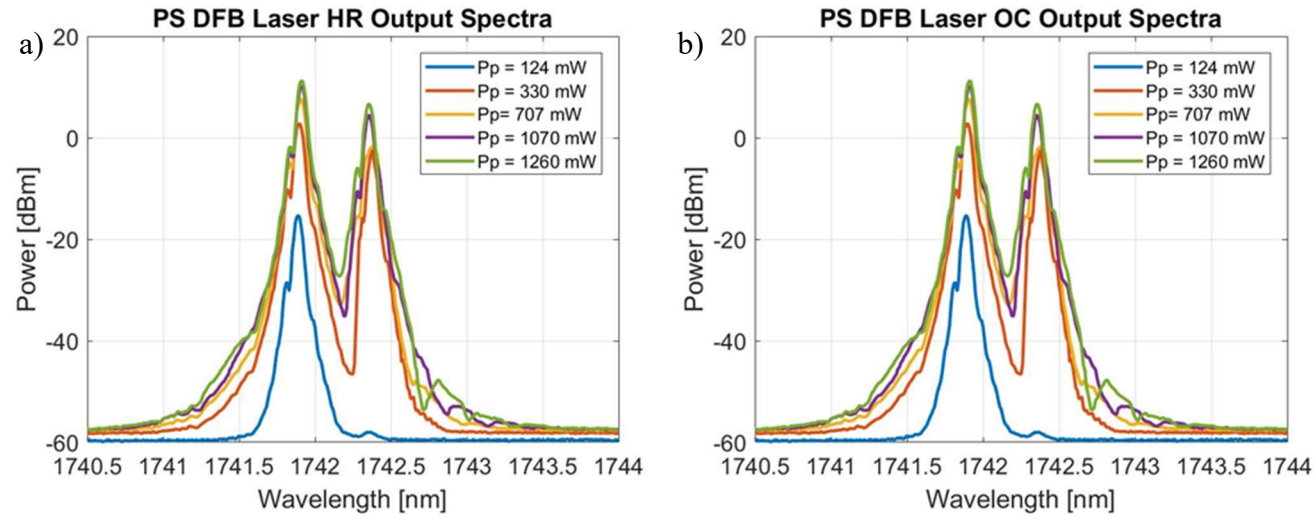

Figure 4-4 Laser spectra for its a) HR output and b) OC output, at multiple pump powers.

The laser has a threshold pump power of 124 mW. Interestingly, we observe how only the fast axis lases at pump threshold whereas multimode operation from the polarization axes is observed at higher pump powers. This is attributed to one or more polarization dependent elements presented in section 2.4, especially stress induced [61, 62]. In other instances, when manipulating the fiber, the slow axis was observed to lase at low pump power and the fast axis did not lase. This highlights the sensitivity of the DFB and the necessity for a setup with robust repeatability – hard to achieve with the thermal compound paste. We also observe similar output power from the OC and HR outputs. This can be explained by both gratings having a high strength, which reduces small phase-shift (PS) offset effects. Nonetheless both output powers have important differences when looking at their broad output spectrum shown at maximal pump power in Figure 4-5.

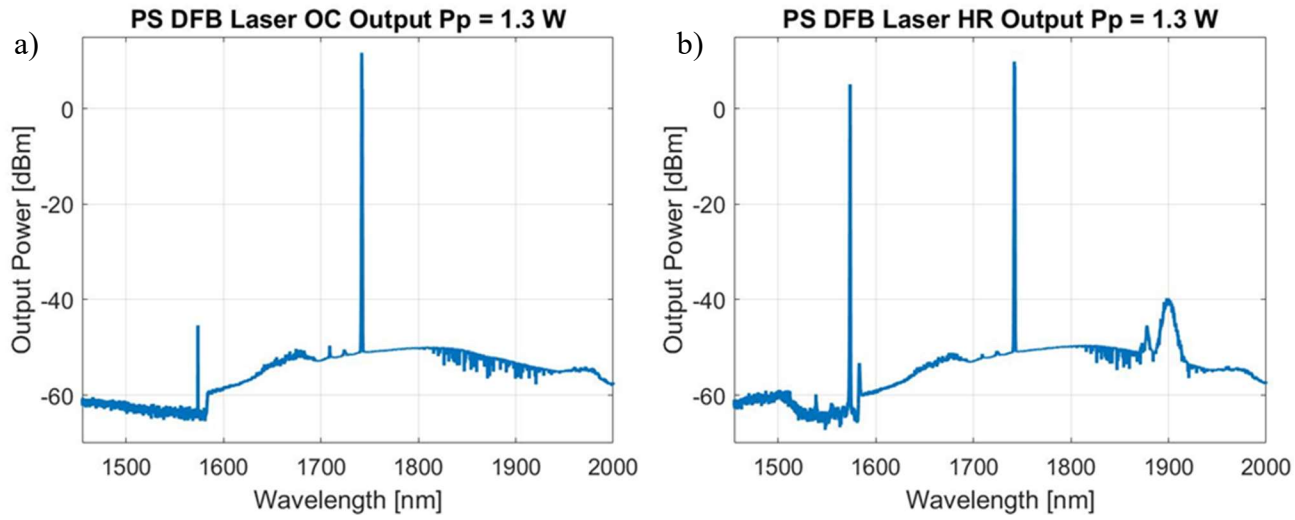

Figure 4-5 Laser broad spectra for its a) OC output and b) HR output, at maximal pump power.

Along with the lasing peak around 1740 nm, we observe in both outputs TDF ASE from 1600 nm to 2000 nm and the pump at 1575 nm. The pump signal extinction ratio is 55 dB for the OC output while it's only 5 dB at the HR output. Recalling from section 3.1.3, the HR output signal is co-propagating (forward output) with the pump signal whilst the OC output is counter-propagating with the pump signal (backward output) leading to the high extinction ratios difference between ports. We also observe unwanted low signal near 1900 nm from the forward output with a high extinction ratio with the main signal; it's not observed in the backward output. The short fiber length eliminates four wave mixing between the 1740 nm laser and 1575 nm pump as an explanation of the observed signal at 1900 nm. This signal could be due to the second order of

diffraction from the 950 nm laser residual pumping the 1575 nm erbium doped fiber laser. Considering our observations, the backward output is the selected port for the laser characterization due to its high signal to pump ratio and absence of unwanted lasing signals.

Lastly in this setup and configuration the laser was put under stress with pressure applied perpendicularly to the active fiber to attempt SP operation. Figure 4-6 shows the resulting spectra, where the fast axis mode has collapsed confirming attainable SP operation under applied stress. Achieving the same SP operation mode however was not reliably done highlighting the manufacturing limitations.

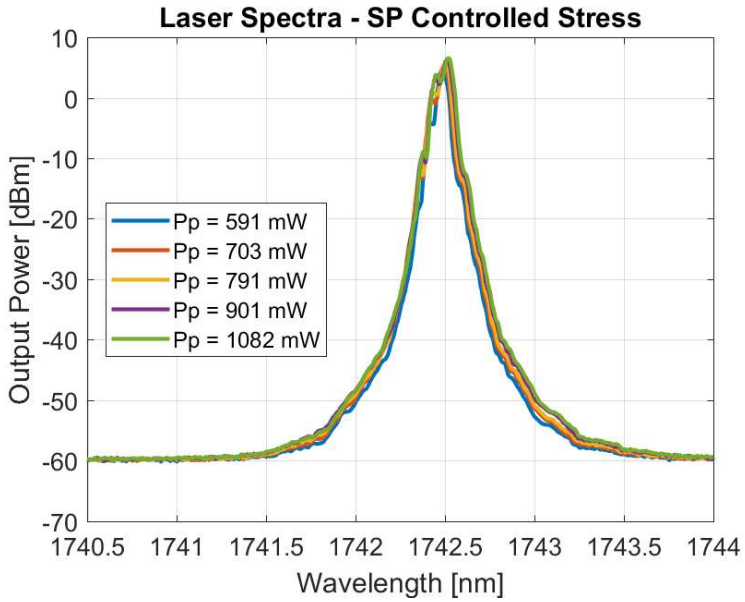

Figure 4-6 Laser SP operation spectra at multiple pump powers - stress induced.

4.3 Simulations

The following result section presents simulations spectra of the proposed SPSF design with a single varying parameter at a time. The spectral responses focus only on the DFB grating Bragg wavelength tuned to the FPFBG as the other DFB polarization does not interact with it.

The cavity spectral response for the proposed SPSF design is presented in Figure 4-7 for multiple external cavity lengths. The selected apodization function is a cosine function applied to a percentage (%) of the total grating length L. The FSR of the external cavity modes can be seen within the DFB grating stop band. As we increase the external cavity length from a) 0.5 mm to c)

3.2 cm, we observe that the number of transmission modes within the DFB grating increases. As previously discussed, these modes can achieve lasing and lead to multimode operation, hence the importance of reducing their presence in the DFB grating using a shorter cavity.

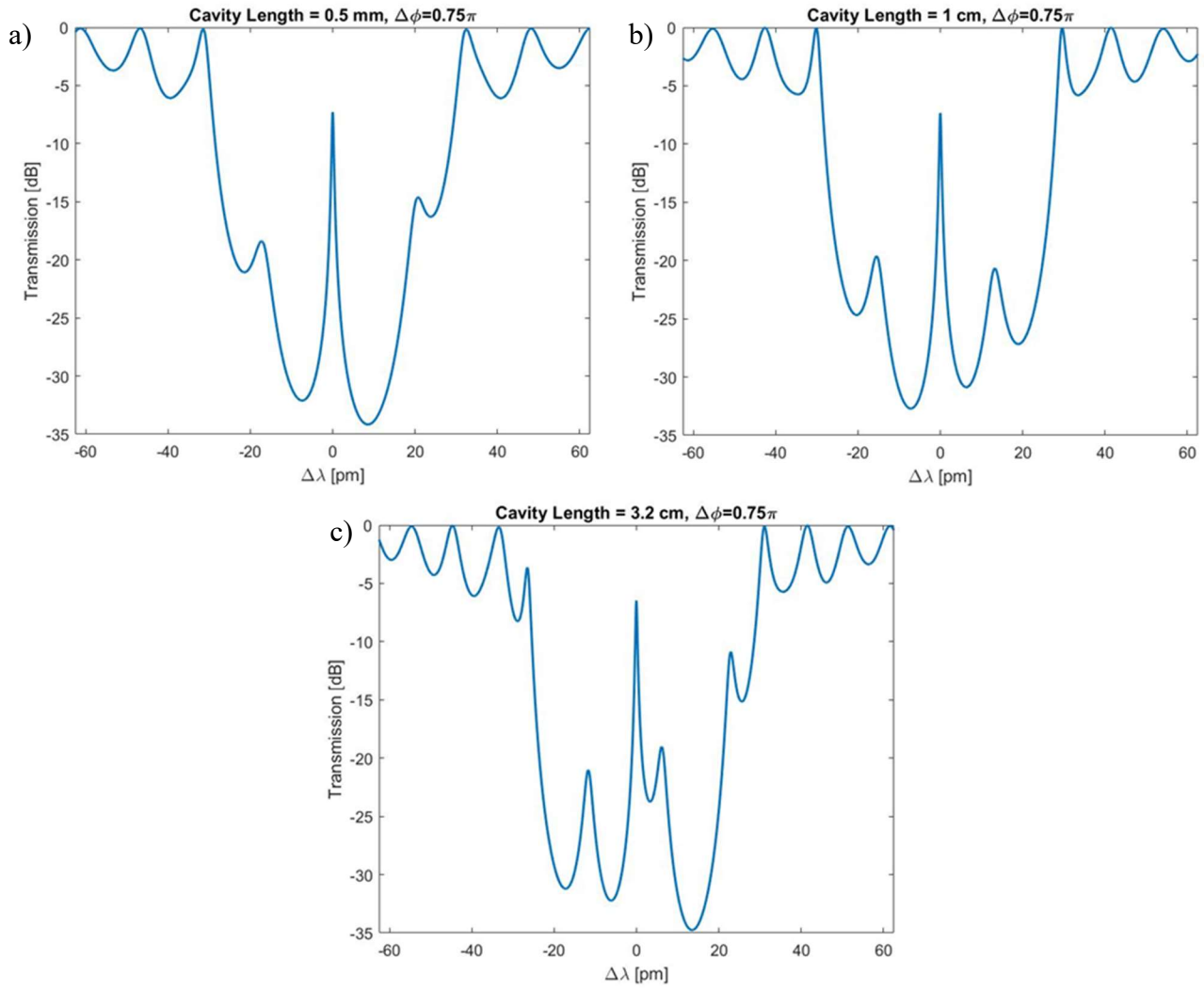

Figure 4-7 Simulated laser modes for multiple cavity lengths L: a) 0.5mm b) 1 cm, and c) 3.2 cm. The fixed simulations parameters are: phase detuning Δφ = 0.75π cm, DFB grating = 0.4L apodized, FPFBG = 0L apodized and R = 0.5, DFB grating and FPFBG centered at 1742 nm.

Figure 4-8 presents the simulations with varying phase relations between the DFB grating and FPFBG. The FPFBG resonant modes within the stop band shift towards longer wavelengths as $\Delta\phi$ increases, as expected from equation **(2.13)**. Furthermore from Figure 4-8 a) to d), we observe the periodic behavior of the central peak transmission due to the phase relation change between the

DFB grating and external cavity. We observe in a) a behavior close to an in-phase relation between the gratings resonant mode - where it has the highest transmission displayed, whilst the closest anti-phase behavior observed between the mode is in c) and consequently has the lowest transmission. This demonstrates the importance of the initial phase which dictates the maximum central mode transmission as well as the necessity to reduce phase shifts during laser operation.

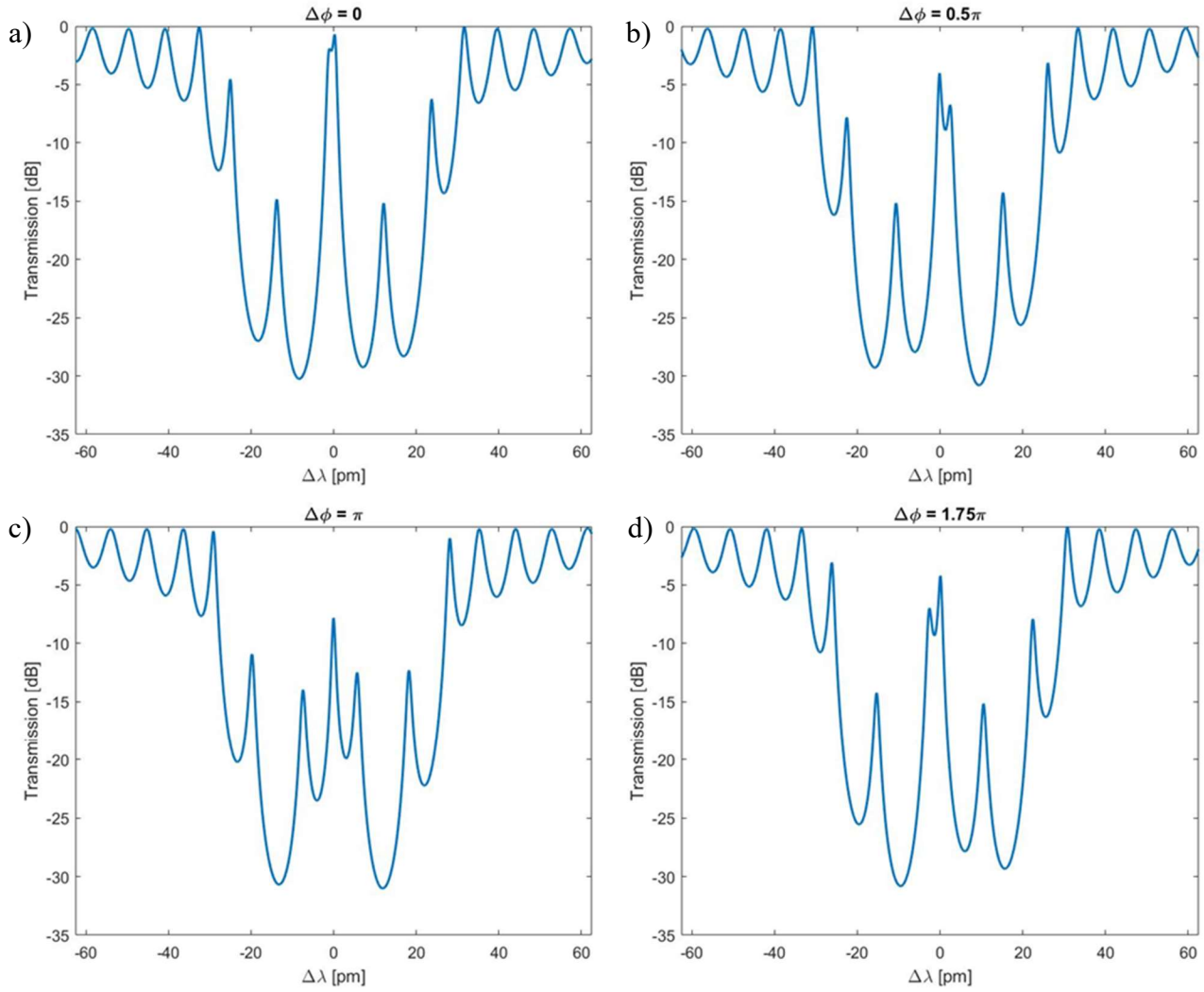

Figure 4-8 Simulated laser modes for multiple phase detuning from the external cavity modes: a) $\Delta\varphi = 0$, b) $\Delta\varphi = 0.5\pi$, c) $\Delta\varphi = \pi$ and d) $\Delta\varphi = 1.75\pi$. The fixed simulations parameters are: cavity length = 5 cm, DFB grating = 0.4L apodized, FPFBG = 0L apodized and R = 0.5, DFB grating and FPFBG centered at 1742 nm.

Equation **(2.15)** shows the relation between the phase and temperature. As the FPFBG length increases so does the phase sensitivity to temperature perturbations. This is highlighted in Table 4.1, where the temperature variation required in Tm doped fiber to achieve a phase shift of π at λ = 1742 nm is shown.

Table 4.1 Temperature variation required for a phase shift variation $\Delta\varphi = \pi$ in TDF for λ = 1742 nm.

Cavity Length (mm)	ΔT (°C)
0.5	25
10	12
32	4

The longer the cavity length, the lower is the temperature variation required for the same phase shift. This result further demonstrates the importance of a small external cavity length.

In Figure 4-9 we now simulate the cavity for increasing wavelengths detuning between the FPFBG Bragg wavelength and the DFB grating Bragg wavelength. We can observe two important behaviors. First, for small Bragg wavelength detunings, Figure 4-9 a) and b), the wavelength detuning acts like a phase detuning; this is expected as wavelength and phase are related by equation **(2.13)**. A second behavior occurs for higher Bragg wavelengths detuning. As it increases, the external FBG bandwidth overlaps less and less with the PS DFB grating bandwidth, Figure 4-9 c) to d), reducing the number of lateral modes in the cavity and their transmission until they are completely unmatched, and the discrimination scheme is negated. The PS DFB laser will then operate in its typical dual polarization regime.

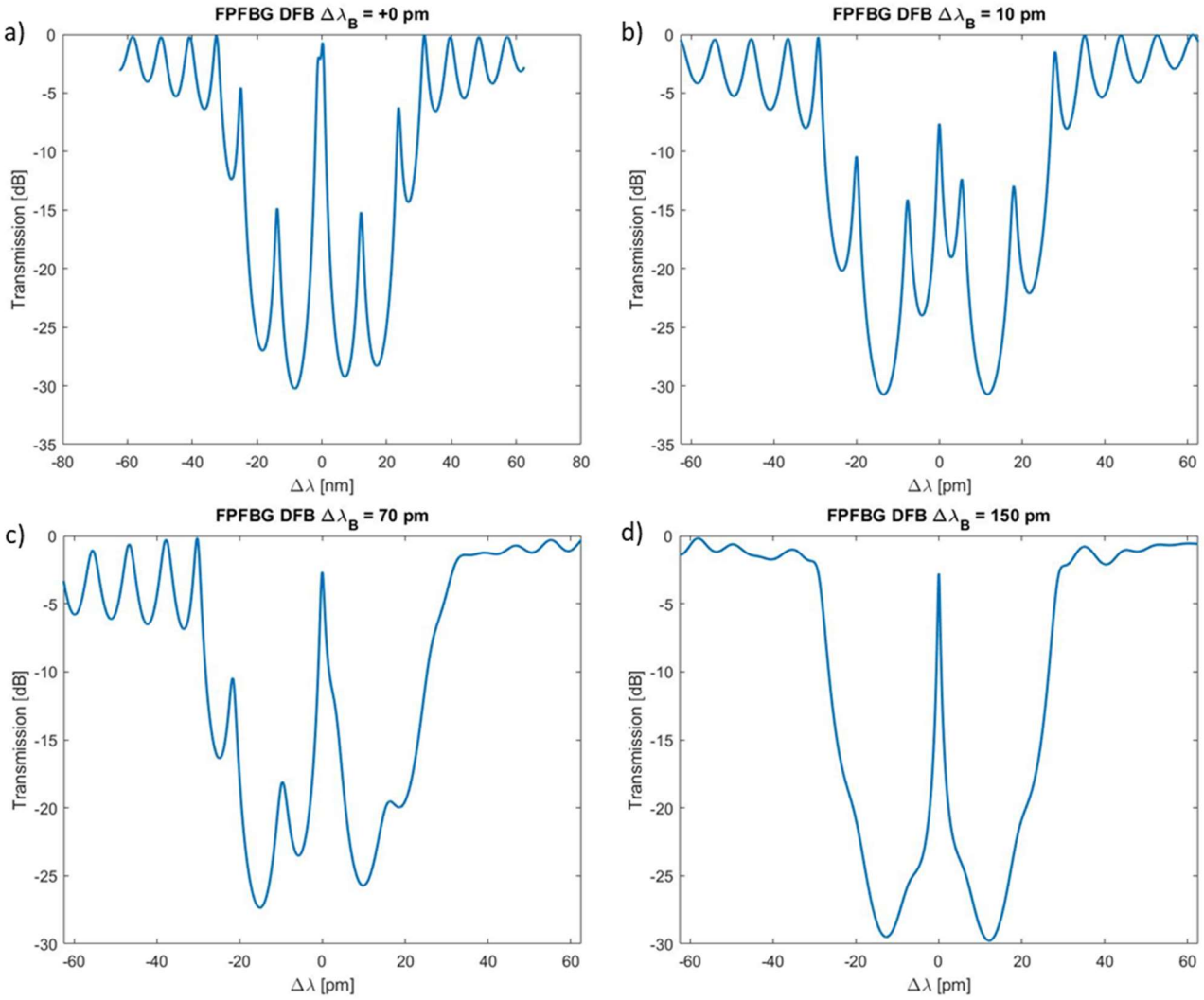

Figure 4-9 Simulated laser modes for multiple DFB grating central wavelength detunings from the FPFBG: a) $\Delta\lambda_B$ = 0 pm, b) $\Delta\lambda_B$ = 10 pm, c) $\Delta\lambda_B$ = 70 pm, and d) $\Delta\lambda_B$ = 150 pm. The fixed simulations parameters are: cavity length= 5 cm, DFB grating = 0.4L apodized, FPFBG = 0L apodized and R = 0.5, and $\Delta\varphi$=0.

4.4 Single Polarization (SP)

The following section presents results from the single polarization (SP) operation objective, related to the methodology in section 3.2.5. It aims to demonstrate the design SP operation functionality and limits.

FPFBG1 was the first FPFBG introduced in the test bench. When temperature tuned to the DFB grating fast axis, the laser displayed preferential polarization output. However, single polarization operation was not achieved, and the DFB grating remained in a multimode regime. This is believed to be due to FPFBG1 low reflectivity of 10%. The limited favored signal feedback to the DFB laser is not enough to break the dual polarization gain equilibrium. Thus, a stronger external fiber Bragg grating (FBG) was introduced, FPFBG2 with a reflectivity R = 50% and a cavity length of 1.90 m. This lengthy external cavity has a small free spectral range (FSR) of 54 MHz or 54 fm. This leads to a large number of modes within the stop band and modal instability from mode hops which is not desired for robust SF operation. This section focuses on SP operation characterization, the modal instability will be discussed in the next section along with single frequency (SF) operation. The unpumped reflection spectrum for SP operation is shown in Figure 4-10 for both a) temperature untuned and b) temperature tuned wavelengths.

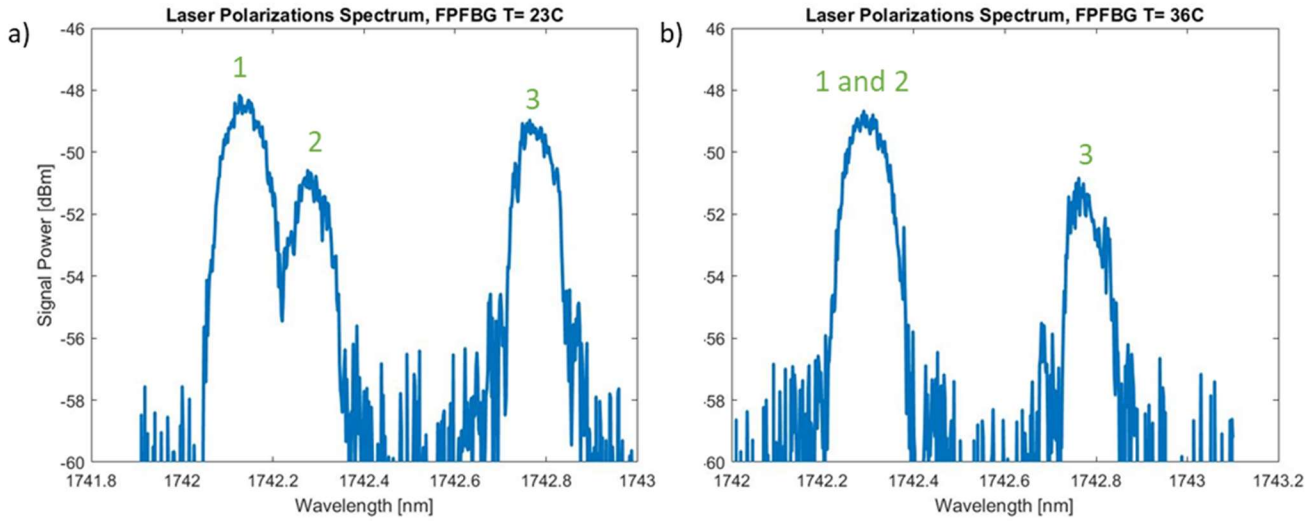

Figure 4-10 Laser cavity unpumped reflection spectra obtained with a -3 dB coupler and a supercontinuum source injected at port 3 (P3). FPFBG2 (1) and DFB laser polarization modes, (2) fast axis, and (3) slow axis for a) room temperature of 23 °C, and b) TEC heated to 36 °C.

At room temperature 23 °C (see Figure 4-10 a)), FPFBG2 Bragg wavelength is not aligned to neither of the DFB grating Bragg wavelength polarizations and thus requires TEC heating (see Figure 4-10 b)), where the FPFBG and fast axis are temperature aligned and Bragg wavelength tuned at 36 °C. The measured FPFBG2 full width at half maximum is 0.11 nm. The laser was pumped at low pump power (Pp) near threshold in both configuration; the spectra results are shown in Figure 4-11 with their respective Fabry-Pero interferometer (FPI) readings. The FPI readings show multiple FSR scans, its FSR = 1.5 GHz. We observe single polarization operation when FPFBG2 is temperature tuned, whilst the expected dual polarization regime is seen when temperature untuned.

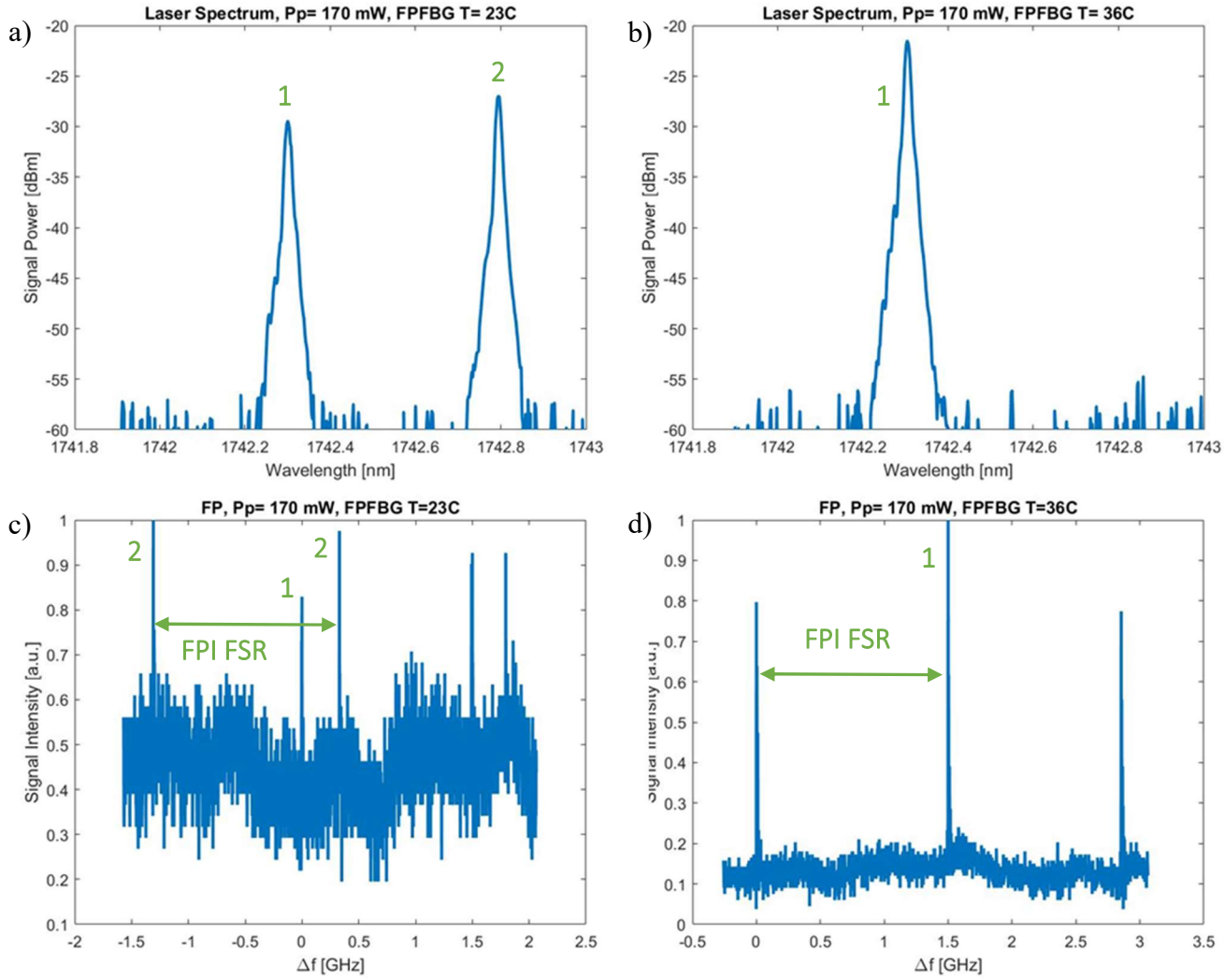

Figure 4-11 Laser spectra and FPI readings for 170 mW pump power for two different FPFBG2 temperatures, 23 °C and 36 °C. a) OSA, FPFBG2 not temperature aligned, b) OSA, FPFBG2 temperature aligned c) FPI, FPFBG2 not temperature aligned and d) FPI, FPGB1 temperature aligned. (1) fast axis, and (2) slow axis.

With the FPFBG2 temperature tuned at 36°C, SP operation is maintained up to Pp = 800 mW, after which it becomes unstable. Additionally, we observed mode hopping on the FPI equal to the external cavity FSR. This is reflected by the unstable output power read by the FPI, which is a typical characteristic of mode hopping [24, 92]. The second polarization was not captured by the optical spectrum analyzer (OSA) in Figure 4-12 a) due to its instability and higher integration time. In Figure 4-12 b) we observe a second peak associated with the slow axis polarization (see Figure

4-11). The loss of single polarization at higher pump powers is due to detuning between Bragg wavelengths of the FPFBG and the DFB grating fast axis. The generated heat from quantum defect leads to a loss of Bragg wavelengths overlap where the SP feedback design can be unstable or in the worst case simply null.

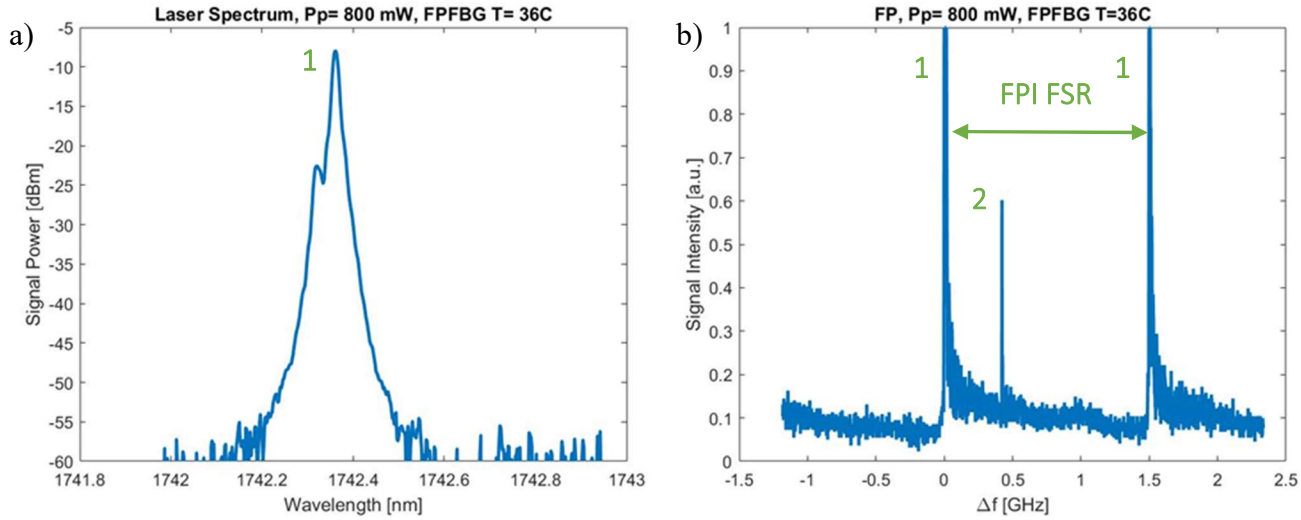

Figure 4-12 Laser spectra and FPI readings at 800 mW pump power. FPFBG2 temperature tuned at 36 °C a) OSA, FPFBG2 b) FP, FPFBG2. (1) fast axis, and (2) slow axis.

The spectrum in Figure 4-12 a) seems to suggest there is another mode lasing also within the fast axis -40 pm off from the main lasing mode. Hence, electrical spectrum analyzer (ESA) spectra were also taken and are shown in Figure 4-13 a) for Pp= 170 mW b) and Pp= 800mW. We observe a frequency beat of 4 GHz or 40 pm at 1742 nm for Pp= 800 mW and no frequency beat for Pp = 170 mW. The pump was then increased to maximum output power Pp= 1.3 W in both configurations, i.e., temperature tuned and untuned. The resulting spectra and FPI readings are presented in Figure 4-14. Multimode operation is now observed within both polarizations and is now visible on the FPI readings Figure 4-14 c) and d), unlike at Pp= 800 mW. This is due to the modes increase in power. The modes observed are again located at $\Delta\lambda$ = -40 pm from the main central mode. At this pump power the temperature difference between FPFBG2 and the DFB grating from the quantum defect is maximum. The second polarization is now observed on the OSA spectrum in Figure 4-14 a) and even for the temperature aligned configuration Figure 4-14 b).

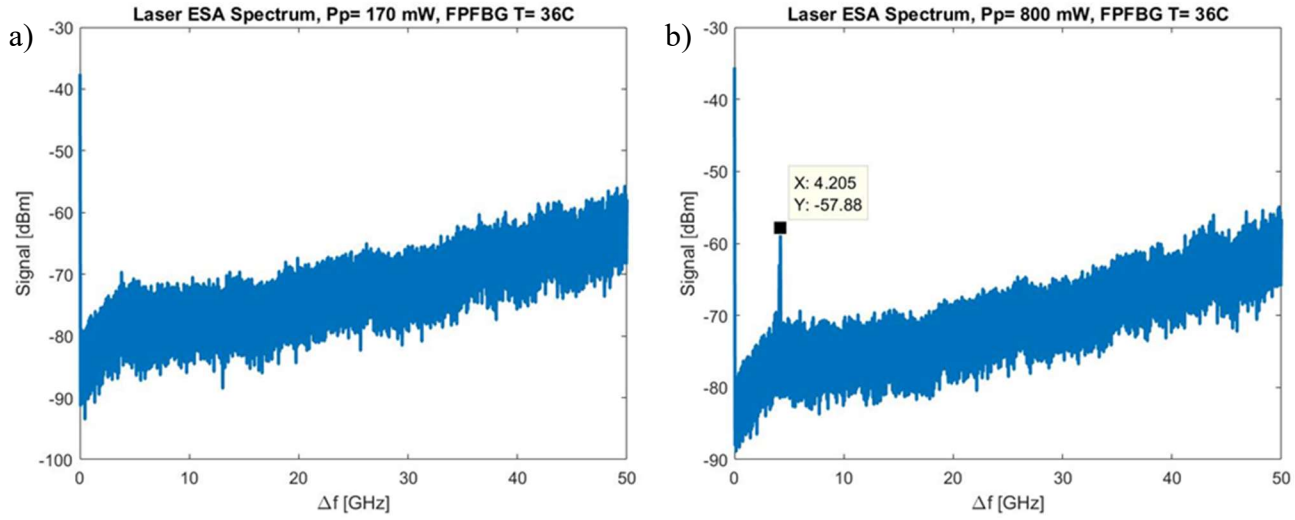

Figure 4-13 Laser ESA spectra for FPFBG T= 36 °C at a) P_p= 170 mW, and b) P_p= 800 mW.

Multimode operation could occur due to the external cavity modes within the DFB grating as seen from the simulations in section 4.3. However, the current modes observed do not correspond to the FSR of the FPFBG; its FSR is equal to 54 MHz or 54 fm at 1742 nm. Furthermore, the Bragg wavelengths overlap at maximum pump power is greatly reduced due to their temperature discrepancy so the impact of the FPFBG is supposed to be reduced if not negligible. This leads back to the phase-shifted DFB grating as the potential source of this extra unwanted mode.

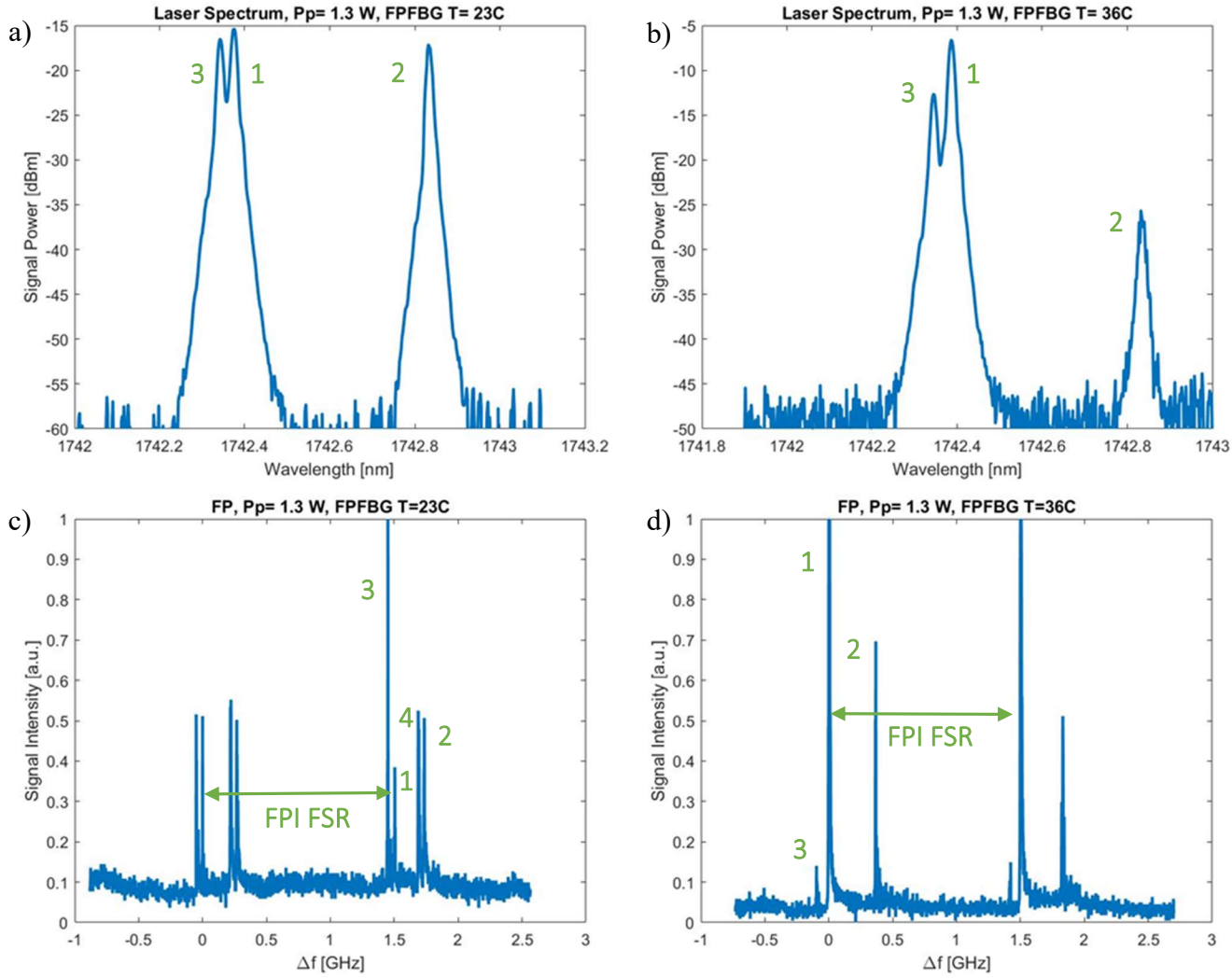

Figure 4-14 Laser spectra and FFPI readings for 1.3 W pump power for two FPFBG2 temperatures, 23 °C and 36 °C: a) OSA, FPFBG2 not temperature aligned b) OSA, FPFBG2 temperature aligned c) FPI, FPFBG2 not temperature aligned, and d) FPI, FPGB1 temperature aligned. (1) fast axis main mode (2) slow axis main mode (3) fast axis 2nd mode, and (4) slow axis 2nd mode.

The DFB cavity was simulated on its own without and overlapping FPFBG Bragg wavelength. The results are presented in Figure 4-15 a). We observe lateral modes 40 pm away from the central mode. At high pump power, Pp = 1.3 W, these higher threshold modes lase and become observable. These modes located at 40 pm are at the resolution limits of the OSA used to obtain Figure 4-4 which has a resolution of 50 pm versus the current OSA with a 10 pm resolution.

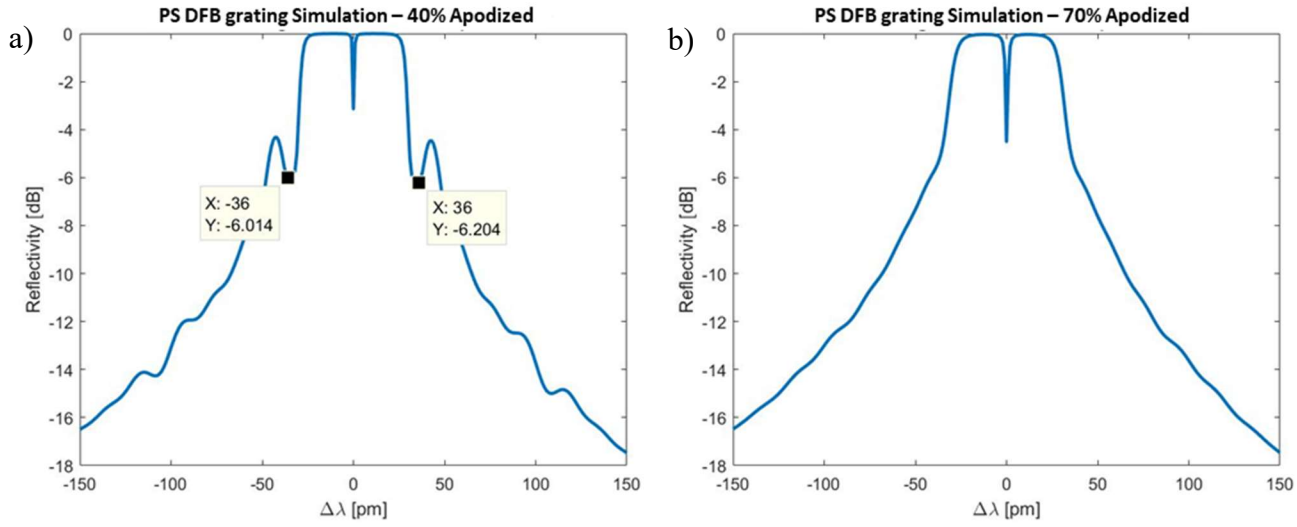

Figure 4-15 Simulated PS DFB laser reflection spectrum without an FPFBG. a) under test DFB grating simulated - 40% apodization (side modes are visible at 36 pm or ~0.04 nm from the main lasing mode) and b) simulated DFB grating with the same parameters - 70% apodization, without side lobes.

Figure 4-15 a) shows the PS DFB grating spectrum with an apodization over 40% of the grating length, Figure 4-15 b) shows the same grating with a higher apodization of 70%. This removes the side lobes and re-enforces single mode operation, however as previously discussed the apodization process reduces the effective length of the grating. Thus, to maintain a similar grating strength (κL) the RI modulation needs to be increased to compensate with a higher κ.

The laser output power for both configurations, Bragg wavelengths temperature tuned and untuned is presented in Figure 4-16. The values are taken at the DFB grating OC output (P2) and multiplied by 2 to consider the -3 dB coupler. We observe how the output power for the same pump power is higher for the temperature tuned configuration versus its untuned counterpart - this is highlighted in red for Pp = 700 mW where there is a 77% increase of the output power between both configurations. In single polarization (SP) operation, for the same pump power, the feedback signal allows the gain to be more efficiently utilized for the main dominant mode as noted in self-injected mechanisms [64, 65]. The readings displayed instability from mode hops, which is why the output power is not linear as shown in Figure 4-16, even if the data points correspond to averaged values

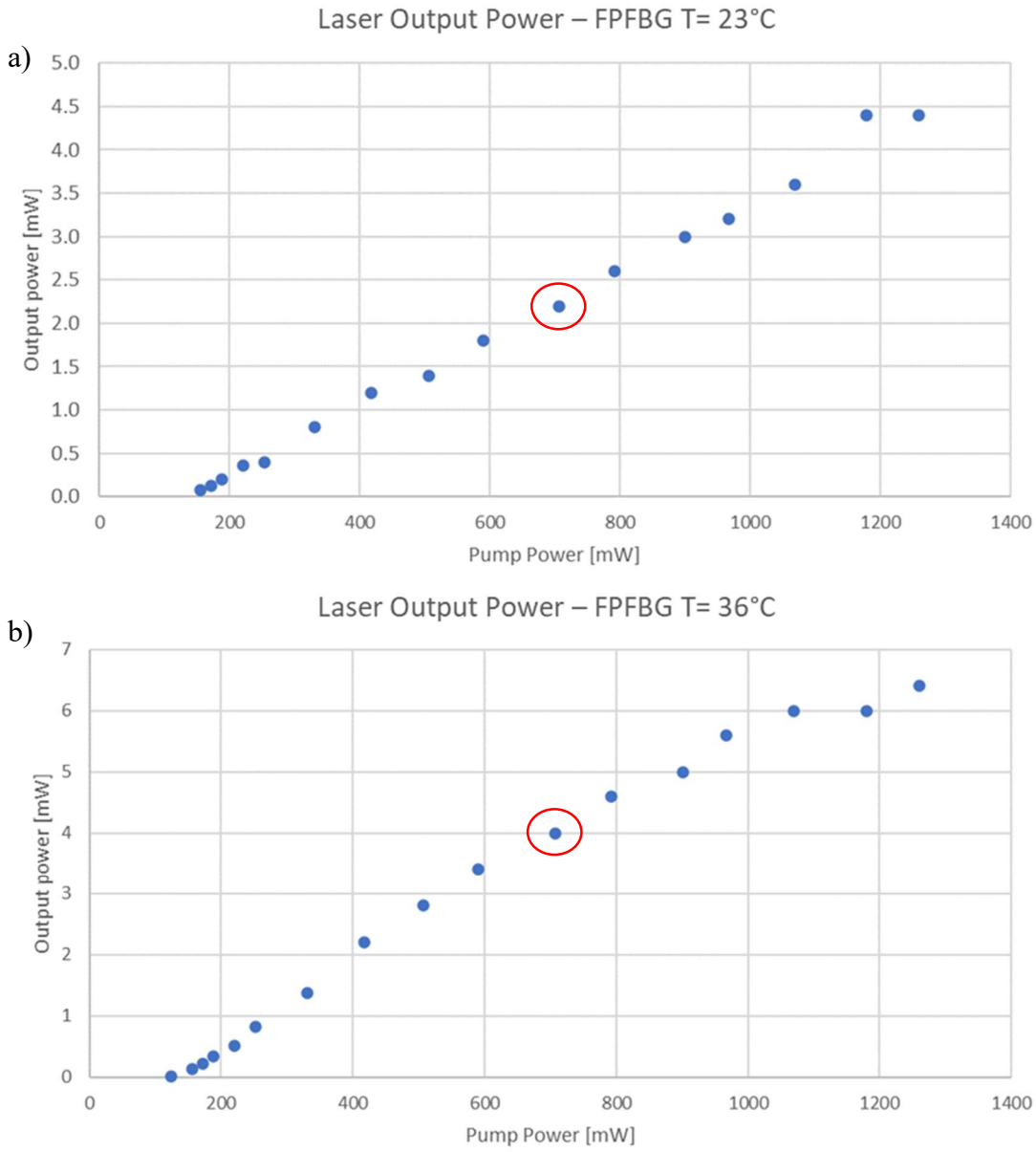

Figure 4-16 Laser output power, at P2, for FPFBG2 a) temperature unaligned and b) temperature aligned. The output power for P_p = 700 mW is circled in red.

In the following results, the FPFBG temperature was increased to see if the non-uniform temperature Bragg wavelengths detuning induced by the increasing pump power could be corrected. This would confirm the detuning claim and test its limitations. Previously, SP operation was lost when the FPFBG was temperature tuned at 36 °C and operating at Pp = 800 mW. With FPFBG temperatures increased to 41.3 °C and 43.2 °C, SP operation was successfully achieved for

Pp = 800 mW and 900 mW respectively. The resulting OSA and FPI readings are shown in Figure 4-17 for both temperatures.

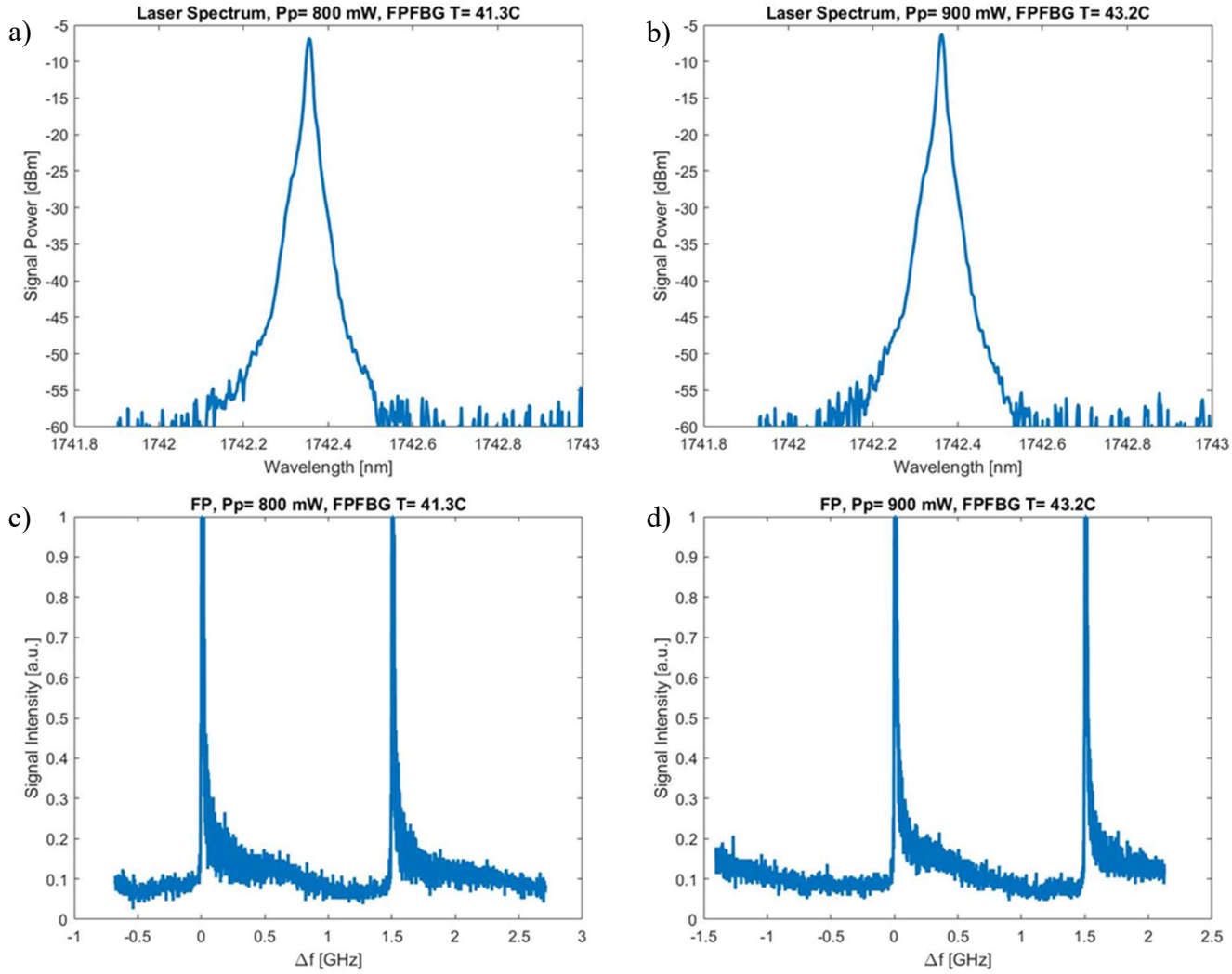

Figure 4-17 Laser spectrum and FPI readings. SP operation is achieved at higher pump powers with increased FPFBG2 temperatures to compensate for the heat induced Bragg wavelengths detuning. P_p = 800 mW, FPFBG2 T = 41.3 °C a) OSA b) FP, P_p = 900 mW, FPFBG2 T = 43.2 °C c) OSA d) FP.

Interestingly, this shows that although the effects from quantum defect in the phase shift region are not removed, re-aligning the lasing mode to the external FBG can achieve SP operation regime. Nonetheless there are several potential limitations for this method due to the increasing pump power. As the pump power increases, temperature effects and high-power effects become more

important. This can include lasing for previously under threshold modes, non-linear effect generation from the high intensity in the PS region, and an increasing induced chirp. A chirped PS DFB leads to output power degradation as the effective length reduces reflectivity translating into more cavity losses. This in turn also reduces the Q-factor and hence can increase the laser linewidth. Attempts to achieve SP at higher pump power were unsuccessful, probably due to a combination of the previously mentioned factors. Lastly, FPFBG2 cavity length was reduced from 1.90 m down to 0.7 m to remove mode hopping behavior. This was unsuccessful with 0.7 m; mode hops were still observed using the Fabry-Perot interferometer with values equal to the cavity FSR.

We have demonstrated the proposed design SP operation functionality. The results confirm that quantum defect is highly detrimental to SP operation by detuning the FPFBG and PS DFB grating Bragg wavelengths. This can be compensated at higher pump powers by re-tuning the cavity. However, increasing the pump power exposes the laser to more undesired instability that can hinder SP operation. With such a lengthy cavity, robust SF operation is not possible as expected. SF operation confirmation and robust operation investigations are presented in the following section.

4.5 Single Polarization Single Frequency (SPSF)

The following section presents results from the single polarization single frequency (SPSF) operation objective, related to the methodology in section 3.2.6. This section aims to demonstrate SPSF functionality and its robust operation.

4.5.1 FPFBG3

In the single polarization operation results, the consequences of phase resonance and reflectivity from the external FBG (FPFBG) and phase-shifted DFB Bragg wavelengths tuning were investigated by heating only the FPFBG. The PS DFB grating was isolated and thus remained unaffected by the TEC temperature due to the high cavity length. However, this high cavity length is undesired for SF operation. For SF operation, the FPFBG needs to be pre-emptively Bragg wavelength matched to the PS DFB grating, and as both PS DFB grating and FPFBG lay on the same metallic plate, the Bragg wavelength temperature tuning range is much more limited. FPFBG3 and 4 were tested in this configuration. FPFBG3 Bragg wavelength overlap with the DFB

grating is less than FPBG4 whose Bragg wavelength overlap with the PS DFB fast axis wavelength is more important. FPFBG3 was first inserted in the new setup and tested at multiple lengths to determine a minimal cavity length free of mode hops. The tested lengths are shown in Table 4.2, with the first mode-hop-free length being 8.8 cm.

Table 4.2 External cavity lengths tested with FPFBG3 for mode-hop-free operation.

L_{Cavity} (cm)	FSR (MHz)	Mode Hops
75	137	yes
50	205	yes
15	684	yes
8.8	1170	no
4.4	2330	no

The FSR for an 8.8 cm cavity is 1.17 GHz, the DFB grating stop band has a bandwidth of a few GHz (~ 6 GHz from the simulations in section 4.3). This 1.17 GHz FSR might prevent mode hops, but there are still several transmission modes within the grating main bandwidth. FPFBG3 cavity length was then reduced to 4.4 cm and the unpumped spectrum was taken at different plate temperatures. The results are shown in Figure 4-18 for three temperatures. As the plate is cooled from room temperature (Figure 4-18 a)) to -3.4 °C (Figure 4-18 b)) or -5.6 °C below room temperature (Figure 4-18 c)), we observe that both gratings shift towards lower wavelengths. However, the PS DFB grating central wavelength overlaps more and more with FPFBG3. This suggests that the thermo-optic coefficient for TDF is higher than for SMF-28. To confirm this behavior the Bragg wavelength response to temperature of TDF and SMF-28 at λ = 1742 nm was measured. Leading to the following results: $\frac{\Delta\lambda}{\Delta T}$= 16 pm/°C for TDF and $\frac{\Delta\lambda}{\Delta T}$= 13 pm/°C for SMF-28. This confirms both observations from Figure 4-18. First, TDF and SMF-28 do not have the same thermo-optic coefficient leading to a distinct response. This re-enforces the need to ensure temperature tuning of the laser does not break SPSF operation. Second, their thermo-optic coefficient values confirm that thulium doped fiber will experience a higher wavelength shift than SMF-28 for the same temperature variation. Then, according to the expected laser temperature operation, the FPFBG Bragg wavelength can be written with an offset to optimize its operation at the required temperature of operation or vise versa.

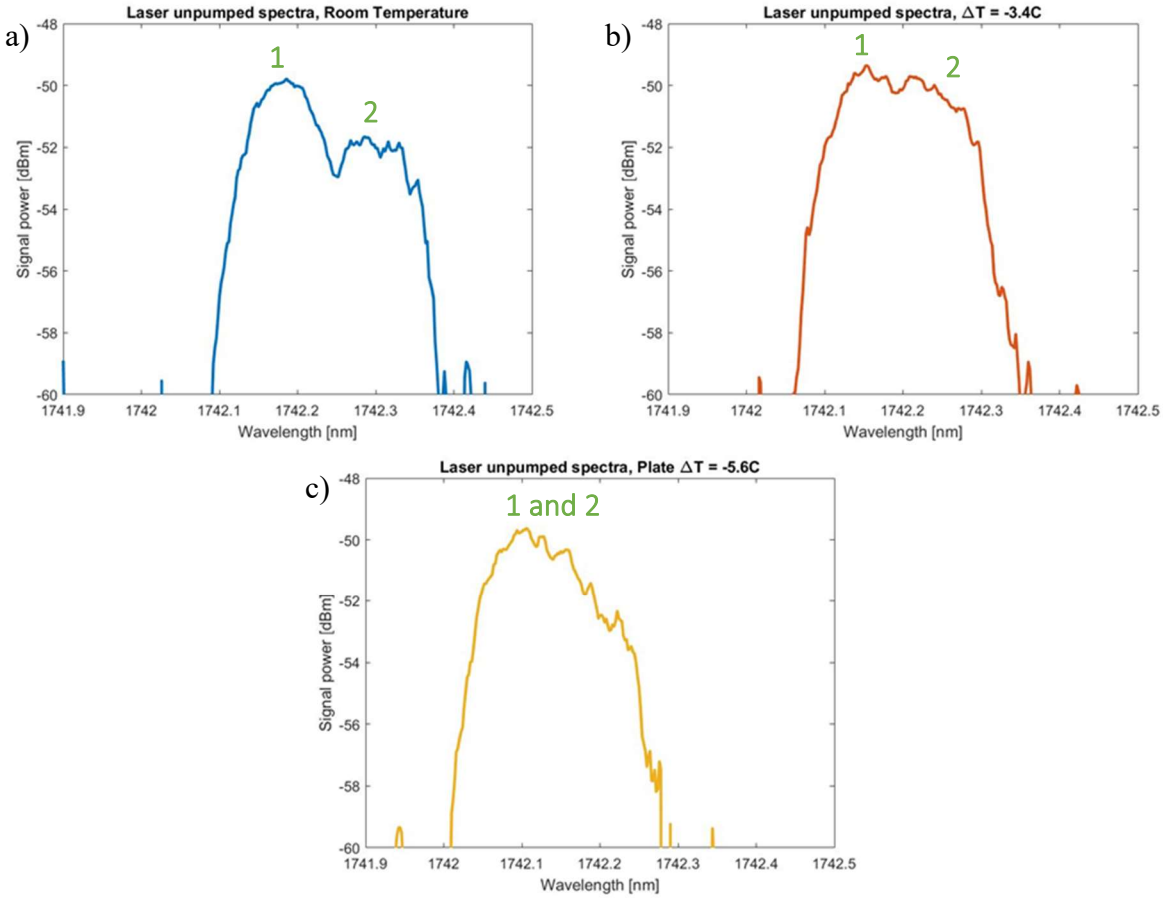

Figure 4-18 Laser unpumped spectra at 3 different plate temperatures with FPFBG3. Plate a) room temperature, b) cooled by 3.4 °C, and c) cooled by 5.6 °C. (1) FPFBG3 and (2) PS DFB grating fast axis.

The laser was then pumped, and its output power and regime of operation were observed at two plates temperatures. The results are shown in Figure 4-19 at a) room temperature and b) cooled by 5.6 °C. There are a few observations to highlight, the first one being the non-linear laser output power. This can be attributed to two phenomena: the higher output power with higher pump power typical of lasers and the variation in phase relation from the quantum defect. The temperature increase in the DFB grating shifts its wavelength of operation whilst the FPFBG remains at constant temperature inducing a phase shift between both gratings' modes. The effect of a phase shift leads to a change in transmission and a collapse of SP operation when the phase is in anti-phase. This also explains the change of polarization operation with increasing pump power from the quantum defect which generates heat. Lastly, we observe an important increase of output power for a

constant pump power when cooling the laser. This is attributed to a better heat exchange between the DFB grating and the metallic plate.

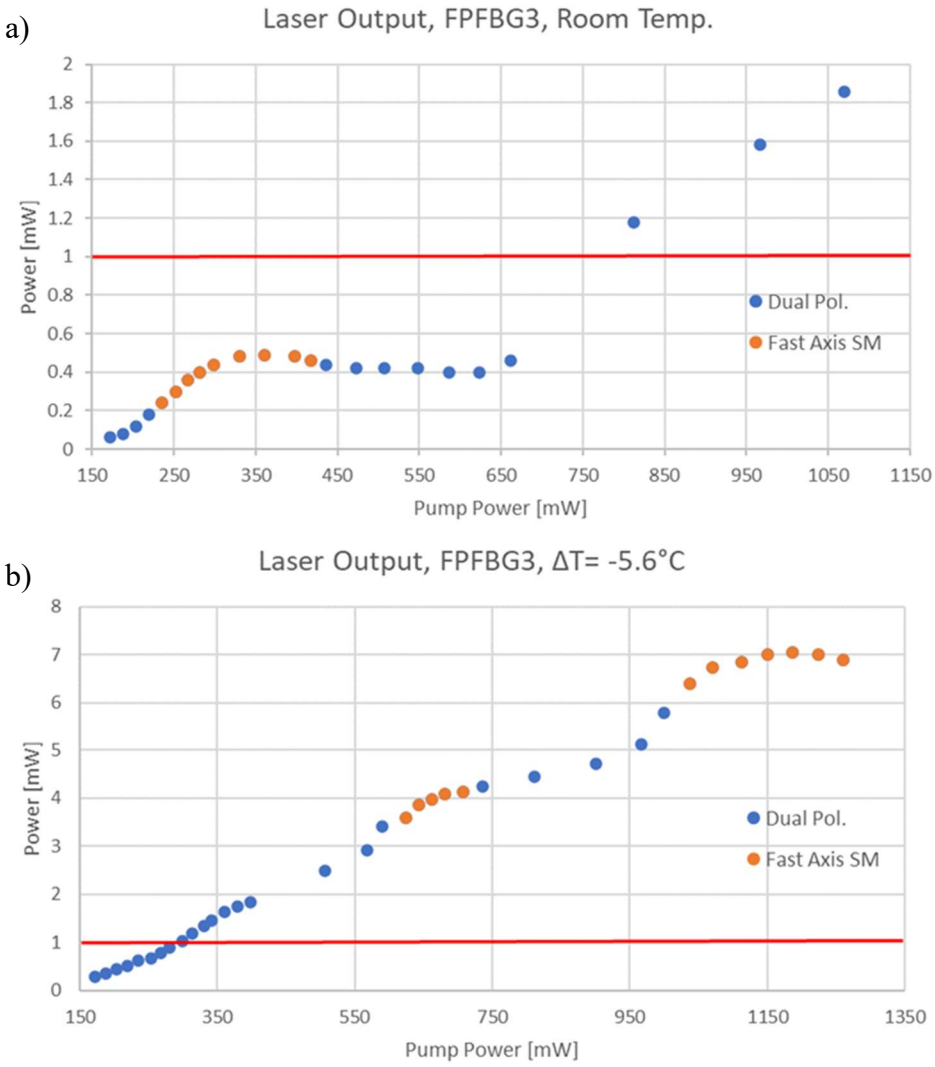

Figure 4-19 Laser output power with FPFBG3 at a) room temperature and b) cooled by -5.6 °C. The red line corresponds to the power requirement of 1 mW.

This section demonstrates the different thermo-optic coefficients for SMF-28 and TDF at 1742 nm which impact the coupled-cavity phase relation. By quantifying the Bragg wavelength temperature shift, their Bragg wavelengths writing can be controlled to ensure good overlapping between one another by considering the desired Pp and temperature of operation. Finally, we determined a safety cavity length limit for mode-hop-free operation of 8.8 cm.

4.5.2 FPFBG4

FPFBG4 was then inserted in the test bench. To reduce the phase variation sensitivity to temperature and further increase the FSR, FPFBG4 was spliced with a shorter cavity length, 3.2 cm. The resulting FSR is 3.21 GHz. This further reduces the number of transmission modes within the cavity. Figure 4-20 shows the unpumped spectra for FPFGB4 focused on the FPFBG and PS DFB grating fast axis for the metallic plate a) at room temperature and b) cooled by 3.75 °C. At room temperature, we observe how the bandwidth overlap is higher than for FPFBG3 (see Figure 4-18).

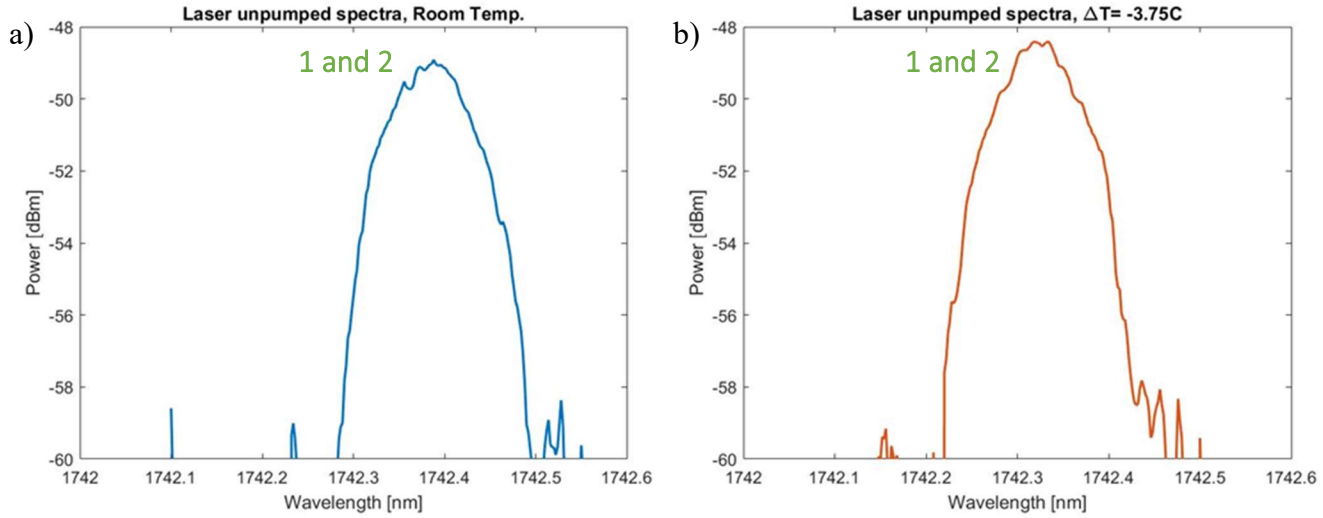

Figure 4-20 Laser unpumped spectra at 2 different plate temperatures with FPFBG4: plate a) at room temperature and b) cooled by 3.75 °C. (1) FPFBG4 and (2) PS DFB grating fast axis.

Once inserted, we characterized the laser frequency shift induced by the cavity detuning from the quantum defect. The results are shown in Figure 4-21 a) at room temperature and b) cooled by

3.75 °C. We observe in both instances the three different polarization operation regimes: dual polarization, fast axis single mode, slow axis single mode and their respective transitions.

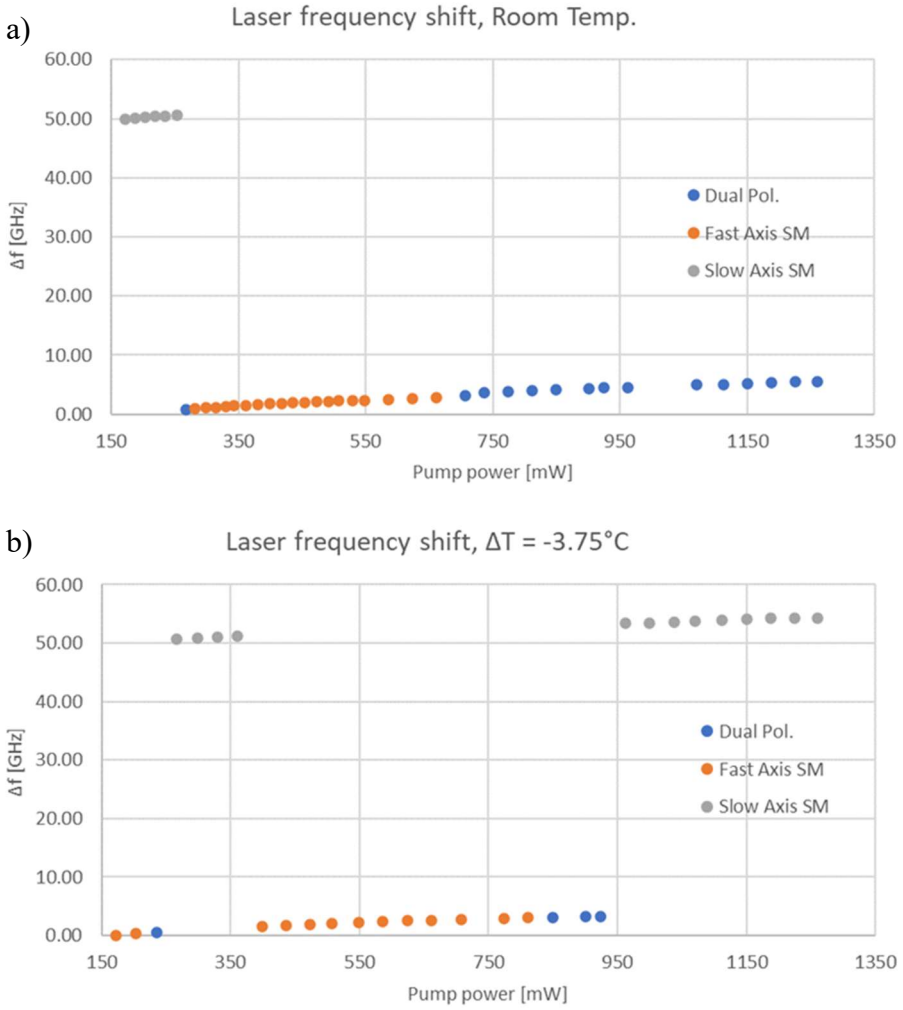

Figure 4-21 Laser frequency shift induced by P_p: a) at room temperature, and b) cooled by 3.75 °C.

The three polarization operation regimes are observed in Figure 4-21, but they were not observed using FPFBG3 at room temperature despite the same Pp range as in Figure 4-19 a). This can be explained by the different cavity length and Bragg wavelengths overlap, which changes the phase as seen from equation **(2.13)**. The polarization regime changes once again for the whole Pp spectrum when the laser is cooled in Figure 4-21 b), due to another initial phase shift but this time from temperature, i.e., the polarization regime associated to a Pp is different and the polarization

transitions occur at different Pp . Figure 4-22 zooms on the fast axis shift, we see how the frequency shift for the same Pp is higher for the laser at room temperature in a), compared to the cooled laser in b). The dual polarization regime shifts presented follow the fast axis shift. This is in agreement with the increase in power from cooling observed in Figure 4-19. A better heat dissipation from cooling reduces the induced chirp in the cavity.

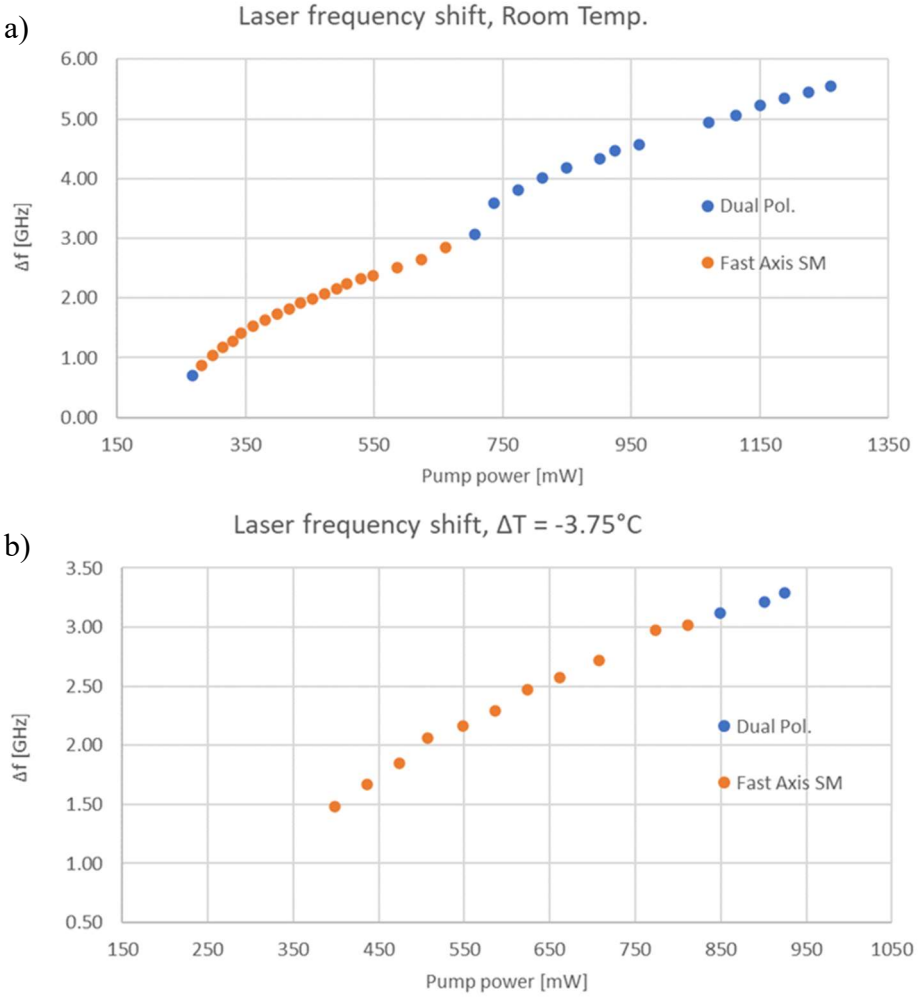

Figure 4-22 Laser frequency shift induced by P_p zoom on fast axis. a) room temperature, b) cooled by 3.75 °C.

Similarly, to FPFBG3, the output power for the laser with FPFBG4 was characterized at room temperature as seen in Figure 4-23. The minimal output power requirement of 1 mW with a SPSF operation is achieved for a low Pp of 330 mW up to 650 mW.

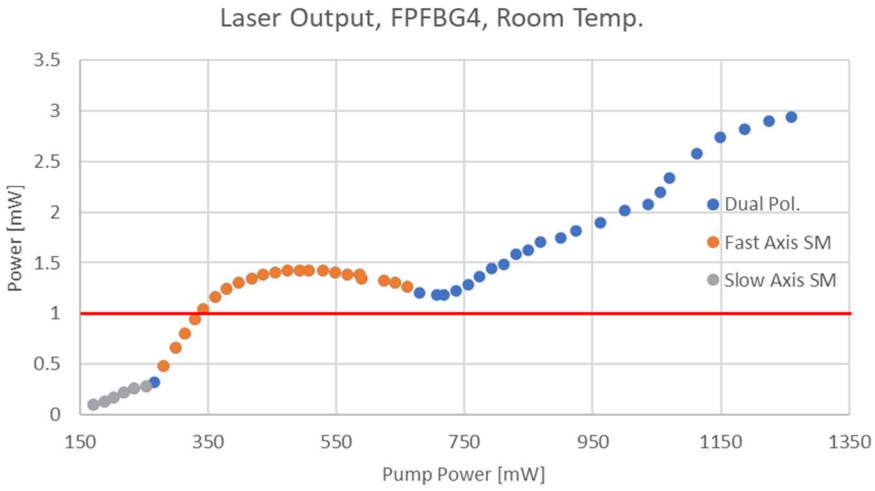

Figure 4-23 Laser output power with FPFBG4. The red line corresponds to the power requirement of 1 mW.

The spectrum was taken at multiple Pp, Figure 4-24 presents the laser spectra for Pp = 361 mW, and Pp = 586 mW where it operates in what seems to be in a single mode regime. Their respective output power is also displayed.

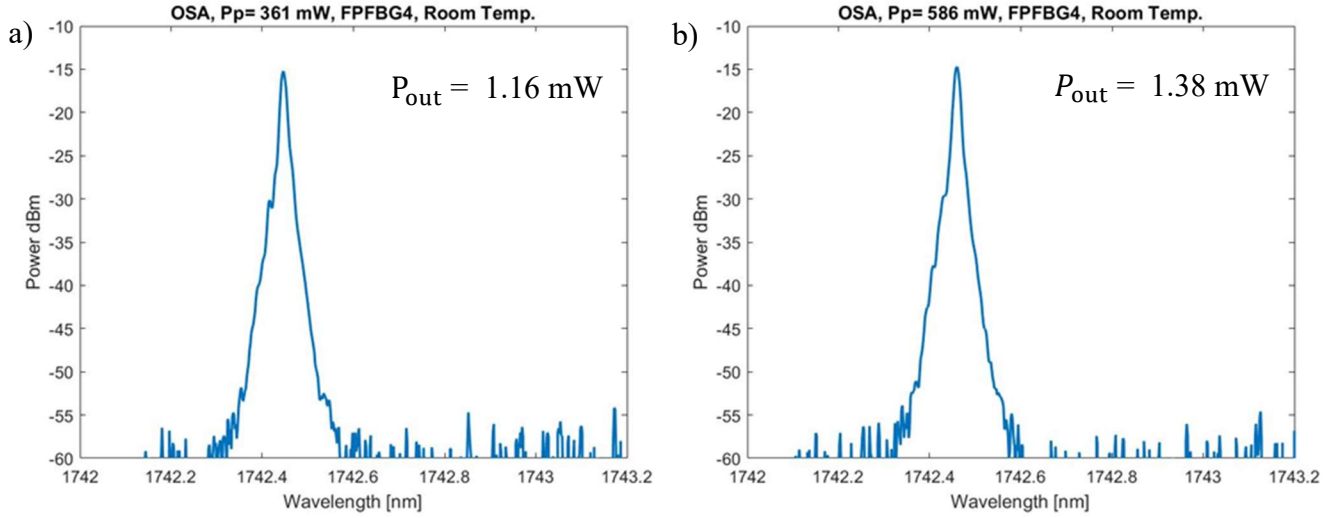

Figure 4-24 Laser spectra at room temperature for a) P_p = 361 mW and b) P_p = 586 mW with their respective output power.

Measurements with the FPI and ESA were taken to confirm SPSF operation. The FPI results are presented in Figure 4-25 for both pump powers with their respective FSR in a) and c) displaying

SF operation. ESA measurements did not show any frequency beat. The SF peaks were zoomed in confirming SF operation and their FWHM measured. The results are presented in Figure 4-25 b) and d) for both Pp. The asymmetry of the peaks is attributed to the input signal alignment with the interferometer. The laser output port is connected to the FPI using a FC/PC adaptor which then couples in the FPI cavity. The FPI model does not offer integrated alignment tools and would thus require preinjection alignment tuning to eliminate the peak shape. The respective FWHM values measured are also presented with values close to 8 MHz or 81 fm at $\lambda = 1742$ nm. As expected with this cavity length (L=3.2 cm) no mode hopping was observed.

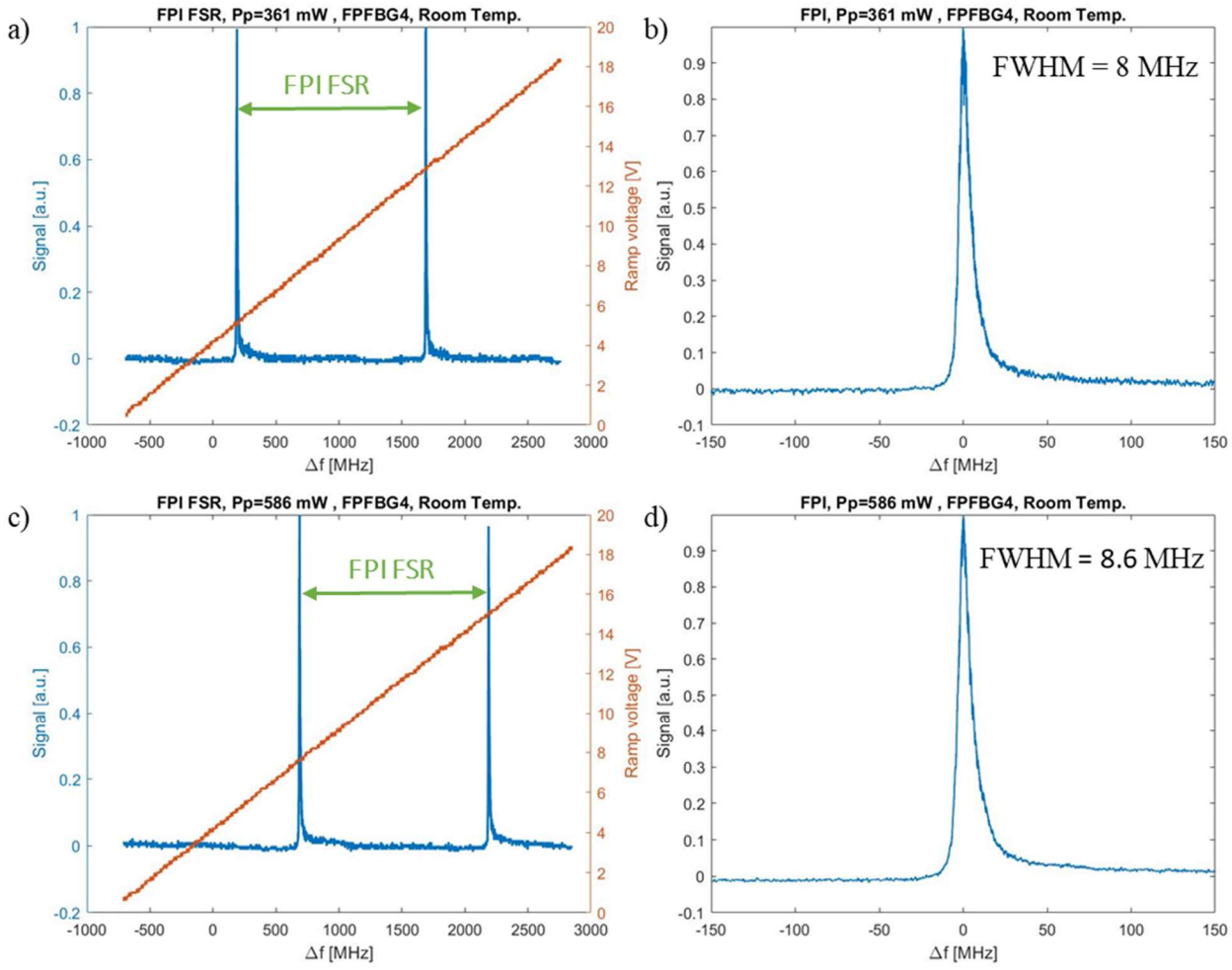

Figure 4-25 Laser linewidth measurements at room temperature for c) $P_p = 361$ mW d) $P_p = 586$ mW with their respective FSR a) and b).

The dynamic behavior of the single mode, its stability, was also observed using the FPI for both pump powers. The maximum peak drift is 30 MHz or 0.3 pm at λ = 1742 nm, which is compliant with the required stability of a maximal value of 1 pm for strontium 87 optical lattice application.

So far, we have demonstrated the SPSF operation of the design with an output power over the required 1 mW. Furthermore, this output power was achieved at low pump power, an advantage for low power consumption. We have highlighted the role of the initial phase relation dependence with the cavity length (optical path) and with the laser operation temperature. The following last results demonstrate robust SPSF operation under temperature and strain tuning.

With both TDF and SMF-28 having a different thermo-optic coefficient their Bragg wavelength temperature response varies one to another. Naturally, the same can be expected for the strain response since both fibers have a different fabrication process and components, e.g., stress rods. With strain being a common method for laser tuning this investigation is even more important. The laser strain is induced with a micrometric translation stage and fiber clamps at the laser extremities. The corresponding frequency shift is measured. Similarly, the metallic plate temperature over which rests the laser was changed and the frequency shift measured. The results are presented in Figure 4-26 a) for the temperature response and Figure 4-26 b) for the strain response. The SPSF operation was maintained throughout the tuning for both methods whether slowly varying or rapidly varying, demonstrating robust SPSF operation. For temperature, we previously observed the collapse of single polarization operation during the increase of pump power related to a frequency shift $\Delta f = 2$ GHz at room temperature whereas robust SP operation is shown during laser tuning over a $\Delta f = 7$ GHz. The response to temperature differs for both fibers, hence we could expect to see a collapse of SP operation. However, in the quantum defect shift case, the detuning is increased within the laser itself and the temperature difference between both gratings is more important.

Previous calculations for TDF achieved a phase shift $\Delta\varphi = \pi$ for a cavity length of 3.2 cm at ΔT = 4 °C, see Table 4.1. The values are similar for SMF-28. This is a value within the temperature variation performed during the tuning, which means the laser has cycled through the phase and anti-phase regime while maintaining SPSF operation. This demonstrates robust SPSF operation, but further characterization would be required to better understand the mechanism and its

limitations. Indeed, this robustness might come from the phase inability to reach anti-phase behavior due to the initial phase. This initial phase is then modified by a minimal amount from the TEC ±0.1°C temperature variation resolution. Characterizing the initial phase range from which the laser can be temperature controlled while maintaining SPSF operation is a valuable information for a robust manufacturing process control.

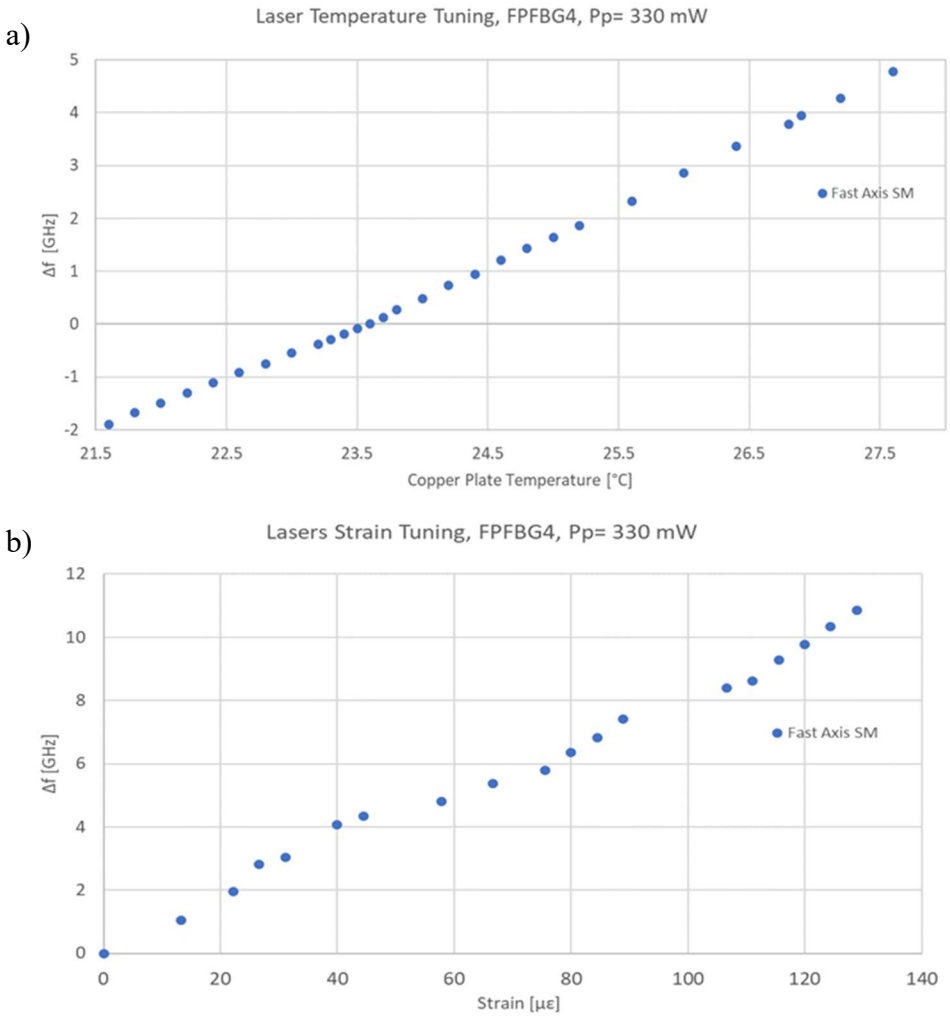

Figure 4-26 Laser tuning with FPFBG4 using a) temperature and b) strain at a constant P_p = 330 mW.

In this section we demonstrated robust SPSF operation for our laser whose required specifications for Sr^{87} optical lattice application were met: SPSF operation, 1 mW of output power minimum and noise under 1 pm. We further investigated the laser robustness determining the important role of

pump power and initial phase for the polarization regime response. Under temperature and strain tests, the laser remained SPSF and mode-hop-free. We highlighted potential limitations and future investigations to test for better understanding of the tuning and SPSF dynamic.

CHAPTER 5 DISCUSSION AND RECOMMENDATIONS

Simulations of the proposed design highlighted the key parameters expected to influence the desired laser behavior. These limitations were first discussed in the literature review in Chapter 2, section 2.4.7. Solutions were identified, implemented, and demonstrated in the realization of a single polarization single frequency (SPSF) laser with the required specifications, while the limitations were expanded and quantified. In the following chapter the secondary objectives are presented with their respective results. The design limitations are discussed with the results and put into context with other state-of-the-art methods for SPSF operation in fiber lasers. As the state-of-the-art, emphasis is placed on the discussion of three methods: FBG writing using linearly polarized light, the short-cavity polarization axis alignment, and the selective wavelength feedback with a non-polarization maintaining (PM) fiber. Finally, recommendations and future steps are also discussed throughout the chapter.

5.1 Laser Fabrication

The proposed design relies on three fiber types for its functionality: PM, PM TDF, and low birefringence fiber, and thus 2 custom splices. From the perspective of cost reduction and ease of access, this research shows how the requirements are reduced to 2 fiber types: PM TDF and SMF-28 with MFDs of 5.6 μm and 10 μm respectively. The mode field diameter mismatch between both fibers was the first challenge encountered and is a limitation of the proposed design due to its high impact on waveguide losses [77, 87]. The pump to WDM splice ensures maximum power in the gain medium for increased laser efficiency and reduction of pump threshold. A poor TDF PM to low birefringent splice results in an increase in loss for the laser cavity, which reduces the Q-factor [21] and reduces the reflected signal power, required for SP operation. The FBG linearly polarized writing method eliminates the need for a splice point inside the cavity which is a major advantage over methods requiring an intra-cavity splice such as short-cavities and selective polarization feedback designs [38, 66]. The effect of a lower reflected signal was observed when FPFBG1 was introduced as the low birefringence fiber. We believed its low signal reflectivity R = 10% limited SP operation compared to FPFBG2 R = 50%. Pre-programmed splice recipes yielded poor results, with transmission losses of 85% which greatly incapacitated the laser operation. Nonetheless, this limitation was greatly improved with a custom developed splice resulting in over 98% signal

transmission. The waveguides junction losses could further be improved with a careful selection of a low birefringence fiber with a closer MFD match to the PM TDF. The mechanical integrity of the splice was also tested with strain tests withstanding up to 140 kpsi. This test is critical for laser strain tuning and FBG writing, where the fiber is placed on the stage with strain for position uniformity and for better writing control.

The literature points toward high signal reabsorption for Tm doped fiber characterization near 1.7 μm [39] and thus a lower signal emission at 1.7 μm versus at 1.9 μm signal [73]. The value obtained for the absorption coefficient characterization of the PM TDF in this work was quantified 0.4 dB/cm near 1.74 μm. Amplified spontaneous emission and gain measurements show similar value, for 1.9 μm and 1.7 μm. The TDF selected for this research can thus be expected to face the same challenges when designing short cavities near 1.7 μm as the ones presented in the literature [74]. The fabrication of the phase-shifted (PS) DFB grating by my colleague Frederic Monet, and the implementation that followed resulted in an operational 1742 nm PS DFB laser in Tm PM fiber, achieving the goal set by objective (1). The DFB grating is 10 cm in length and was inscribed with a 1.5 mW 213 nm wavelength UV source. Other PS DFB 10 cm long gratings were written and achieved lasing. However, attempts to make shorter DFB gratings, 5 cm in length were unsuccessful. The RI modulation process is proportional to the incident light power [24]. The UV light power used to inscribe the gratings was increased up to 5 times the power used for the 10 cm gratings, thus achieving multiple grating strengths of lower and higher value than the DFB grating presented in this work. There could be several reasons why the 5 cm grating would not lase, possibly due to the fabrication process but which are beyond the scope of this thesis, however it could also be related to the PM TDF. These results highlight the need for future investigations on exploring the limitations of inscription in the selected TDF PM fiber. These limitations could be from induced background loss or low total gain. If the gain is too small no significant amount of signal is detected outside the cavity due to the low output coupling from the DFBs' high reflectivity.

5.2 Single Polarization Single Frequency (SPSF) Operation

The simulations results showed that the external cavity length L_{cavity}, the phase φ, and the wavelength detuning Δλ of the Bragg wavelengths are the main parameters affecting SPSF

operation. In doing so the realization of objective (2) was achieved. The phase relation between coupled cavities affects the laser output power. We observe a periodic behavior from the phase variation with localized maxima as we increased the pump power. This is, however, not purely periodic as the periodic behavior occurs in pair with the typical laser behavior of output power linearly proportional to the pump power. Quantum defect detunes both the cavity phase and its wavelength of operation from the external FBG (FPFBG). For small increments, Bragg wavelength detuning $\Delta\lambda$ acts as a phase shift on the cavity behavior. As the wavelength detuning increases due to heating in the phase-shifted (PS) DFB grating from the quantum defect, the lack of overlap between the Bragg wavelengths of the DFB and the external FBG gratings then becomes the main single polarization (SP) operation limitation factor – observed at Pp = 800 mW for the FBG tuning temperature of 36 °C. The quantum defect was partially mitigated by retuning the FPFBG temperature to the new PS DFB redshift operation wavelength. This enables SP operation at high pump powers – SP operation achieved at Pp = 800 mW and Pp = 900 mW for FPFBG temperatures of 41.3 °C and 43.2 °C respectively. This is possible only when the temperature of the FPFBG alone can be tuned, hence not in the desired short external cavity length. The heat induced by the quantum defect would require non-uniform cooling with maximum cooling located at the PS region to be fully mitigated. This could be done using smaller Peltier elements, but the non-uniform heat remains an inherent flaw of DFB fiber lasers not found in short-cavity fiber lasers.

While typical lasers operation enables a selection of output powers via pump powers, which increases their versatility, the external FBG design limits the Pp range of operation. The determined laser range for SP operation is $\Delta Pp \cong 300$ mW. This is one of the main limitations determined for the proposed design. However, constant pump power, or constant current are common regimes for the operations of lasers which suits our laser as it can operate with robust single polarization output. Moreover, high pump power operation is not recommended in DFB fiber lasers where undesired quantum defect effects previously mentioned are made more prevalent. The observed multimode operation at high pump power was investigated. The sidelobes present at 40 pm of the Bragg wavelength are due to the method used to write the FBG, but only become apparent at high pump powers. An increased apodization length of 30% was proposed and simulated as a solution to eliminate these unwanted modes. This in turn requires a higher RI modulation to maintain a fix grating strength.

Comparatively, X. Cen et al. 1.7 μm TDF short cavity laser was able to operate in SPSF with an output range of 1.5 mW to 12 mW with a respective range of 350 mW to 600 mW of absorbed pump power [74]. The SPSF output power range is much larger without the FPFBG. However, the phase-shifted DFB laser developed achieves 1.5 mW for a Pp = 460 mW, but only 250 mW of absorbed pump power – better laser efficiency at low pump power. This was determined by measuring the residual pump power at port 3 (P3) and subtracting it from the injected pump power in the fiber. We believe the output power can be further increased with the addition of a thermal compound with low viscosity such as glycerol. This is expected to have a similar effect from the laser cooling which demonstrated an increase in output power up to 77% for a constant pump power. This is due to increasing the heat dissipation and thus dampening the cavity chirp and phase shift. The quantum defect effect partial mitigation was confirmed by measuring a larger laser frequency shift at room temperature compared to the lower frequency shift when the laser is cooled.

The external cavity length impacts the spacing and thus number of transmission modes within the DFB stopband. We observed the resulting laser mode hopping experimentally and which was also seen in simulations. The FPFBG cavity length of 8.8 cm with a free spectral range = 1.17 GHz determined a length limit for mode-hop-free operation. The length challenge is a main flaw of short cavity lasers discussed throughout this work. The 1.7 um Tm doped fiber (TDF) laser based on a short-cavity design had its length limited to 1.8 cm for safe SPSF operation [74] compared to the proposed design limited to 8.8 cm in length. More importantly the length limitation in the proposed design is not from the gain cavity.

The cavity length used in this thesis, the most visible impact is on single frequency operation not single polarization operation, but L_{cavity} also increases the linear variation response of phase from temperature which compromises the stability of SP operation. Writing the phase shifted DFB and FPFBG separately and then performing a splice limits their minimal cavity length. The required high intensity splice arc can partially erase the refractive index modulation and thus the grating; a cavity length limitation encountered in this work. Splicing the non-PM fiber to the PM TDF before grating inscription would enable much lower cavity lengths controlled by the high precision FBG writing stage. This solution enables repeatability for the initial phase, quality control and ease of manufacturing while improving the robustness of the laser to temperature variations significantly.

The results indicate the important role of phase for SP operation, its control is a major challenge with a design based on coupled cavities and is related to equation **(2.13**) parameters. The coupled cavities phase ϕ can be expressed with two terms :

$$\phi = \phi_i + \Delta\phi \quad \textbf{(5.1)}$$

where ϕi is the initial phase, the phase induced by fixed parameters. These parameters are shown in the proposed design to be the external cavity length (O.P.), the temperature of operation and the Bragg wavelengths offset between both gratings. $\Delta\phi$ is a phase variation - for the PS DFB laser this is stress induced by strain and/or temperature variations for tuning and temperature stability purposes affecting the RI and cavity length L_{cavity}. Ideally, the response of the fiber to temperature and strain is uniform. This is normally limited by the strain and temperature setup used. In the proposed PS DFB laser, the selective polarization feedback relies on two fibers, hence most likely two different responses to the same applied stress. Results show that the thermal response of the materials differ and thus it requires considering the stress induced phase variation $\Delta\phi$ – the measured response was $\frac{\Delta\lambda}{\Delta T}$ = 16 pm/°C for TDF and $\frac{\Delta\lambda}{\Delta T}$ = 13 pm/°C for SMF-28 at 1742 nm. The PS DFB laser maintained SPSF operation for ΔT = 6.5 °C. This temperature variation was selected as it coincides with the TDF DBR laser [74] temperature variation and covers the temperature variation of ΔT = 4 °C for a shift of $\Delta\phi = \pi$ in TDF. If $\phi = \pi$ the losses of the selected polarization increase, and we observe SP operation for the slow axis. The reduced feedback then the phase relation is close to anti-phase values lead to dual polarization, the increase losses do not fully inhibit the selected polarization but still hinder it – disabling the SP operation regime. The induced phase variation $\Delta\phi$ from strain and temperature, in increments of $\pm$0.1°C, did not collapse SPSF operation. Their respective spectral response to temperature leads to thermo-optic coefficients $\frac{\partial n_g}{\partial T}$ = 9.2 μRI/°C for TDF and $\frac{\partial n_g}{\partial T}$ = 7.5 μRI/°C calculated with the Bragg wavelength response to temperature at 1742 nm.

Future investigation to understand the limitations of tuning include increasing the temperature tuning range, deepen the understanding of the temporal response from their respective thermo-optic coefficient, varying ϕ_i, the initial phase, and optimizing FPFBG reflectivity. For the temperature tuning range, we can expect SP operation to be halted before or at the wavelength difference

$\Delta\lambda$ =140 pm, the difference between FPFBG2 and the PS DFB grating. For both fibers to observe the same wavelength variation, it would require a temperature variation ΔT = 47 °C. With $\Delta\phi$ being constant, a variation of ϕ_i can be done with slight alterations of the O.P. by changing the external cavity length and then observing the resulting polarization regime of operation. Then, by repeated characterization of the frequency shift and observation of SPSF while temperature tuned one can determine initial phases to avoid collapse of SPSF operation. Finally, optimization for the FPFBG reflectivity is highly valuable to optimize the laser threshold and output power [65]. In its globality, this research project succeeded achieving its remaining objectives by developing a SPSF laser with robust operation with over 1 mW of output power and a FWHM and stability under 1 pm.

CHAPTER 6 CONCLUSION

The main objective of this work was to development of a single frequency linearly polarized laser in Tm polarization maintaining fiber near a wavelength of 1.7 μm using a phase-shifted (PS) distributed-feedback (DFB) structure for the generation of optical lattice for optical clocks applications. In Chapter 2 theorical background on PS DFB, thulium doped fiber and a state-of-the-art for SPSF operation in fibered lasers was presented. The single polarization single frequency (SPSF) laser methods were presented with their respective limitations and benefits. Chapter 3 presented the work performed during the research project for the development and characterization of the proposed design. Chapter 4 presented the characterization results and investigations performed. The initial focus was placed on fabricating the PS DFB laser, followed by the SPSF operation characterization of the laser. In between the fabrication and SPSF characterization, simulations were performed to understand the laser behavior. Chapter 5 further discussed the results while incorporating state-of-art elements, the challenges encountered were discussed with their respective solutions and future investigations.

The main objective was successfully achieved: develop a novel SPSF design for fiber lasers. The objectives also achieved the required specifications of minimum output power for the master oscillator power amplifier seeding of 1 mW, and a laser with a FWHM and stability under 1 pm. Comparison with short-cavity Tm doped fiber (TDF) based lasers at the same wavelength further exposed its benefits. (1) The fabrication of the laser does not require expensive splicer. (2) The laser gain media length is not limited for SPSF operation. (3) The laser enables the usage of smaller L-band wavelengths pump sources much more accessible and at lower cost. (4) The laser fabrication process for SPSF operation can be well controlled in a manufacturing environment and (5) it inherits the benefits from fiber optics. The main limitations of the laser are related to its coupled cavities behavior in terms of Bragg wavelength overlap, DFB lasers sensitivity, as well as mode field diameters mismatch and phase relation which is affected by the quantum defect and different thermo-optic coefficients inherent in the laser. Nonetheless, this is an additional tool in the state-of-the-art optical fiber laser designs for achieving SPSF operation. More investigations using the selected Tm doped fiber with the recommendations implemented, can lead to significantly better performance. Future work could then also include development of a 1.7 μm short cavity-based laser and a DFB cavity inscription using linearly polarized light for comparisons between

design with the selected TDF. This could incorporate the usage of UV light or the usage of recently developed femtosecond writing techniques as well as the usage of longer L-band wavelength pump which will lead to an improvement in thulium doped fiber lasers efficiency. Lastly, this research contributes to the promising future applications of optical clocks which require compactness and robustness to be more accessible and used in new environments.

REFERENCES

[1] T. H. Maiman, "Stimulated Optical Radiation in Ruby," *Nature,* vol. 187, no. 4736, pp. 493-494, 1960/08/01 1960, doi: 10.1038/187493a0.

[2] C. J. Koester and E. Snitzer, "Amplification in a Fiber Laser," *Appl. Opt.,* vol. 3, no. 10, pp. 1182-1186, 1964/10/01 1964, doi: 10.1364/AO.3.001182.

[3] S. Fu *et al.*, "Review of recent progress on single-frequency fiber lasers [Invited]," *J. Opt. Soc. Am. B,* vol. 34, no. 3, pp. A49-A62, 2017/03/01 2017, doi: 10.1364/JOSAB.34.000A49.

[4] Z. Burkley, A. D. Brandt, C. Rasor, S. F. Cooper, and D. C. Yost, "Highly coherent, watt-level deep-UV radiation via a frequency-quadrupled Yb-fiber laser system," *Appl. Opt.,* vol. 58, no. 7, pp. 1657-1661, 2019/03/01 2019, doi: 10.1364/AO.58.001657.

[5] P. Zhou, X. Wang, Y. Ma, H. Lü, and Z. Liu, "Review on recent progress on mid-infrared fiber lasers," *Laser Physics,* vol. 22, no. 11, pp. 1744-1751, 2012/11/01 2012, doi: 10.1134/S1054660X12110199.

[6] M. Chen, Z. Meng, Y. Zhang, J. Wang, and W. Chen, "Ultranarrow-Linewidth Brillouin/Erbium Fiber Laser Based on 45-cm Erbium-Doped Fiber," *IEEE Photonics Journal,* vol. 7, no. 1, pp. 1-6, 2015, doi: 10.1109/JPHOT.2015.2399354.

[7] W. Shi, Q. Fang, X. Zhu, R. A. Norwood, and N. Peyghambarian, "Fiber lasers and their applications [Invited]," *Appl. Opt.,* vol. 53, no. 28, pp. 6554-6568, 2014/10/01 2014, doi: 10.1364/AO.53.006554.

[8] K. Bongs *et al.*, "Development of a strontium optical lattice clock for the SOC mission on the ISS," *Comptes Rendus Physique,* vol. 16, no. 5, pp. 553-564, 2015/06/01/ 2015, doi: https://doi.org/10.1016/j.crhy.2015.03.009.

[9] H. Katori, "Optical lattice clocks and quantum metrology," *Nature Photonics,* vol. 5, no. 4, pp. 203-210, 2011/04/01 2011, doi: 10.1038/nphoton.2011.45.

[10] A. D. Ludlow, M. M. Boyd, J. Ye, E. Peik, and P. O. Schmidt, "Optical atomic clocks," *REVIEWS OF MODERN PHYSICS,* vol. 87, no. 2, 2015, doi: https://doi.org/10.1103/RevModPhys.87.637.

[11] M. M. Boyd, "High Precision Spectroscopy of Strontium in an Optical Lattice: Towards a New Standard for Frequency and Time," Doctor of Philosophy, Department of Physics, University of Colorado, Boulder, 2007. [Online]. Available: https://jila.colorado.edu/sites/default/files/2019-05/boyd_thesis.pdf

[12] *The International System of Units (SI) - 9th edition*. (2019). https://www.bipm.org/documents/20126/41483022/SI-Brochure-9-EN.pdf. Sèvres, France.

[13] S. Vladimir, R. W. Jason, and Y. Nan, "Direct semiconductor diode laser system for an optical lattice clock based on neutral strontium for future tests of fundamental physics in space," in *Proc.SPIE*, 2020, vol. 11296, p. 112962H, doi: 10.1117/12.2549377. [Online]. Available: https://doi.org/10.1117/12.2549377

[14] T. E. Mehlstäubler, G. Grosche, C. Lisdat, P. O. Schmidt, and H. Denker, "Atomic clocks for geodesy," *Reports on Progress in Physics,* vol. 81, no. 6, p. 064401, 2018/04/18 2018, doi: 10.1088/1361-6633/aab409.

[15] S. Bilicki, "Strontium optical lattice clocks: clock comparisons for timescales and fundamental physics applications

Horloges à réseau optique au strontium : comparaisons d'horloges pour des applications en physique fondamentale et échelles de temps," Observatoire de Paris - SYRTE, 2017. [Online]. Available: https://tel.archives-ouvertes.fr/tel-01711318

[16] M. Takamoto, F.-L. Hong, R. Higashi, and H. Katori, "An optical lattice clock," *Nature Letters,* vol. 435, 2005, doi: https://doi.org/10.1038/nature03541.

[17] Y. Wang, X. Lu, B. Lu, D. Kong, and H. Chang, "Recent Advances Concerning the 87Sr Optical Lattice Clock at the National Time Service Center," *Applied Sciences*, vol. 8, no. 11*,* doi: 10.3390/app8112194.

[18] T. Ido and H. Katori, "Recoil-Free Spectroscopy of Neutral Sr Atoms in the Lamb-Dicke Regime," *Physical Review Letters,* vol. 91, no. 5, p. 053001, 07/29/ 2003, doi: 10.1103/PhysRevLett.91.053001.

[19] S. Jackson and A. C. Vutha, "Magic polarization for cancellation of light shifts in two-photon optical clocks," *Physical Review A,* vol. 99, no. 6, p. 063422, 06/21/ 2019, doi: 10.1103/PhysRevA.99.063422.

[20] R. Hui and M. O'Sullivan, "Chapter 2 - Basic Instrumentation for Optical Measurement," in *Fiber Optic Measurement Techniques*, R. Hui and M. O'Sullivan Eds. Boston: Academic Press, 2009, pp. 129-258.

[21] B. E. A. Saleh and M. C. Teich, *Fundamentals of photonics / Bahaa E.A. Saleh, Malvin Carl Teich*, 2nd ed. (Wiley series in pure and applied optics). New York: Wiley, 2007.

[22] W. J. Eckner, A. W. Young, N. Schine, and A. M. Kaufman, "High-power, fiber–laser-based source for magic-wavelength trapping in neutral-atom optical clocks," *Review of Scientific Instruments,* vol. 92, no. 9, 2021, doi: https://doi.org/10.1063/5.0057619.

[23] K. O. Hill and G. Meltz, "Fiber Bragg grating technology fundamentals and overview," *Journal of Lightwave Technology,* vol. 15, no. 8, pp. 1263-1276, 1997, doi: 10.1109/50.618320.

[24] R. Kashyap, *Fiber Bragg Gratings*, 2nd ed. Academic Press, 2010.

[25] T. Erdogan, "Fiber grating spectra," *Journal of Lightwave Technology,* vol. 15, no. 8, pp. 1277-1294, 1997, doi: 10.1109/50.618322.

[26] A. Othonos, "Fiber Bragg gratings," *Review of Scientific Instruments,* vol. 68, no. 12, pp. 4309-4341, 1997/12/01 1997, doi: 10.1063/1.1148392.

[27] S. Loranger, "Discovery and Correction of Spatial Non-Uniformity in Optical Fibers: Towards the Fabrication of Perfect Ultra-Long Fiber Bragg Gratings for Applications in Non-Linear Optics," PhD thesis, Département de génie physique, École Polytechnique de Montréal, 2018. [Online]. Available: https://publications.polymtl.ca/2997/

[28] A. Roberge, "Fabrication of Fiber Bragg Gratings Using Femtosecond Laser Direct-Writing Techniques," Master's of Science Applied, Engineering Physics, Polytechnique Montreal, 2022.

[29] M. Gagné, "FABRICATION ET APPLICATIONS DES RÉSEAUX DE BRAGG ULTRA-LONGS," Doctor of Philosophy, Engineering Physics, Polytechnique Montréal, 2015. [Online]. Available: https://publications.polymtl.ca/1876/

[30] E. Chehura, S. W. James, and R. P. Tatam, "A simple and wavelength-flexible procedure for fabricating phase-shifted fibre Bragg gratings," *Measurement Science and Technology,* vol. 21, no. 9, p. 094001, 2010/07/28 2010, doi: 10.1088/0957-0233/21/9/094001.

[31] M. Gagné, S. Loranger, J. Lapointe, and R. Kashyap, "Fabrication of high quality, ultra-long fiber Bragg gratings: up to 2 million periods in phase," *Opt. Express,* vol. 22, no. 1, pp. 387-398, 2014/01/13 2014, doi: 10.1364/OE.22.000387.

[32] S. Loranger, V. Lambin-Iezzi, and R. Kashyap, "Reproducible ultra-long FBGs in phase corrected non-uniform fibers," *Optica,* vol. 4, no. 9, pp. 1143-1146, 2017/09/20 2017, doi: 10.1364/OPTICA.4.001143.

[33] A. Roberge, S. Loranger, J.-S. Boisvert, F. Monet, and R. Kashyap, "Femtosecond laser direct-writing of high quality first-order Bragg gratings with arbitrary complex apodization by phase modulation," *Opt. Express,* vol. 30, no. 17, pp. 30405-30419, 2022/08/15 2022, doi: 10.1364/OE.465331.

[34] Rumadi, A. Syahriar, D. Astharini, and A. H. Lubis, "The effects of apodization profile on uniform fiber Bragg gratings," in *2015 9th International Conference on Telecommunication Systems Services and Applications (TSSA)*, 25-26 Nov. 2015 2015, pp. 1-6, doi: 10.1109/TSSA.2015.7440430.

[35] S. D. Agger, "Thulium distributed-feedback fiber lasers," Doctor of Philosophy, Technical University of Denmark, Kgs. Lyngby, 2006. [Online]. Available: https://orbit.dtu.dk/en/publications/thulium-distributed-feedback-fiber-lasers

[36] S. Karsten, L. Samir, K. Philipp, and F. Peter, "2 µm Laser Sources and Their Possible Applications," in *Frontiers in Guided Wave Optics and Optoelectronics*, P. Bishnu Ed. Rijeka: IntechOpen, 2010, p. Ch. 21.

[37] K. Bremer *et al.*, "Sensitive detection of CO2 implementing tunable thulium-doped all-fiber laser," *Appl. Opt.,* vol. 52, no. 17, pp. 3957-3963, 2013/06/10 2013, doi: 10.1364/AO.52.003957.

[38] S. Agger, J. H. Povlsen, and P. Varming, "Single-frequency thulium-doped distributed-feedback fiber laser," *Opt. Lett.,* vol. 29, no. 13, pp. 1503-1505, 2004/07/01 2004, doi: 10.1364/OL.29.001503.

[39] S. D. Agger and J. H. Povlsen, "Emission and absorption cross section of thulium doped silica fibers," *Opt. Express,* vol. 14, no. 1, pp. 50-57, 2006/01/09 2006, doi: 10.1364/OPEX.14.000050.

[40] J. Cajzl *et al.*, "Thulium-Doped Silica Fibers with Enhanced Fluorescence Lifetime and Their Application in Ultrafast Fiber Lasers," *Fibers*, vol. 6, no. 3, doi: 10.3390/fib6030066.

[41] W. Blanc *et al.*, "Thulium environment in a silica doped optical fibre," *Journal of Non-Crystalline Solids,* vol. 354, no. 2, pp. 435-439, 2008/01/15/ 2008, doi: https://doi.org/10.1016/j.jnoncrysol.2007.06.083.

[42] "Fusion Splicing of Specialty Fiber," in *Optical Fiber Fusion Splicing*, A. D. Yablon Ed. Berlin, Heidelberg: Springer Berlin Heidelberg, 2005, pp. 229-253.

[43] G. P. Agrawal and N. K. Dutta, *Semiconductor Lasers*, 2nd ed. NY: Springer New York, 1993.

[44] L. Shah *et al.*, "Integrated Tm:fiber MOPA with polarized output and narrow linewidth with 100 W average power," *Opt. Express,* vol. 20, no. 18, pp. 20558-20563, 2012/08/27 2012, doi: 10.1364/OE.20.020558.

[45] J. Liu, H. Shi, K. Liu, Y. Hou, and P. Wang, "210 W single-frequency, single-polarization, thulium-doped all-fiber MOPA," *Opt. Express,* vol. 22, no. 11, pp. 13572-13578, 2014/06/02 2014, doi: 10.1364/OE.22.013572.

[46] H. Baghdasaryan *et al.*, "Single-Mode Light Generation in DFB Fiber Laser: Wavelength-Scale Electromagnetic Modelling by the Method of Single Expression," in *2018 International Conference on Broadband Communications for Next Generation Networks and Multimedia Applications (CoBCom)*, 11-13 July 2018 2018, pp. 1-6, doi: 10.1109/COBCOM.2018.8443979.

[47] V. E. Perlin and H. G. Winful, "Distributed feedback fiber Raman laser," *IEEE Journal of Quantum Electronics,* vol. 37, no. 1, pp. 38-47, 2001, doi: 10.1109/3.892722.

[48] S. Loranger, V. Karpov, G. W. Schinn, and R. Kashyap, "Single-frequency low-threshold linearly polarized DFB Raman fiber lasers," *Opt. Lett.,* vol. 42, no. 19, pp. 3864-3867, 2017/10/01 2017, doi: 10.1364/OL.42.003864.

[49] I. A. Nechepurenko, A. V. Dorofeenko, and O. V. Butov, "Optimal defect position in a DFB fiber laser," *Opt. Express,* vol. 29, no. 9, pp. 13657-13668, 2021/04/26 2021, doi: 10.1364/OE.418262.

[50] N. Hodgson and H. Weber, *Laser Resonators and Beam Propagation*, 2nd ed. (Springer Series in Optical Sciences). Heidelberg: Springer Berlin, 2005.

[51] G. P. Agrawal and S. Radic, "Phase-shifted fiber Bragg gratings and their application for wavelength demultiplexing," *IEEE Photonics Technology Letters,* vol. 6, no. 8, pp. 995-997, 1994, doi: 10.1109/68.313074.

[52] X. Sun, L. Zeng, Y. Hu, and J. a. Duan, "Fabrication and Sensing Application of Phase-shifted Bragg Grating Sensors," *Materials*, vol. 15, no. 10, doi: 10.3390/ma15103720.

[53] A. Asseh *et al.*, "10 cm Yb³⁺ DFB fibre laser with permanent phase-shifted grating," *Electronics Letters*, vol. 31, no. 12, pp. 969-970. [Online]. Available: https://digital-library.theiet.org/content/journals/10.1049/el_19950672

[54] R. Kashyap, P. F. Mckee, and D. Armes, "UV written reflection grating structures in photosensitive optical fibres using phase-shifted phase masks," *Electronics Letters*, vol. 30, no. 23, pp. 1977-1978. [Online]. Available: https://digital-library.theiet.org/content/journals/10.1049/el_19941357

[55] X. Chen, Y. Painchaud, K. Ogusu, and H. Li, "Phase Shifts Induced by the Piezoelectric Transducers Attached to a Linearly Chirped Fiber Bragg Grating," *Journal of Lightwave Technology,* vol. 28, no. 14, pp. 2017-2022, 2010, doi: 10.1109/JLT.2010.2051215.

[56] S. Loranger and R. Kashyap, "Efficiency increase of distributed feedback Raman fiber lasers by dynamic control of the phase shift," *Opt. Lett.,* vol. 43, no. 23, pp. 5705-5708, 2018/12/01 2018, doi: 10.1364/OL.43.005705.

[57] Y. u. Liu, S. B. Lee, and S. S. Choi, "Phase-Shifted Fiber Bragg Grating Transmission Filters Based on the Fabry-Perot Effect," *J. Opt. Soc. Korea,* vol. 2, no. 1, pp. 30-33, 1998/03/30 1998. [Online]. Available: https://opg.optica.org/josk/abstract.cfm?URI=josk-2-1-30.

[58] J. Sun *et al.*, "Fabrication of π phase-shifted fiber Bragg grating and its application in narrow linewidth 1.5 μm Er-doped fiber lasers," *Optics Communications,* vol. 407, pp. 344-348, 2018/01/15/ 2018, doi: https://doi.org/10.1016/j.optcom.2017.09.064.

[59] S. Loranger, A. Tehranchi, H. Winful, and R. Kashyap, "Realization and optimization of phase-shifted distributed feedback fiber Bragg grating Raman lasers," *Optica,* vol. 5, no. 3, pp. 295-302, 2018/03/20 2018, doi: 10.1364/OPTICA.5.000295.

[60] J. Geng, Q. Wang, T. Luo, S. Jiang, and F. Amzajerdian, "Single-frequency narrow-linewidth Tm-doped fiber laser using silicate glass fiber," *Opt. Lett.,* vol. 34, no. 22, pp. 3493-3495, 2009/11/15 2009, doi: 10.1364/OL.34.003493.

[61] W. Fan, B. Chen, X. Li, L. Chen, and Z. Lin, "Stress-induced single polarization DFB fiber lasers," *Optics Communications,* vol. 204, no. 1, pp. 157-161, 2002/04/01/ 2002, doi: https://doi.org/10.1016/S0030-4018(02)01242-7.

[62] C. Kin Seng, "Stress-induced birefringence fibers designed for single-polarization single-mode operation," *Journal of Lightwave Technology,* vol. 7, no. 2, pp. 436-441, 1989, doi: 10.1109/50.17791.

[63] S. A. Babin, D. V. Churkin, A. E. Ismagulov, S. I. Kablukov, and M. A. Nikulin, "Single frequency single polarization DFB fiber laser," *Laser Physics Letters,* vol. 4, no. 6, pp. 428-432, 2007/06/01 2007, doi: 10.1002/lapl.200610128.

[64] B. Yin, S. Feng, Z. Liu, Y. Bai, and S. Jian, "Single-Frequency and Single-Polarization DFB Fiber Laser Based on Tapered FBG and Self-Injection Locking," *IEEE Photonics Journal,* vol. 7, no. 3, pp. 1-9, 2015, doi: 10.1109/JPHOT.2015.2426871.

[65] J. L. Bueno Escobedo *et al.*, "Self-injection locking of the DFB laser through an external ring fiber cavity: Application for phase sensitive OTDR acoustic sensor," *Results in Physics,* vol. 7, pp. 641-643, 2017/01/01/ 2017, doi: https://doi.org/10.1016/j.rinp.2017.01.013.

[66] J. L. Philipsen *et al.*, "Polarisation control of DFB fibre laser using UV-induced birefringent phase-shift," *Electronics Letters*, vol. 34, no. 7, pp. 678-679. [Online]. Available: https://digital-library.theiet.org/content/journals/10.1049/el_19980492

[67] E. Wikszak *et al.*, "Linearly polarized ytterbium fiber laser based on intracore femtosecond-written fiber Bragg gratings," *Opt. Lett.,* vol. 32, no. 18, pp. 2756-2758, 2007/09/15 2007, doi: 10.1364/OL.32.002756.

[68] Y. Lai, A. Martinez, I. Khrushchev, and I. Bennion, "Distributed Bragg reflector fiber laser fabricated by femtosecond laser inscription," *Opt. Lett.,* vol. 31, no. 11, pp. 1672-1674, 2006/06/01 2006, doi: 10.1364/OL.31.001672.

[69] A. Siekiera, R. Engelbrecht, R. Neumann, and B. Schmauss, "Fiber Bragg gratings in polarization maintaining specialty fiber for Raman fiber lasers," *Physics Procedia,* vol. 5, pp. 671-677, 2010/01/01/ 2010, doi: https://doi.org/10.1016/j.phpro.2010.08.098.

[70] Z. Zhang, A. J. Boyland, J. K. Sahu, W. A. Clarkson, and M. Ibsen, "High-Power Single-Frequency Thulium-Doped Fiber DBR Laser at 1943 nm," *IEEE Photonics Technology Letters,* vol. 23, no. 7, pp. 417-419, 2011, doi: 10.1109/LPT.2011.2106491.

[71] Q. Yang *et al.*, "A Single-Frequency Linearly Polarized Fiber Laser Using a Newly Developed Heavily Tm3+-Doped Germanate Glass Fiber at 1.95 μm*," *Chinese Physics Letters,* vol. 32, no. 9, p. 094206, 2015/09/01 2015, doi: 10.1088/0256-307X/32/9/094206.

[72] X. Guan *et al.*, "High-efficiency sub-watt in-band-pumped single-frequency DBR Tm3+-doped germanate fiber laser at 1950 nm," *Opt. Express,* vol. 26, no. 6, pp. 6817-6825, 2018/03/19 2018, doi: 10.1364/OE.26.006817.

[73] J. Zhang *et al.*, "Single-frequency 1.7-μm Tm-doped fiber laser with optical bistability of both power and longitudinal mode behavior," *Opt. Express,* vol. 29, no. 14, pp. 21409-21417, 2021/07/05 2021, doi: 10.1364/OE.424336.

[74] X. Cen *et al.*, "Short-Wavelength, in-Band-Pumped Single- Frequency DBR Tm3+-Doped Germanate Fiber Laser at 1.7 μm," *IEEE Photonics Technology Letters,* vol. 33, no. 7, pp. 350-353, 2021, doi: 10.1109/LPT.2021.3056047.

[75] E. Fujita, Y. Mashiko, S. Asaya, M. Musha, and M. Tokurakawa, "High power narrow-linewidth linearly-polarized 1610 nm Er:Yb all-fiber MOPA," *Opt. Express,* vol. 24, no. 23, pp. 26255-26260, 2016/11/14 2016, doi: 10.1364/OE.24.026255.

[76] S. V. Firstov *et al.*, "Laser-Active Fibers Doped With Bismuth for a Wavelength Region of 1.6–1.8 μm," *IEEE Journal of Selected Topics in Quantum Electronics,* vol. 24, no. 5, pp. 1-15, 2018, doi: 10.1109/JSTQE.2018.2801461.

[77] L. Hu and C. Yuan, "Analysis of Splice Loss of Single-Mode Optical Fiber in the High Altitude Environment," *Coatings*, vol. 11, no. 8, doi: 10.3390/coatings11080876.

[78] S. V. Chernikov, J. R. Taylor, and R. Kashyap, "Coupled-cavity erbium fiber lasers incorporating fiber grating reflectors," *Opt. Lett.,* vol. 18, no. 23, pp. 2023-2025, 1993/12/01 1993, doi: 10.1364/OL.18.002023.

[79] X. Luo *et al.*, "Single polarization, narrow linewidth hybrid laser based on selective polarization mode feedback," *Optics & Laser Technology,* vol. 154, p. 108340, 2022/10/01/ 2022, doi: https://doi.org/10.1016/j.optlastec.2022.108340.

[80] Y.-G. Lin *et al.*, "First Evaluation and Frequency Measurement of the Strontium Optical Lattice Clock at NIM," *Chinese Physics Letters,* vol. 32, no. 9, p. 090601, 2015/08/19 2015, doi: 10.1088/0256-307x/32/9/090601.

[81] S. Falke *et al.*, "The⁸⁷Sr optical frequency standard at PTB," *Metrologia,* vol. 48, no. 5, pp. 399-407, 2011/09/12 2011, doi: 10.1088/0026-1394/48/5/022.

[82] M. L. Dennis, J. W. Dixon, and I. Aggarwal, "High power upconversion lasing at 810 nm, in Tm:ZBLAN fibre," *Electronics Letters*, vol. 30, no. 2, pp. 136-137. [Online]. Available: https://digital-library.theiet.org/content/journals/10.1049/el_19940077

[83] E. Kajikawa, T. Ishii, K. Ogawa, and M. Musha, "High-power 813-nm Tm3+-doped ZBLAN fiber MOPA withsignal-light photodarkening suppression," *Appl. Opt.,* vol. 60, no. 23, pp. 6776-6780, 2021/08/10 2021, doi: 10.1364/AO.430892.

[84] P. R. Watekar, J. Seongmin, and H. Won-Taek, "800-nm upconversion emission in Yb-sensitized Tm-doped optical fiber," *IEEE Photonics Technology Letters,* vol. 18, no. 15, pp. 1609-1611, 2006, doi: 10.1109/LPT.2006.879584.

[85] P. Peterka, I. Kasik, A. Dhar, B. Dussardier, and W. Blanc, "Theoretical modeling of fiber laser at 810 nm based on thulium-doped silica fibers with enhanced 3H4 level lifetime," *Opt. Express,* vol. 19, no. 3, pp. 2773-2781, 2011/01/31 2011, doi: 10.1364/OE.19.002773.

[86] A. D. Yablon, *Optical Fiber Fusion Splicing*, 1st ed. (Optical Sciences). Heidelberg: Springer Berlin, 2005.

[87] D. Marcuse, "Loss analysis of single-mode fiber splices," *The Bell System Technical Journal,* vol. 56, no. 5, pp. 703-718, 1977, doi: 10.1002/j.1538-7305.1977.tb00534.x.

[88] E. Ronnekleiv, M. N. Zervas, and J. T. Kringlebotn, "Modeling of polarization-mode competition in fiber DFB lasers," *IEEE Journal of Quantum Electronics,* vol. 34, no. 9, pp. 1559-1569, 1998, doi: 10.1109/3.709571.

[89] S. W. Lovseth and D. Y. Stepanov, "Dynamic analysis of multiple wavelength DFB fiber lasers," *IEEE Journal of Quantum Electronics,* vol. 37, no. 10, pp. 1237-1245, 2001, doi: 10.1109/3.952534.

[90] H. Rongqing and O. S. Maurice, *Fiber Optic Measurement Techniques*, 1st ed. Academic Press, 2009.

[91] M. Barbier, I. Zaquine, and P. Delaye, "Spontaneous four-wave mixing in liquid-core fibers: towards fibered Raman-free correlated photon sources," *New Journal of Physics,* vol. 17, no. 5, p. 053031, 2015/05/20 2015, doi: 10.1088/1367-2630/17/5/053031.

[92] M. Ohtsu, Y. Teramachi, Y. Otsuka, and A. Osaki, "Analyses of mode-hopping phenomena in an AlGaAs laser," *IEEE Journal of Quantum Electronics,* vol. 22, no. 4, pp. 535-543, 1986, doi: 10.1109/JQE.1986.1072987.